IMAGING ULTRAFAST DYNAMICS IN NANOMATERIALS USING SPATIALLY-SEPARATED PUMP-PROBE MICROSCOPY

Michelle M. Gabriel

A dissertation submitted to the faculty of the University of North Carolina at Chapel Hill in partial fulfillment of the requirements for the degree of Doctor of Philosophy in the Department of Chemistry.

Chapel Hill
2015

Approved by:

John M. Papanikolas

R. Mark Wightman

J. Michael Ramsey

James F. Cahoon

Joanna M. Atkin

ABSTRACT

Michelle M. Gabriel: Imaging Ultrafast Dynamics in Nanomaterials Using
Spatially-Separated Pump-Probe Microscopy
(Under the direction of John M. Papanikolas)

Understanding the fundamental physics of nanomaterials is critical for the advancement and rational design of new nanotechnologies. On the nanoscale, differences between individual structures, and even variations between different spatial locations within the same structure, can have a significant impact on the functional properties of nanomaterials and the electronic performance of nanodevices; yet much of our knowledge of nanostructure function is inferred from measurements that average over entire structures or integrate over long times. The existence of multiple conformations or structures within an ensemble, which often exhibit different dynamical behaviors, shroud the underlying dynamics, making it difficult to reach meaningful and quantitative conclusions.

These limitations are overcome with the development and implementation of an ultrafast pump-probe microscopy technique. With combined spatial and temporal resolution, the microscope is capable of collecting data from individual nanostructures at various spatially distinct locations with a high throughput. Additionally, the microscope's ability to excite an object in one location and probe it in another, allows the direct visualization of charge carrier motion and acoustic lattice motion on the nanoscale without the need for physical contact or active electrical connection.

In this work, the microscope has been used to image electron diffusion in intrinsically doped silicon nanowires as well as image a combination of electron diffusion and drift in silicon nanowire devices with built-in electric fields. Additionally, to demonstrate the versatility of the microscope, it has been employed to study the insulator-to-metal transition and coherent acoustic phonon mode propagation in vanadium (IV) oxide (VO_2) nanowires in a contactless imaging mode.

for my mother…

AKNOWLEDGEMENTS

First of all, I would like to express my deepest gratitude to my research advisor, Dr. John Papanikolas. Joining his lab was easily one of the best decisions I’ve ever made and I will always be grateful for his guidance, patience, and wacky sense of humor (and mostly for putting up with mine). I would also like to thank Dr. Ralph House and Dr. Brian Mehl and Dr. Justin Kirschbrown for their initial development of the microscope, and for their help when I first joined the Papanikolas group. Extra thanks goes to Justin for his collaboration and support on my initial projects and surprisingly, for actually keeping me sane. I’d also like to thank all of the members of the Papanikolas group, especially Emma Cating and Dr. Erik Grumstrup for their help and advice with the spatially-separated microscopy projects. Additional recognition is required for Dr. James Cahoon for his guidance and the rest of his group for providing silicon nanowire samples and helping with COMSOL, lithography, and various other projects.

I’d also like to express my gratitude to my entire committee, especially Dr. Mark Wightman for my first summer in Chapel Hill and first impression of research at UNC and for his continued support over the years.

Infinite thanks to my parents and my sisters, Andi and Bianca, for their unconditional love and support throughout my life, and to all of my friends in Chapel Hill who’ve become family: my sisters Sandi and Vivien, and my big brother Dave, as well as the entire extended family on Rosemary and Henderson. BIG thanks to Bub O’Malley’s and Chapel Hill Underground for parking, use of cable and internet, pretending like they actually *want* to hear all about my research and presentations, and for giving me a life outside of lab.

TABLE OF CONTENTS

LIST OF TABLES

LIST OF FIGURES

LIST OF ABBREVIATIONS

AFM	atomic force microscopy
AOM	acousto-optic modulator
BBO	beta barium borate
CVD	chemical vapor deposition
CW	continuous wave
EHP	electron-hole plasma
FET	field effect transistor
FT	Fourier transform
FWHM	full-width-at-half-maximum
IMT	insulator-to-metal transition
LBO	lithium triborate
MNW	micro/nanowire
NA	numerical aperture
NW	nanowire
PMT	photomultiplier tube
PSD	phase sensitive detection
RF	radio frequency
SEM	scanning electron microscopy
SHG	second harmonic generation
SOPP	spatially-overlapped pump-probe
SSPP	spatially-separated pump-probe
TA	transient absorption

TCSPC	time-correlated single photon counting
TR-PES	time-resolved photo-electron spectroscopy
VLS	vapor-liquid-solid

LIST OF SYMBOLS

a	radius
A_{ref},	amplitude of the reference frequency for lock-in detection
A_{sig},	amplitude of the signal in lock-in detection
β	full-width at half-maximum of diffusion profiles
c_L	longitudinal speed of sound in a material
γ_{pu}	spatial full-width at half-maximums of the pump pulse
γ_{pr}	spatial full-width at half-maximums of the probe pulse
d	diameter
D	diffusion constant
Δ_{pp}	spatial separation of the pump and probe beams
Δt	pump-probe delay time
E	electric field
E	Young's modulus
I	intensity
J_o	Bessel function
L	length of nanowire
λ	wavelength
ν	Poisson's ratio
ξ_n	eigenvalue for the breathing mode
ρ	charge density (Chapter 5)
ρ_m	density of a solid-state material (Chapter 6)
S	surface recombination velocity

σ	error
τ	recombination lifetime
τ_{br}	period of breathing mode
w	weight for instrumental weighted linear fit
ϕ_{ref}	phase component of the lock-in reference frequency
ϕ_{sig}	phase component of the signal frequency in lock-in detection
ψ_{ref}	waveform for the reference frequency for a lock-in detector
ψ_{sig}	waveform of the chopped pump pulse train in lock-in detection
ω_{br}	angular frequency of breathing mode
ω_{ext}	angular frequency of an extensional mode
ω_{ref}	angular frequency of the lock-in reference frequency
ω_{sig}	angular frequency of the signal waveform in lock-in detection

CHAPTER 1: INTRODUCTION

1.1 Motivation

Recent advances in technology and the associated demand for smaller and more efficient electronic, and optoelectronic devices have driven considerable research efforts focused on the optical properties of nanomaterials. As the size scale of materials becomes smaller and smaller, their properties begin to differ from those of the bulk offering a platform for the development of novel nanoscale devices. Understanding the fundamental physics of nanoscale materials is central to the developmental progress of emerging technologies.

The functional properties of nanomaterials are strongly influenced by their structural features, making them ideal for incorporation in innovative device applications. Time-resolved spectroscopic techniques have proven to be quite powerful for probing electron dynamics in semiconductor nanomaterials on ultrafast (sub-picosecond) timescales; however, these methods typically average over ensembles or entire structures that often vary in size, shape, composition, and physical conformation.[1-5] While electron diffusion characteristics have been studied in individual nanowires using functional imaging techniques, these experiments typically require complicated and time-consuming processing steps to attach metallic contacts to each nanowire to measure the electrical current flowing through the device.[6-10] Additionally, these methods lack dynamical time resolution and still average over the entire wire. The limited spatial information hinders the ability to correlate device performance with specific structural features that may vary along the length of the wire such as lattice defects or impurities. Disentangling signals from inhomogeneous samples presents a barrier for the rational design of new nanoscale devices. The ability to correlate function with underlying structure requires research methodologies with combined temporal and spatial resolution. The following section provides a brief overview of the evolution of spatiotemporal imaging.

1.2 Overcoming Heterogeneity

1.2.1 Time-Resolved Spectroscopy

When the focus of spectroscopic research shifted from isolated molecules in the gas phase to solvated reactions, the introduction of environmental heterogeneity within samples became a major obstacle for the reliable quantitative analysis these more complex systems. Frequency domain spectroscopy, the primary experimental technique for isolated molecules, was of limited use for the study of solvated systems. To overcome this issue, the development of new experimental techniques became vital. The ultrafast spectroscopies that emerged to meet this need enabled the observation of both solute and solvent processes on timescales as small as tens of femtoseconds. The ability to directly follow chemical dynamics in time dramatically improved the understanding of a variety of condensed phase phenomena, including energy and electron transfer processes, excited state relaxation, and solvation dynamics.

With improved spectroscopic techniques, research efforts progressed towards larger and more complicated systems such as biological materials, macromolecular systems, and nanomaterials. However, since typical spectroscopic analyses were performed over large ensembles, the effects of heterogeneity continued to pose distinct and even more arduous challenges. The existence of multiple conformations or structures within an ensemble, which often exhibit different dynamical behaviors, obscured the underlying chemical dynamics, making it difficult to reach meaningful and quantitative conclusions. While the multidimensional coherent spectroscopies that were originally developed to address this issue enabled the assignment of spectroscopic and dynamical contributions from different sub-ensembles, these techniques are still incapable of directly correlating specific dynamical phenomena with structural or conformational variations across the ensemble without additional experimental studies or complicated theoretical calculations.

1.2.2 Microscopy Methods

With increased spatial resolution, microscopy methods bypass the heterogeneous aspects of ensemble averaging by probing materials on a structure-to-structure basis, and enabling the direct observation of the physical properties of individual particles. Over the past several decades a variety of microscopy approaches (e.g. electron, scanning probe, optical) have been implemented to reveal broad distributions in the optical, electrical, and mechanical properties in an assortment of complex systems.

Far-field optical methods are perhaps the most widely used as they often offer less complicated experimental design while still providing intuitive access to conventional absorption and emission spectroscopies. Though their spatial resolution is limited to the order of the wavelength of light (i.e. diffraction-limited), far field techniques can still be used to study single particles in sufficiently dilute samples. This configuration has been applied to the investigation of a range of phenomena. In biological studies, fluorescence techniques have allowed the direct observation of the inter-conversion between conformations of biomolecules[11,12] and molecular motor functions.[13,14] Studies of single particles have advanced the understanding of the photophysics of individual nanostructures[15] and demonstrated significant enhancements in fluorescence, Raman, and other nonlinear processes by plasmonic nanoantennas.[16-18] Single-molecule methods have also provided insight into the properties of the ensemble, uncovering phenomena such as “blinking” in molecules, proteins, and nanoparticles.[19-22] While early single molecule work has had an incredible impact on our knowledge of the dynamics of sub-ensembles within complex systems, the “time-averaged” nature of detection has limited these methods to the investigation of relatively slow or steady-state processes.

1.2.3 Combining Temporal and Spatial Resolution

Advances in experimental methods with combined spatial and temporal resolution have prompted a shift from the time-averaged properties to the direct observation of the unfolding of the dynamical phenomena from which macroscopic functionality emerges. Over the past decade, transient absorption pump-probe techniques have been used in combination with optical microscopy methods to study charge carrier (electron and hole) dynamics with diffraction-limited spatial resolution in individual nanostructures[4,23-39] and two-dimensional materials and structures,[40-46] as well as acoustic modes and plasmonic propagation in metal nanoparticles.[47-50] While access to the highest spatial resolution can be achieved through implementation of subdiffraction-limited methods based on the coupling of ultrafast laser sources with scanning probe microscopies[51-60] and electron microscopies[61-67], the focus of this work is on the development and application of a diffraction-limited pump-probe microscopy technique capable of measuring time-resolved dynamics including transport phenomena along individual locations within a single nanostructure. Therefore, the following chapters will be devoted to diffraction-limited pump-probe microscopy.

1.3 Chapter Overview

While this chapter (**Chapter 1**) provides the rationale behind this work and an introduction to time-resolved microscopy, the next chapters take a more in depth look at diffraction-limited pump-probe microscopy with specific emphasis on transient absorption microscopy.

Chapter 2 is devoted to the details of a new spatially-separated pump-probe microscopy technique and the microscope itself, since its development and application comprises a major component of this dissertation work.

Chapter 3 summarizes the groundwork resulting from initial efforts in the development and application of the pump-probe microscope to encompass the spatially-separated capabilities for the experiments described herein.

Chapter 4 details the initial results of the spatially-separated pump-probe microscopy technique and its application to the study of charge carrier diffusion in intrinsic silicon nanowires and doped silicon nanowires.

In **Chapter 5,** the microscope is used to study a more complex silicon nanowire sample fabricated with a *p*-type/intrinsic/*n*-type junction encoded along each individual nanowire. In these experiments, carrier diffusion and drift in the presence of the built-in electric field of the junction are investigated in a high carrier injection regime.

Chapter 6 demonstrates the versatility of the spatially-separated pump-probe microscope by detailing its application to the study of the insulator-to-metal transition and propagation of coherent acoustic phonon modes in vanadium dioxide nanowires.

The last portion of this dissertation, **Chapter 7**, includes a brief summary of this work followed by challenges, future directions and conclusions.

REFERENCES

1 Kar, A., Upadhya, P. C., Dayeh, S. A., Picraux, S. T., Taylor, A. J. & Prasankumar, R. P. Probing Ultrafast Carrier Dynamics in Silicon Nanowires. *Ieee Journal of Selected Topics in Quantum Electronics* **17**, 889-895, (2011).

2 Prasankumar, R. P., Upadhya, P. C. & Taylor, A. J. Ultrafast carrier dynamics in semiconductor nanowires. *physica status solidi (b)* **246**, 1973-1995, (2009).

3 Styers-Barnett, D. J., Ellison, S. P., Mehl, B. P., Westlake, B. C., House, R. L., Park, C., Wise, K. E. & Papanikolas, J. M. Exciton Dynamics and Biexciton Formation in Single-Walled Carbon Nanotubes Studied with Femtosecond Transient Absorption Spectroscopy. *The Journal of Physical Chemistry C* **112**, 4507-4516, (2008).

4 Song, J. K., Willer, U., Szarko, J. M., Leone, S. R., Li, S. & Zhao, Y. Ultrafast upconversion probing of lasing dynamics in single ZnO nanowire lasers. *Journal of Physical Chemistry C* **112**, 1679-1684, (2008).

5 Grumstrup, E. M., Cating, E. M., Gabriel, M. M., Pinion, C. W., Christesen, J. D., Kirschbrown, J. R., Vallorz, E. L., Cahoon, J. F. & Papanikolas, J. M. Ultrafast Carrier Dynamics of Silicon Nanowire Ensembles: The Impact of Geometrical Heterogeneity on Charge Carrier Lifetime. *The Journal of Physical Chemistry C* **118**, 8626-8633, (2014).

6 Ahn, Y., Dunning, J. & Park, J. Scanning Photocurrent Imaging and Electronic Band Studies in Silicon Nanowire Field Effect Transistors. *Nano Letters* **5**, 1367-1370, (2005).

7 Howell, S. L., Padalkar, S., Yoon, K., Li, Q., Koleske, D. D., Wierer, J. J., Wang, G. T. & Lauhon, L. J. Spatial Mapping of Efficiency of GaN/InGaN Nanowire Array Solar Cells Using Scanning Photocurrent Microscopy. *Nano Letters* **13**, 5123-5128, (2013).

8 Gu, Y., Romankiewicz, J. P., David, J. K., Lensch, J. L., Lauhon, L. J., Kwak, E. S. & Odom, T. W. Local Photocurrent Mapping as a Probe of Contact Effects and Charge Carrier Transport in Semiconductor Nanowire Devices. *Journal of Vacuum Science & Technology B: Microelectronics and Nanometer Structures* **24**, 2172, (2006).

9 Allen, J. E., Hemesath, E. R. & Lauhon, L. J. Scanning Photocurrent Microscopy Analysis of Si Nanowire Field-Effect Transistors Fabricated by Surface Etching of the Channel. *Nano Letters* **9**, 1903-1908, (2009).

10 Gutsche, C., Niepelt, R., Gnauck, M., Lysov, A., Prost, W., Ronning, C. & Tegude, F. J. Direct Determination of Minority Carrier Diffusion Lengths at Axial GaAs Nanowire p-n Junctions. *Nano Letters* **12**, 1453-1458, (2012).

11 Schuler, B., Lipman, E. A. & Eaton, W. A. Probing the free-energy surface for protein folding with single-molecule fluorescence spectroscopy. *Nature* **419**, 743-747, (2002).

12 Lu, H. P., Xun, L. & Xie, X. S. Single-Molecule Enzymatic Dynamics. *Science* **282**, 1877-1882, (1998).

13 Joo, C., Balci, H., Ishitsuka, Y., Buranachai, C. & Ha, T. Advances in single-molecule fluorescence methods for molecular biology. *Annual Review of Biochemistry* **77**, 51-76, (2008).

14 Peterman, E. J., Sosa, H. & Moerner, W. E. Single-molecule fluorescence spectroscopy and microscopy of biomolecular motors. *Annual Review of Physical Chemistry* **55**, 79-96, (2004).

15 Nirmal, M., Dabbousi, B. O., Bawendi, M. G., Macklin, J. J., Trautman, J. K., Harris, T. D. & Brus, L. E. Fluorescence intermittency in single caadmium selenide nanocrystal. *Nature* **383**, 802-804, (1996).

16 Le Ru, E. C. & Etchegoin, P. G. Single-molecule surface-enhanced Raman spectroscopy. *Annual Review of Physical Chemistry* **63**, 65-87, (2012).

17 Nie, S. & Emory, S. R. Probing Single Molecules and Single Nanoparticles by Surface-Enhanced Raman Scattering. *Science* **275**, 1102-1106, (1997).

18 Michaels, A. M., Jiang & Brus, L. Ag Nanocrystal Junctions as the Site for Surface-Enhanced Raman Scattering of Single Rhodamine 6G Molecules. *The Journal of Physical Chemistry B* **104**, 11965-11971, (2000).

19 Basché, T., Kummer, S. & Bräuchle, C. Direct spectroscopic observation of quantum jumps of a single molecule. *Nature* **373**, 132-134, (1995).

20 Dickson, R. M., Cubitt, A. B., Tsien, R. Y. & Moerner, W. E. On/off blinking and switching behaviour of single molecules of green fluorescent protein. *Nature* **388**, 355-358, (1997).

21 Neuhauser, R. G., Shimizu, K. T., Woo, W. K., Empedocles, S. A. & Bawendi, M. G. Correlation between Fluorescence Intermittency and Spectral Diffusion in Single Semiconductor Quantum Dots. *Physical Review Letters* **85**, 3301-3304, (2000).

22 Kuno, M., Fromm, D. P., Hamann, H. F., Gallagher, A. & Nesbitt, D. J. Nonexponential "blinking" kinetics of single CdSe quantum dots: A universal power law behavior. *The Journal of Chemical Physics* **112**, 3117, (2000).

23 Graham, M. W., Shi, S. F., Wang, Z. H., Ralph, D. C., Park, J. & McEuen, P. L. Transient Absorption and Photocurrent Microscopy Show That Hot Electron Supercollisions Describe the Rate-Limiting Relaxation Step in Graphene. *Nano Letters* **13**, 5497-5502, (2013).

24 Gabor, N. M., Zhong, Z., Bosnick, K. & McEuen, P. L. Ultrafast Photocurrent Measurement of the Escape Time of Electrons and Holes from Carbon Nanotube p-i-n Photodiodes. *Physical Review Letters* **108**, 087404, (2012).

25 Gabriel, M. M., Kirschbrown, J. R., Christesen, J. D., Pinion, C. W., Zigler, D. F., Grumstrup, E. M., Mehl, B. P., Cating, E. E. M., Cahoon, J. F. & Papanikolas, J. M. Direct Imaging of Free Carrier and Trap Carrier Motion in Silicon Nanowires by Spatially-Separated Femtosecond Pump-Probe Microscopy. *Nano Letters* **13**, 1336-1340, (2013).

26 Gao, B., Hartland, G. V. & Huang, L. B. Transient Absorption Spectroscopy of Excitons in an Individual Suspended Metallic Carbon Nanotube. *Journal of Physical Chemistry Letters* **4**, 3050-3055, (2013).

27 Grumstrup, E. M., Gabriel, M. M., Cating, E. M., Pinion, C. W., Christesen, J. D., Kirschbrown, J. R., Vallorz, E. L., Cahoon, J. F. & Papanikolas, J. M. Ultrafast Carrier Dynamics in Individual Silicon Nanowires: Characterization of Diameter-Dependent Carrier Lifetime and Surface Recombination with Pump-Probe Microscopy. *Journal of Physical Chemistry C* **118**, 8634-8640, (2014).

28 Mehl, B. P., Kirschbrown, J. R., Gabriel, M. M., House, R. L. & Papanikolas, J. M. Pump-Probe Microscopy: Spatially Resolved Carrier Dynamics in ZnO Rods and the Influence of Optical Cavity Resonator Modes. *Journal of Physical Chemistry B* **117**, 4390-4398, (2013).

29 Mehl, B. P., Kirschbrown, J. R., House, R. L. & Papanikolas, J. M. The End Is Different than The Middle: Spatially Dependent Dynamics in ZnO Rods Observed by Femtosecond Pump–Probe Microscopy. *The Journal of Physical Chemistry Letters* **2**, 1777-1781, (2011).

30 Schumacher, T., Giessen, H. & Lippitz, M. Ultrafast Spectroscopy of Quantum Confined States in a Single CdSe Nanowire. *Nano Letters* **13**, 1706-1710, (2013).

31 Seo, M. A., Dayeh, S. A., Upadhya, P. C., Martinez, J. A., Swartzentruber, B. S., Picraux, S. T., Taylor, A. J. & Prasankumar, R. P. Understanding ultrafast carrier dynamics in single quasi-one-dimensional Si nanowires. *Applied Physics Letters* **100**, 071104, (2012).

32 Seo, M. A., Yoo, J., Dayeh, S. A., Picraux, S. T., Taylor, A. J. & Prasankumar, R. P. Mapping carrier diffusion in single silicon core-shell nanowires with ultrafast optical microscopy. *Nano Letters* **12**, 6334-6338, (2012).

33 Szarko, J. M., Song, J. K., Blackledge, C. W., Swart, I., Leone, S. R., Li, S. & Zhao, Y. Optical injection probing of single ZnO tetrapod lasers. *Chemical Physics Letters* **404**, 171-176, (2005).

34 Gabriel, M. M., Grumstrup, E. M., Kirschbrown, J. R., Pinion, C. W., Christesen, J. D., Zigler, D. F., Cating, E. E., Cahoon, J. F. & Papanikolas, J. M. Imaging Charge Separation and Carrier Recombination in Nanowire p-i-n Junctions Using Ultrafast Microscopy. *Nano Letters* **14**, 3079-3087, (2014).

35 Grumstrup, E. M., Gabriel, M. M., Pinion, C. W., Parker, J. K., Cahoon, J. F. & Papanikolas, J. M. Reversible strain-induced electron-hole recombination in silicon nanowires observed with femtosecond pump-probe microscopy. *Nano Letters* **14**, 6287-6292, (2014).

36 Son, B. H., Park, J. K., Hong, J. T., Park, J. Y., Lee, S. & Ahn, Y. H. Imaging ultrafast carrier transport in nanoscale field-effect transistors. *ACS Nano* **8**, 11361-11368, (2014).

37 Blake, J. C., Eldridge, P. S. & Gundlach, L. Spatial variation in carrier dynamics along a single CdSSe nanowire. *Chemical Physics* **442**, 128-131, (2014).

38 Gundlach, L. & Piotrowiak, P. Ultrafast Spatially Resolved Carrier Dynamics in Single CdSSe Nanobelts. *Journal of Physical Chemistry C* **113**, 12162-12166, (2009).

39 Gundlach, L. & Piotrowiak, P. Femtosecond Kerr-gated wide-field fluorescence microscopy. *Optics Letters* **33**, 992-994, (2008).

40 Gao, B., Hartland, G., Fang, T., Kelly, M., Jena, D., Xing, H. L. & Huang, L. B. Studies of Intrinsic Hot Phonon Dynamics in Suspended Graphene by Transient Absorption Microscopy. *Nano Letters* **11**, 3184-3189, (2011).

41 Ruzicka, B. A., Wang, S., Liu, J., Loh, K.-P., Wu, J. Z. & Zhao, H. Spatially resolved pump-probe study of single-layer graphene produced by chemical vapor deposition [Invited]. *Optical Materials Express* **2**, 708-716, (2012).

42 Ruzicka, B. A., Wang, S., Werake, L. K., Weintrub, B., Loh, K. P. & Zhao, H. Hot carrier diffusion in graphene. *Physical Review B* **82**, 195414, (2010).

43 Shi, H., Yan, R., Bertolazzi, S., Brivio, J., Gao, B., Kis, A., Jena, D., Xing, H. G. & Huang, L. Exciton dynamics in suspended monolayer and few-layer MoS(2) 2D crystals. *ACS Nano* **7**, 1072-1080, (2013).

44 Wang, R., Ruzicka, B. A., Kumar, N., Bellus, M. Z., Chiu, H.-Y. & Zhao, H. Ultrafast and spatially resolved studies of charge carriers in atomically thin molybdenum disulfide. *Physical Review B* **86**, 045406, (2012).

45 Zhao, H., Mower, M. & Vignale, G. Ambipolar spin diffusion and D'yakonov-Perel' spin relaxation in GaAs quantum wells. *Physical Review B* **79**, 115321, (2009).

46 Yu, G., Liu, X., Xing, G., Chen, S., Ng, C. F., Wu, X., Yeow, E. K. L., Lew, W. S. & Sum, T. C. Spatially-Resolved Ultrafast Optical Spectroscopy of Polymer-Grafted Residues on CVD Graphene. *The Journal of Physical Chemistry C* **118**, 708-713, (2014).

47 Lo, S. S., Shi, H. Y., Huang, L. B. & Hartland, G. V. Imaging the extent of plasmon excitation in Au nanowires using pump-probe microscopy. *Optics Letters* **38**, 1265-1267, (2013).

48 Staleva, H. & Hartland, G. V. Transient absorption studies of single silver nanocubes. *Journal of Physical Chemistry C* **112**, 7535-7539, (2008).

49 Staleva, H. & Hartland, G. V. Vibrational Dynamics of Silver Nanocubes and Nanowires Studied by Single-Particle Transient Absorption Spectroscopy. *Advanced Functional Materials* **18**, 3809-3817, (2008).

50 Staleva, H., Skrabalak, S. E., Carey, C. R., Kosel, T., Xia, Y. N. & Hartland, G. V. Coupling to light, and transport and dissipation of energy in silver nanowires. *Physical Chemistry Chemical Physics* **11**, 5889-5896, (2009).

51 Terada, Y., Yoshida, S., Takeuchi, O. & Shigekawa, H. Real-space imaging of transient carrier dynamics by nanoscale pump-probe microscopy. *Nat Photon* **4**, 869-874, (2010).

52 Karki, K., Namboodiri, M., Zeb Khan, T. & Materny, A. Pump-probe scanning near field optical microscopy: Sub-wavelength resolution chemical imaging and ultrafast local dynamics. *Applied Physics Letters* **100**, 153103, (2012).

53 Berweger, S., Atkin, J. M., Xu, X. G., Olmon, R. L. & Raschke, M. B. Femtosecond Nanofocusing with Full Optical Waveform Control. *Nano Letters* **11**, 4309-4313, (2011).

54 Berweger, S., Atkin, J. M., Olmon, R. L. & Raschke, M. B. Light on the Tip of a Needle: Plasmonic Nanofocusing for Spectroscopy on the Nanoscale. *The Journal of Physical Chemistry Letters* **3**, 945-952, (2012).

55 Atkin, J. M. & Raschke, M. B. Techniques: Optical spectroscopy goes intramolecular. *Nature* **498**, 44-45, (2013).

56 Atkin, J. M., Berweger, S., Jones, A. C. & Raschke, M. B. Nano-optical imaging and spectroscopy of order, phases, and domains in complex solids. *Advances in Physics* **61**, 745-842, (2012).

57 Smith, S., Holme, N. C. R., Orr, B., Kopelman, R. & Norris, T. Ultrafast measurement in GaAs thin films using NSOM. *Ultramicroscopy* **71**, 213-223, (1998).

58 Nechay, B. A., Siegner, U., Achermann, M., Bielefeldt, H. & Keller, U. Femtosecond pump-probe near-field optical microscopy. *Review of Scientific Instruments* **70**, 2758-2764, (1999).

59 Nechay, B. A., Siegner, U., Morier-Genoud, F., Schertel, A. & Keller, U. Femtosecond near-field optical spectroscopy of implantation patterned semiconductors. *Applied Physics Letters* **74**, 61-63, (1999).

60 Shen, Y., Lin, T.-C., Dai, J., Markowicz, P. & Prasad, P. N. Near-Field Optical Imaging of Transient Absorption Dynamics in Organic Nanocrystals. *The Journal of Physical Chemistry B* **107**, 13551-13553, (2003).

61 Gong, Y., Joly, A. G., Hu, D., El-Khoury, P. Z. & Hess, W. P. Ultrafast Imaging of Surface Plasmons Propagating on a Gold Surface. *Nano Letters* **15**, 3472-3478, (2015).

62 Baum, P., Yang, D.-S. & Zewail, A. H. 4D Visualization of Transitional Structures in Phase Transformations by Electron Diffraction. *Science* **318**, 788-792, (2007).

63 Lobastov, V. A., Weissenrieder, J., Tang, J. & Zewail, A. H. Ultrafast Electron Microscopy (UEM): Four-Dimensional Imaging and Diffraction of Nanostructures during Phase Transitions. *Nano Letters* **7**, 2552-2558, (2007).

64 Fukumoto, K., Yamada, Y., Onda, K. & Koshihara, S.-y. Direct imaging of electron recombination and transport on a semiconductor surface by femtosecond time-resolved photoemission electron microscopy. *Applied Physics Letters* **104**, 053117, (2014).

65 Fukumoto, K., Onda, K., Yamada, Y., Matsuki, T., Mukuta, T., Tanaka, S.-i. & Koshihara, S.-y. Femtosecond time-resolved photoemission electron microscopy for spatiotemporal imaging of photogenerated carrier dynamics in semiconductors. *Review of Scientific Instruments* **85**, 083705, (2014).

66 Ortalan, V. & Zewail, A. H. 4D Scanning Transmission Ultrafast Electron Microscopy: Single-Particle Imaging and Spectroscopy. *Journal of the American Chemical Society* **133**, 10732-10735, (2011).

67 Mohammed, O. F., Yang, D.-S., Pal, S. K. & Zewail, A. H. 4D Scanning Ultrafast Electron Microscopy: Visualization of Materials Surface Dynamics. *Journal of the American Chemical Society* **133**, 7708-7711, (2011).

CHAPTER 2: INSTRUMENTATION

2.1 Microscope Description

A major emphasis of the work described in this dissertation is the development and implementation of a spatiotemporal instrument incorporating a scanning mechanism whereby the position of the probe can be independently positioned relative to the pump. The introduction of this spatially-separated configuration increases the versatility of the microscope in that it can be operated in a spatially-overlapped pump-probe (SOPP) mode and a spatially-separated pump-probe (SSPP) mode. In the new SSPP mode, samples can be excited in one location and probed in another, enabling the visualization of transport properties in nanomaterials.

Figure 2.1 shows a schematic of our instrument.[1-6] The primary source of radiation begins with a solid state diode-pumped continuous wave (CW) laser (Spectra Physics: Millennia Pro-15sJ). The Millennia uses the output from a diode laser to pump a neodymium yttrium vanadate crystalline matrix ($Nd:YVO_4$). The resulting near-infrared emission with a wavelength of $\lambda = 1064$ is frequency doubled by second-harmonic generation in a lithium triborate (LBO; LiB_3O_5) crystal, which can output up to 15 W of CW radiation at a wavelength of 532 nm.

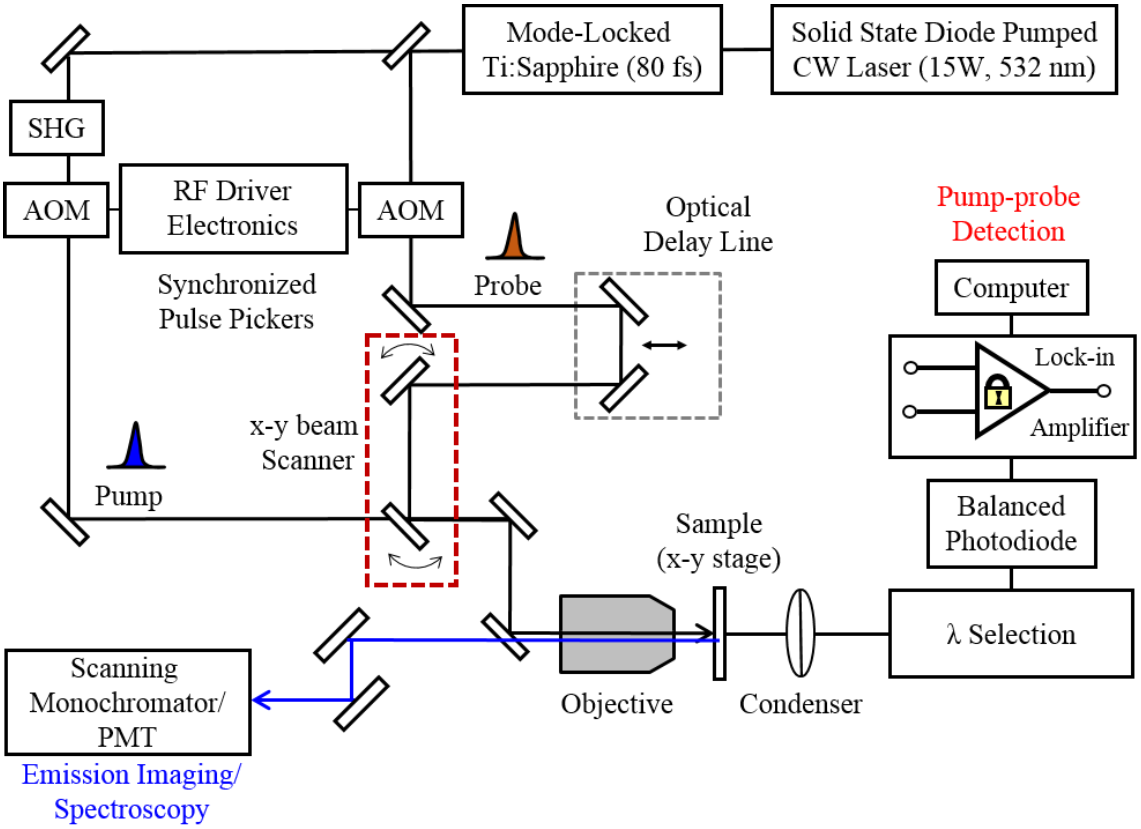

Figure 2.1: Schematic diagram of the pump−probe microscope. The pump and probe pulses are obtained from the output of a Ti:Sapphire laser operating at 80 MHz. The beam is split into the two pump and probe pulses. The pump portion is frequency doubled by SHG in a BBO crystal. Both beams are directed through synchronized AOMs to reduce the repetition rate of the pulses. The probe is sent through a mechanical delay stage (optical delay line) to vary its arrival time at the sample with respect to that of the pump. The probe beam is also directed passed a set of two scanning mirrors which vary the angle at which it enters the back aperture of the objective enabling its focal position to be adjusted laterally with respect to that of the pump. The pump and probe beams are recombined using a beam splitter and focused to diffraction-limited spots at the sample. Spatially-overlapped imaging is achieved by raster scanning the sample stage across the objective focal point while spatially-separated imaging is achieved by raster scanning the position of the probe with respect to the pump while holding the delay stage fixed. The change in transmitted probe signal is monitored with a balanced photodetector and lock-in amplifier.

The 532 nm CW output of the Millennia is used to pump a Ti:Sapphire laser (Spectra Physics: Tsunami). The gain medium of the laser is a sapphire crystalline matrix (Ti:Al_2O_3) where titanium ions (Ti^{3+}) are substituted for a small percentage of the Al^{3+} ions. Absorption in the gain medium occurs over a broad range of wavelengths from 400 – 600 nm. The resulting stimulated emission generates a laser output tunable over 700 – 1000 nm. The mode-locked pulses are <100 fs in with a repetition rate of 80 MHz.

For the majority of the experiments discussed in this work, the output of the Ti:Sapphire laser is tuned to 850 nm. A portion of the 850 nm beam is split off to serve as the probe and the remainder is frequency doubled using second harmonic generation (SHG) in a beta barium borate (BBO) crystal to produce the 425 nm pump beam. Both pump and probe beams are passed through two dedicated acousto-optic modulators (AOMs), one for each beam, to reduce the repetition rate of the laser to 1-4 MHz. This step ensures that the sample returns to its equilibrium state before the next pump-probe pulse pair arrives. The AOMs (Gooch & Housego: 17389.93-FOA), are controlled using two RF drivers (Gooch & Housego: 64381.9-SYN-9.5-1 for the probe AOM and Gooch & Housego: R31389.5-5AS for the pump AOM). The drivers are synchronized using the sync output of the electronics module from the Ti:Sapphire laser (Spectra-Physics: 3995) and a delay generator (SRS-645DG).

The probe is passed through a mechanical delay stage to vary its arrival time at the sample with respect to the pump. The sample is positioned using a moveable x-y stage (Queensgate Instruments: NPS-XY-100A). Computer controlled mirrors vary the angle of incidence of the probe beam as it enters the objective, allowing the probe beam to be focused to a point on the sample that is laterally offset relative to the pump. Before focusing, the pump and probe beams are recombined with a dichroic beam-splitter and directed onto the back aperture of a 100X microscope objective with a numerical aperture (NA) of 0.8. Focusing is achieved by adjusting the height of the objective using a nanopiezo-actuated stage, enabling remote controlled focusing of the two laser pulses to diffraction-limited spot sizes. In the case of a 425 nm pump pulse and an 850 nm probe pulse, additional steps are taken to ensure that both colors reach a focal point in the same plane. This is achieved by slightly decollimating the pump light before the objective.

After passing through the sample, light is collected using a condenser lens with a higher numerical aperture than the objective. Pump light is removed by spectral filters and the intensity of the probe beam (I) is measured using a balanced photodetector. Pump-induced changes in the probe beam (ΔI) are extracted through the use of a lock-in detector (SRS: SR830) where the pump AOM is inhibited at a 50% duty cycle to modulate the pump beam at 10-20 kHz. This frequency also serves as the reference for the lock-in detector which will be discussed in more detail below. This transient absorption microscopy technique is remarkably sensitive, capable of detecting $\Delta I/I \sim 5\text{x}10^{-5}$.

2.1.1 Performance Characteristics

The microscope is also capable of emission detection in a forward-scatter mode, where detection comes after the sample (not shown in Figure 2.1) or in a backward-scatter mode where fluorescence emanating from emissive samples is recollected by the microscope objective, focused on the slit of a monochromator, and detected by a photomultiplier tube (PMT). Emission detection is used to measure additional performance characteristics of the microscope such as temporal resolution and spatial resolution.

The time resolution (~500 fs) is estimated by taking a cross-correlation of the pump and probe beams (Figure 2.2A). This is achieved by focusing both beams onto a single point within a zinc oxide (ZnO) crystal. Sum frequency generation is an instantaneous nonlinear process that occurs only when the pump and probe beams are focused and overlapped spatially and temporally within a nonlinear crystal. The monochromator is set to only pass the sum frequency of the pump and probe pulses which is detected using the PMT while the delay stage is scanned. A Gaussian peak in signal is observed as the two pulses cross temporally. The time resolution is taken as full-width-at-half-maximum (FWHM) the Gaussian.

The diffraction-limited spatial resolution of the microscope is demonstrated using the two-photon fluorescence of a quantum dot (Figure 2.2B) which can be thought of as point source emitter. Emission from quantum dots is collected while the sample stage is raster scanned across the focal point. The emission profile of a single dot excited by 810 nm pulses is a 2D Gaussian with a FWHM of ~400 nm.

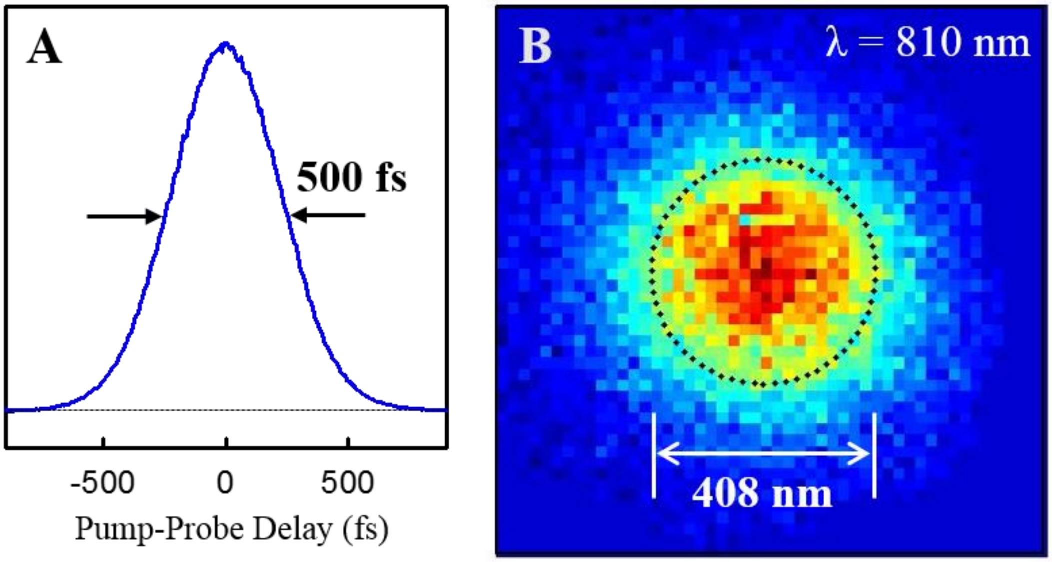

Figure 2.2: Microscope resolution. (A) Cross-correlation of the pump and probe pulses in the microscope obtained by monitoring the sum-frequency signal generated by a ZnO crystal. **(B)** Two-photon emission image of a 100 nm nanoparticle with 810 nm excitation. The size of the emission feature suggests that the lateral resolution is approximately 410 nm.

2.1.2 Transient Absorption

The basic operating principal of a pump-probe technique is illustrated in Figure 2.3. Though pump-probe techniques can be operated in transient reflectivity or transient absorption mode, the experiments presented in this work were all carried out in the transient absorption configuration illustrated in the figure. An initial pump pulse excites the sample, giving rise to a change in its absorption and/or reflectivity (and therefore, transmission) properties. The probe pules measures a dynamic response in a sample due to an excitation pump pulse. The dynamic response is measured over different pump-probe delays by scanning the mechanical delay stage. In Figure 2.3A, the probe pulse arrives before the pump, and therefore, no change in probe intensity is observed. A spike in signal appears just after (or quasi-simultaneously with) the pump pulse due to sample excitation. As pump-probe delay grows longer, the sample relaxes back to its equilibrium state. The changes are monitored by a decrease in probe intensity over time.

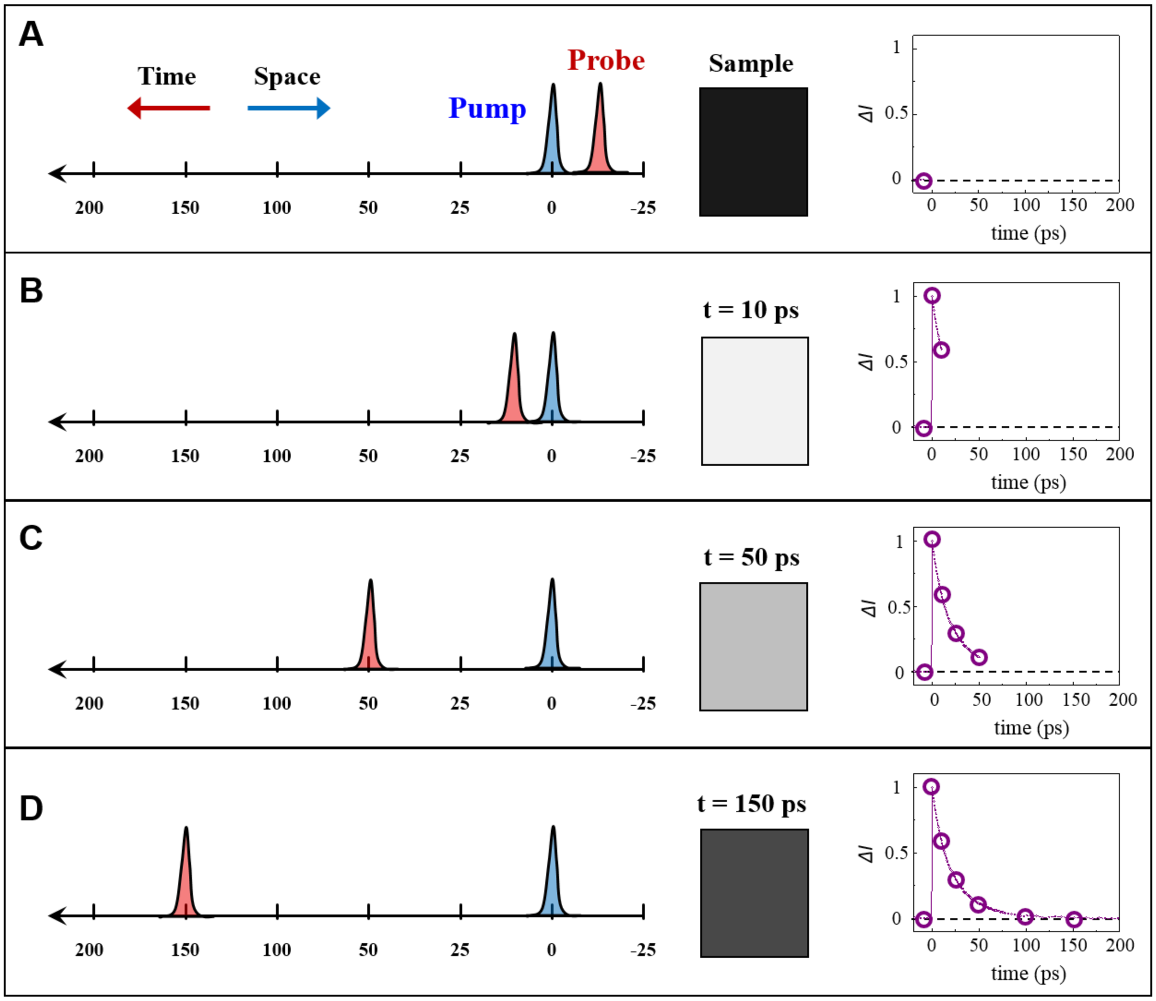

Figure 2.3: Diagram of transient absorption. (A) The transient absorption experiment in comprised of two pulses, a pump (blue) a probe (red) which is scanned in time relative to the pump pulse. In this diagram, time progresses to the left (red arrow) and the spatial coordinate is to the right (blue arrow) such that in the top configuration the probe pulse hits the sample before the pump pulse. In this configuration, the sample exhibits no pump-induced change in optical properties and the measured change in probe transmission is zero (plot on far right). **(B)** After the pump pulse excites the sample, a change in transmission properties of the probe occurs. In this case the sample transmits more probe light after excitation and a maximum in signal is seen just after the pump pulse arrives at the sample. **(C)** As the probe pulse is delayed further in time, the sample begins to relax back to it equilibrium position and a decrease in pump-induced transmission is observed. **(D)** After the sample has had sufficient time to completely relaxed, the observed signal response is back at baseline.

2.1.3 Lock-in Detection

Small pump-induced changes in probe transmission are monitored using lock-in detection. The lock-in amplifier is capable of extracting a small signal in an extremely noisy environment using a technique known as phase sensitive detection (PSD), which selects a single component of the signal at a specific reference frequency and phase and rejects noise signals at all other frequencies. In order to do this, the lock-in requires a reference signal, ψ_{ref}, which is generally a square wave output from a function generator that the lock-in converts to a sine wave with the waveform:

$$\psi_{ref} = A_{ref}\cos(\omega_{ref}t + \phi_{ref}) \qquad \text{Eq. 2.1}$$

where A_{ref}, ω_{ref}, and ϕ_{ref} are the amplitude, frequency and phase components of the reference signal. The pump pulse train is also chopped at the same frequency and phase as the lock-in reference using a delay generator with the waveform:

$$\psi_{sig} = A_{sig}\cos(\omega_{sig}t + \phi_{sig}) \qquad \text{Eq. 2.2}$$

where A_{sig}, ω_{sig}, and ϕ_{sig} are the amplitude, frequency and phase components signal. Since the lock-in amplifier multiplies the reference frequency by the signal, consider the multiplication of ψ_{ref} and ψ_{sig}, taking into account the product to sum identity:

$$\psi_{ref}\psi_{sig} = \frac{A_{ref}A_{sig}}{2}\cos\left[\left(\omega_{ref} + \omega_{sig}\right)t + \left(\phi_{ref} + \phi_{sig}\right)\right]$$
$$+ \frac{A_{ref}A_{sig}}{2}\cos\left[\left(\omega_{ref} - \omega_{sig}\right)t + \left(\phi_{ref} - \phi_{sig}\right)\right] \qquad \text{Eq. 2.3}$$

The multiplication of the two waveforms contains components at the sum and difference frequencies. When the pump signal is synced to the same phase and frequency as the reference, the second half of Eq. 2.3 simplifies to a DC component. Using a low pass filter, the output of the lock-in produces a DC component where the magnitude is equal to $A_{ref}A_{sig}/2$.

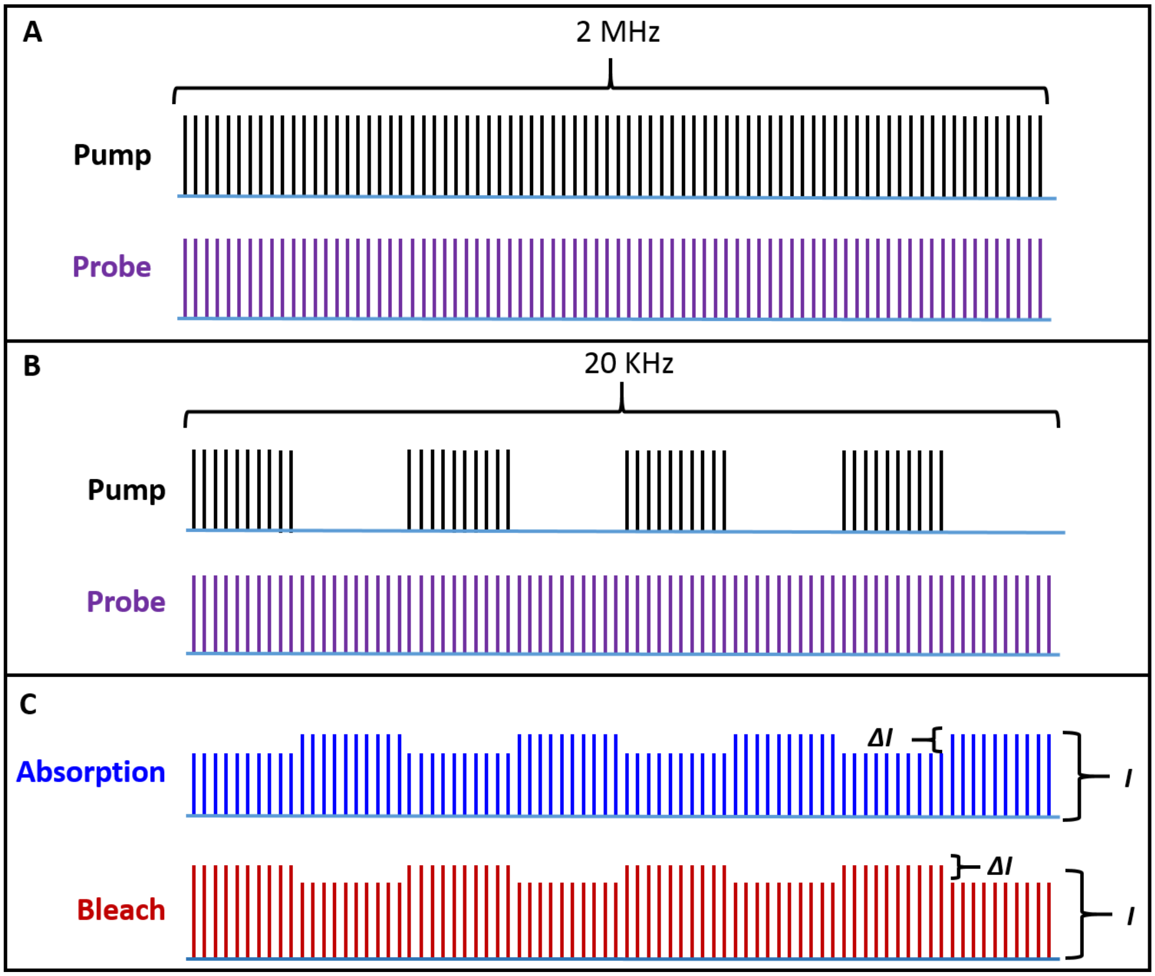

Figure 2.4: Lock-in detection. (A) The pump (black) and probe (purple) pulses are split from the output of the Ti:Sapphire laser and reduced to a repetition rate of 2 MHz by a pair of synchronized AOMs. **(B)** The pump AOM is also modulated at a 50 % duty cycle to a modulation frequency of 20 KHz which serves as the reference for the AOM. The probe is left unmodulated. **(C)** While the balance detector measures the entire pulse train (*I*), the lock-in only outputs signal that is modulated at 20 KHz and therefore only outputs *ΔI*. If less probe light reaches the detector when the pump pulses are 'on', a decrease, or absorption, of signal is detected (blue). If more probe light reaches the detector when the pump is 'on', a bleach in signal is observed.

Figure 2.4 provides an illustration of how this works in our experiment. The pump (black) and probe (purple) pulses are split from the output of the Ti:Sapphire laser operating at 80 MHz and reduced to a repetition rate of 2 MHz by a pair of synchronized AOMs. Only the pump AOM is modulated at a 50 % duty cycle to a modulation frequency of 20 KHz which serves as the reference for the AOM. The probe is left unmodulated. While the balance detector measures the intensity of the entire pulse train (*I*), the lock-in only outputs signal that is modulated at 20 KHz and therefore only outputs *ΔI*. If less probe light reaches the detector when the pump pulses are 'on', a decrease, or absorption, of signal is detected (blue). If more probe light reaches the detector when the pump is 'on', a bleach in signal is observed.

In order to investigate dynamical phenomena occurring at spatially distinct locations from the initial excitation position, we have developed a pump-probe microscopy technique that uses this detections scheme while pumping a nanostructure in one position and probing it in another. The following section describes the logistics of the spatially-separated pump-probe configuration.

2.2 Spatially-Separated Alignment and Calibration

The primary foundation behind the SSPP imaging technique is a pair of independent positioning mechanisms for the pump and probe pulses. The pump pulse is focused by the objective and its position on the sample is controlled by adjusting the Queensgate sample x-y stage (Figure 2.1). The probe beam is positioned independently using the x-y beam scanner (Figure 2.5), which is comprised of a set of two computer controlled mirrors with motorized actuators on both the horizontal and vertical axes. In both dimensions, mirror #1 initially adjusts the angle of the probe beam while mirror #2 compensates to redirect the probe back onto the aperture of the objective.

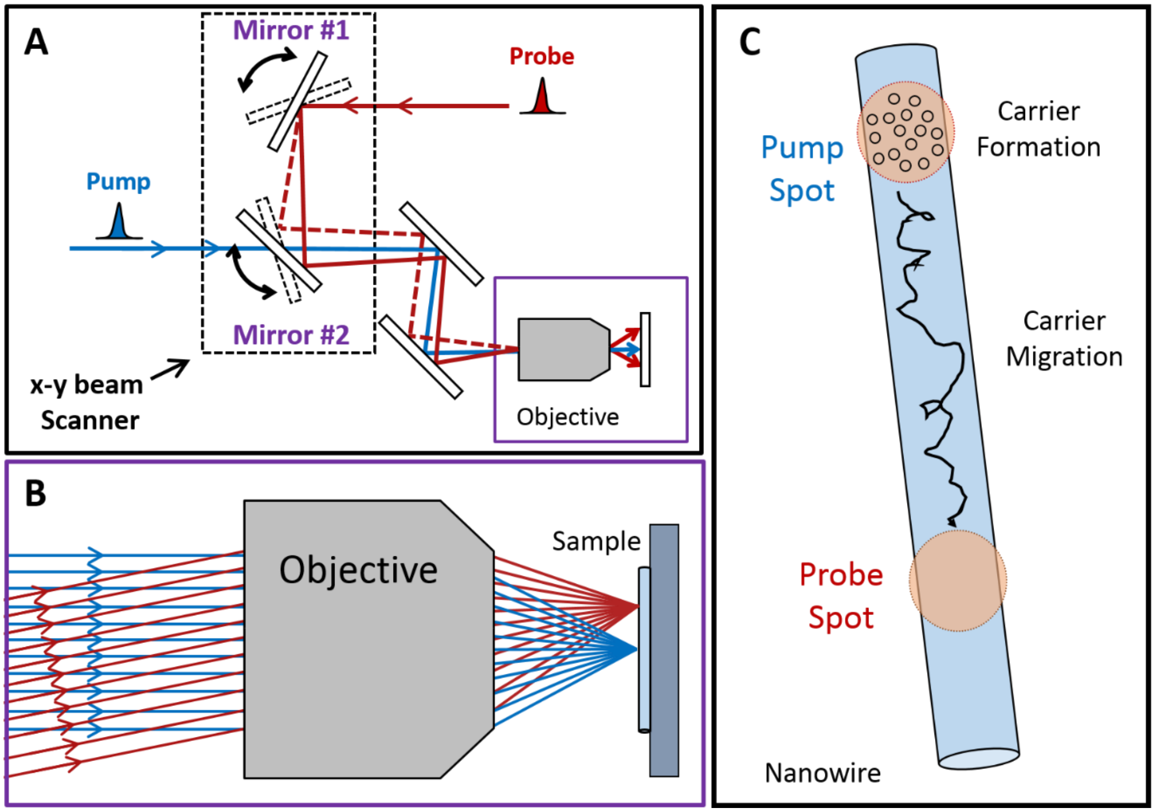

Figure 2.5: Schematic of spatially-separated pump-probe imaging. (A) The x-y beam scanner is a set of two computer-controlled mirrors with motorized actuators on both the horizontal and vertical axes. In both dimensions, Mirror #1 initially adjusts the angle of the probe beam while Mirror #2 compensates to redirect the probe beam back onto the back aperture of the objective. **(B)** Larger illustration of the pump and probe pulses entering the objective at different angles and focusing onto the sample at different positions. **(C)** Basic concept of SSPP method. A nanostructure is photoexcited in one location and probed in another location. In this illustration, electrons are excited by the pump pulse and their migration along the axis of the wire is measured via the probe pulse.

The vertical and horizontal axes of both scanning mirrors are controlled using two motion controllers (Newport: ESP 301). With the pump and probe beams aligned through the objective at angle of 0°and focused at the same position on the sample, the position of each of the 4 mirror axes can be set to 0 on the motion controllers. The horizontal and vertical axes are then independently calibrated under the assumption that motion along one axis does not significantly alter the beam path along the other axis. This assumption is sufficiently validated by the use of gimbal-like mirror mounts that place the center of rotation at the front surface of the optic so rotational adjustments do not cause any beam translation.

Each axis is calibrated one at a time (with the other held at the 0 position) using a MATLAB script that moves the position of Mirror #1 a set distance away from the zero position and then scans the corresponding axis of Mirror #2 while simultaneously monitoring the signal that reaches the detector. This process is repeated at set increments such that the positions of Mirror #1 and Mirror #2 are symmetric about the zero position. Figure 2.6 shows an example for the calibration of the horizontal axis. On the x axis, Mirror #1 is scanned from -0.5 mm to 0.5 mm translation. The y axis shows the horizontal displacement positions for the axis motor on Mirror #2. The magnitude of the signal at each (x,y) position is represented on the color scale shown to the right of the plot in Figure 2.6. For example, when Mirror #1 is at -0.5 mm and Mirror #2 is at 0.6 mm, no signal is measured at the detector because the beam path is no longer going through the aperture of the objective. Once Mirror #2 reaches a position near -0.6 mm, the beam is aligned through the objective and transmitted signal is detected. The maximum value at each x position is used for a linear fit where the slope represents the gear ratio of Mirror #2 to Mirror #1, (i.e. how far the Mirror #2 motor must travel to compensate for motion of Mirror #1).

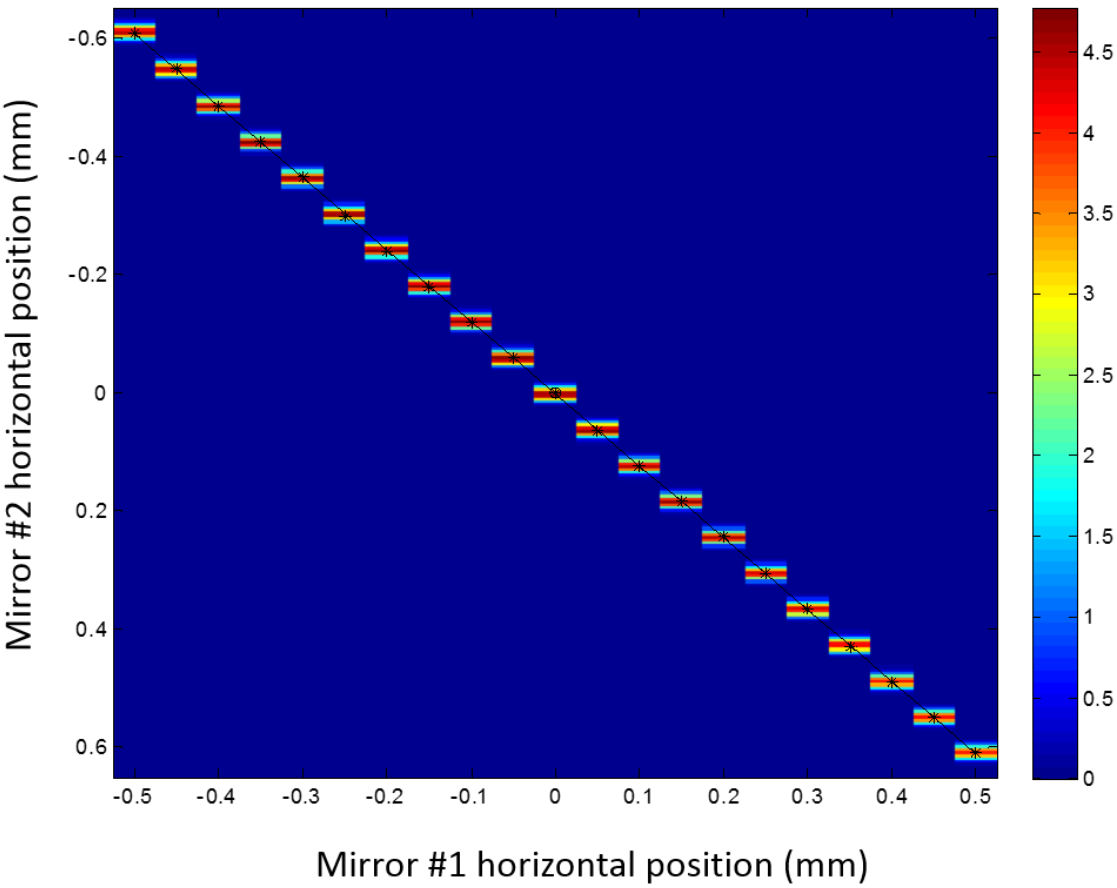

Figure 2.6: Mirror calibration. A typical calibration plot for the horizontal mirror axes. On the x axis, the horizontal position of Mirror #1 is scanned from -0.5 mm to 0.5 mm. At each position, the horizontal position of Mirror #2 is scanned. The magnitude of the signal at each (x,y) position is represented on the color scale shown to the right. The maximum value at each x position is used for a linear fit where the slope represents how far Mirror #2 must travel to compensate for motion of Mirror #1.

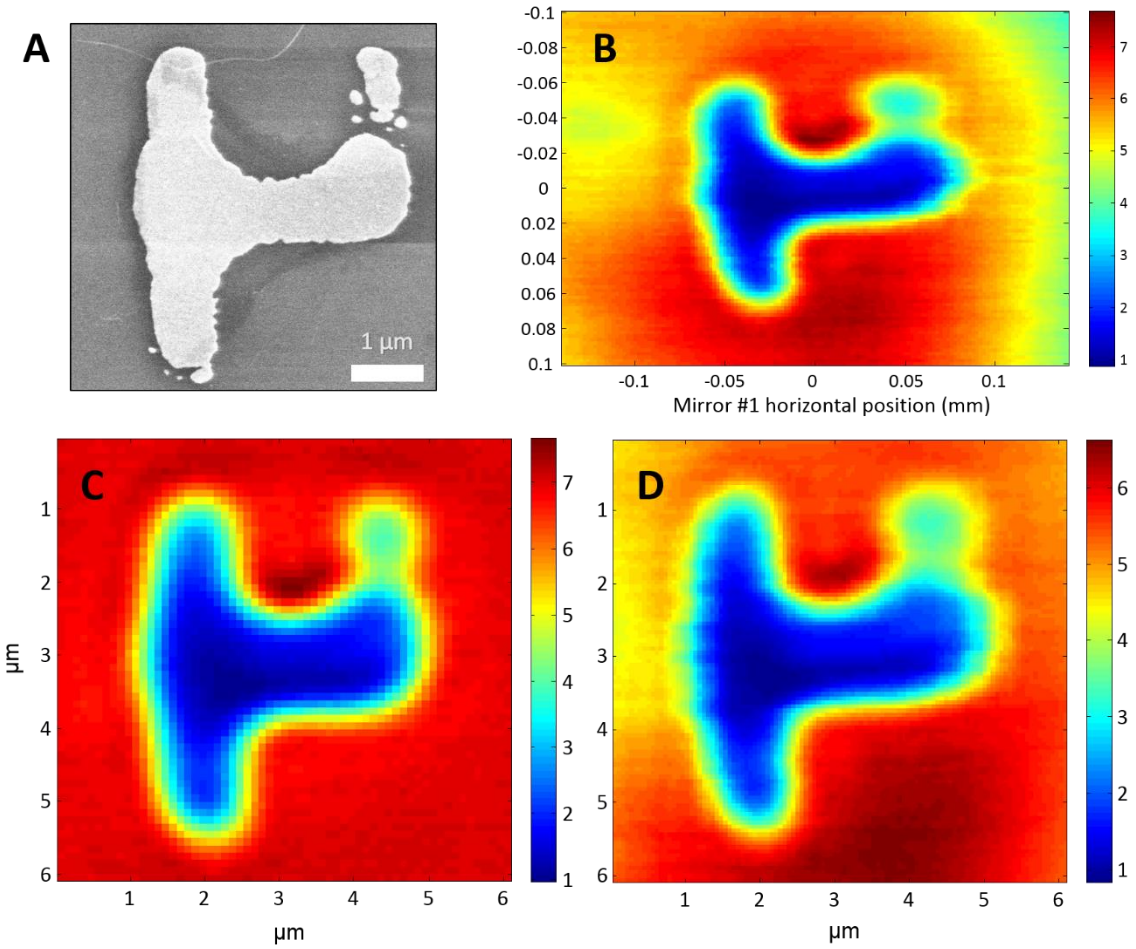

Figure 2.7: Image calibration. (A) SEM image. **(B)** Raw data mirror scanning image. **(C)** x-y sample stage image. **(D)** Calibrated scanning mirror image.

The gear ratio's obtained from horizontal and vertical linear fits are used as input parameters for another MATLAB script that links Mirror #1 and Mirror #2 and sets the gear ratio such that Mirror #2 automatically moves with adjustments to Mirror #1. Other input parameters tell the mirrors how fast to scan and set the scan area in units of mm of Mirror #1 actuator travel. Figure 2.7A shows an SEM image of a feature patterned on a quartz substrate. Figure 2.7B shows the raw data image of the same feature the using the scanning mirror technique. In this image, the x and y axes are plotted in terms of mm of Mirror #1 actuator movement for the horizontal and vertical actuators respectively. In order to correlate mm of actuator movement with microns of movement on the sample, we simply compare the scanning mirror image to an image collected by scanning the Queensgate x-y sample stage with the probe beam held fixed at the zero position (Figure 2.7C). Using another MATLAB script, we can convert mm of actuator movement to microns of spatial movement across the sample (Figure 2.7D) such that both images are displayed in units of microns. Figure 2.7 demonstrates distortion free imaging of the feature using both imaging techniques.

The exact spatial extent that the microscope is capable of imaging is depicted in Figure 2.8. The circular shape of the first image (Figure 2.8A) results from the beam being scanned over the last 1" circular mirror before the beam splitter. Upon replacing the 1" mirror with a 2" mirror, we increased our spatial imaging capabilities (Figure 2.8B). The rectangular shape of the image is due to the rectangular beam splitter where the pump and probe beams are recombined. Further improvements are possible through geometry considerations and placement of the scanning mirrors; however, these measures have not been necessary for any of the experiments thus far.

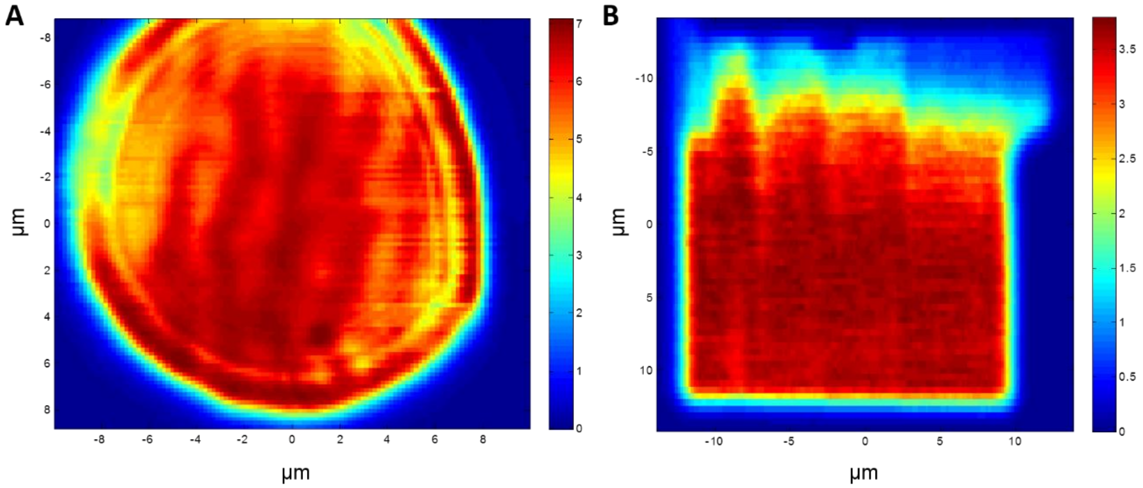

Figure 2.8: Microscope spatial Imaging extent. (A) Initial image of an approximately 18 µm X 16 µm area. The circular image is a result of the beam being scanned across the last 1” mirror before the beam splitter where the pump and probe beams are recombined. This limited the spatial imaging extent to a circular area with a diameter of about 16 µm. **(B)** Spatial extent of the pump-probe microscope after doubling the size of the last mirror. Here the rectangular beam splitter is the limiting optic, allowing for approximately 20 µm X 20 µm uniform imaging capability.

2.3 Data Collection Modes

2.3.1 Spatially-Overlapped Pump-Probe Configuration

Four modes of measurement are possible in this instrument that provide complementary information on the spatial and temporal excited state phenomena in nanomaterials. In the first, the pump and probe beams are spatially overlapped on a specific position on the sample and the pump-probe delay time is scanned using the optical delay stage. The resulting data are similar to the scan illustrated in Figure 2.3. Another example of this operational mode is shown in Figure 2.9A where SOPP transients are collected at three different points along the axis of a silicon nanowire (SiNW) grown with different doping regions as illustrated on the wire diagram on the right. Points of collection are illustrated in the diagram with color-coded circles. Here, the black trace corresponds to data collected in an intrinsic region, while the red trace was collected in the *n*-type region and the blue in the (*ininin)* grating region. The spatial resolution of the microscope enables comparison of dynamics at different regions along a single nanowire. For example, signal in the intrinsic region is much longer lived than the *n*-type or grating regions. This conclusion is further supported by the images in Figure 2.9B.

The second mode of operation is SOPP imaging, where the pump and probe beams are focused at the same focal point, and the x-y sample stage is raster scanned across the focus at fixed pump-probe delays. The spatial variation in the decay kinetics is easily ascertained by collecting images at a series of delay times. This is clear in Figure 2.9B, where one can easily see that in the intrinsic regions of the SiNW, the excited carriers have longer lifetimes than in the *n*-type and grating regions, as corroborated by the SOPP transient delay scans discussed above.

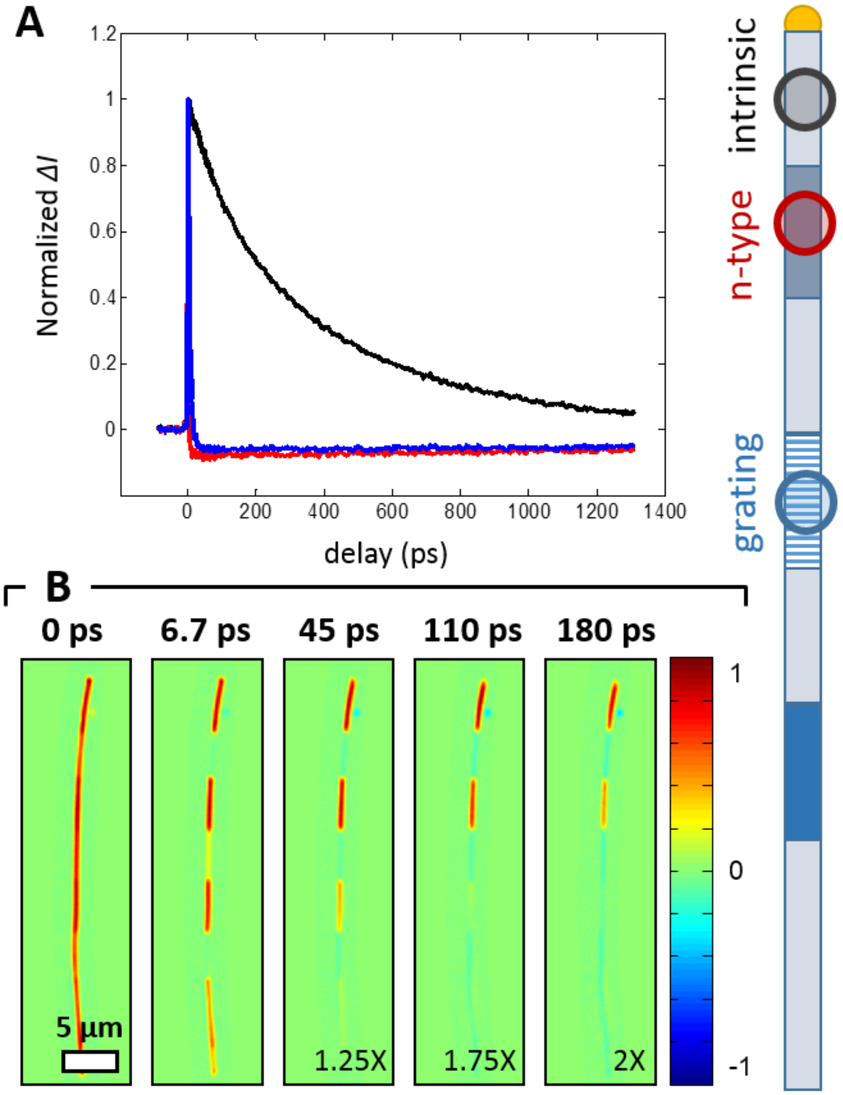

Figure 2.9: SOPP imaging of silicon nanowire grating wires (A) Spatially-overlapped transient decay curves for points along a silicon nanowire grown according to the doping diagram on the right. The colored circles indicate where each transient trace was collected. The black curve was collected in an intrinsic region, the red curve was collected in an *n*-type region, and the blue curve was collected in the (*ininin*) grating region. This is supported by SOPP images of the same silicon nanowire in **(B).** The images were collected at pump-probe delays of 0 ps, 6.7 ps, 45 ps, 110 ps, and 180 ps. Each pump-probe image is depicted using a normalized color scale with the relative amplitudes indicated by the scaling factors in the bottom right corner of each frame.

2.3.2 Spatially-Separated Pump-Probe Configuration

In the third mode the pump and probe beams are separated at a fixed distance (Δ_{pp}) and the delay stage is scanned analogous to the SOPP configuration (Figure 2.9A). For pump-probe experiments, it is important to note that although the probe scanning mechanism alters the path of the probe beam, the geometry is such that the excess path length introduced by the tilt of the first mirror is almost completely compensated with the tilt second mirror. As a result there is little (<0.5 ps) variation in the pump-probe delay as the probe beam is moved. Similarly, experiments using propagating surface plasmon polaritons have shown that this is also not an issue for galvo-scanner methods over length scales of several microns.[7]

An example of SSPP transient collection from our group is shown in Figure 2.10A for single a SiNW.[3] The nanowire is excited by the pump pulse in a single location and the transient data is collected at four pump-probe spatial separations (Δ_{pp}) of 0.0 μm (black squares), 0.56 μm (red circles), 0.87 μm (green triangles), and 1.18 μm (blue inverted triangles). The black squares correspond to data collected in the spatially-overlapped configuration (i.e. $\Delta_{pp} = 0$ μm) while the rest of the data was collected in SSPP configuration. The delayed rise in signal for the SSPP data corresponds to the time it takes for excited carriers to travel a distance of Δ_{pp}.

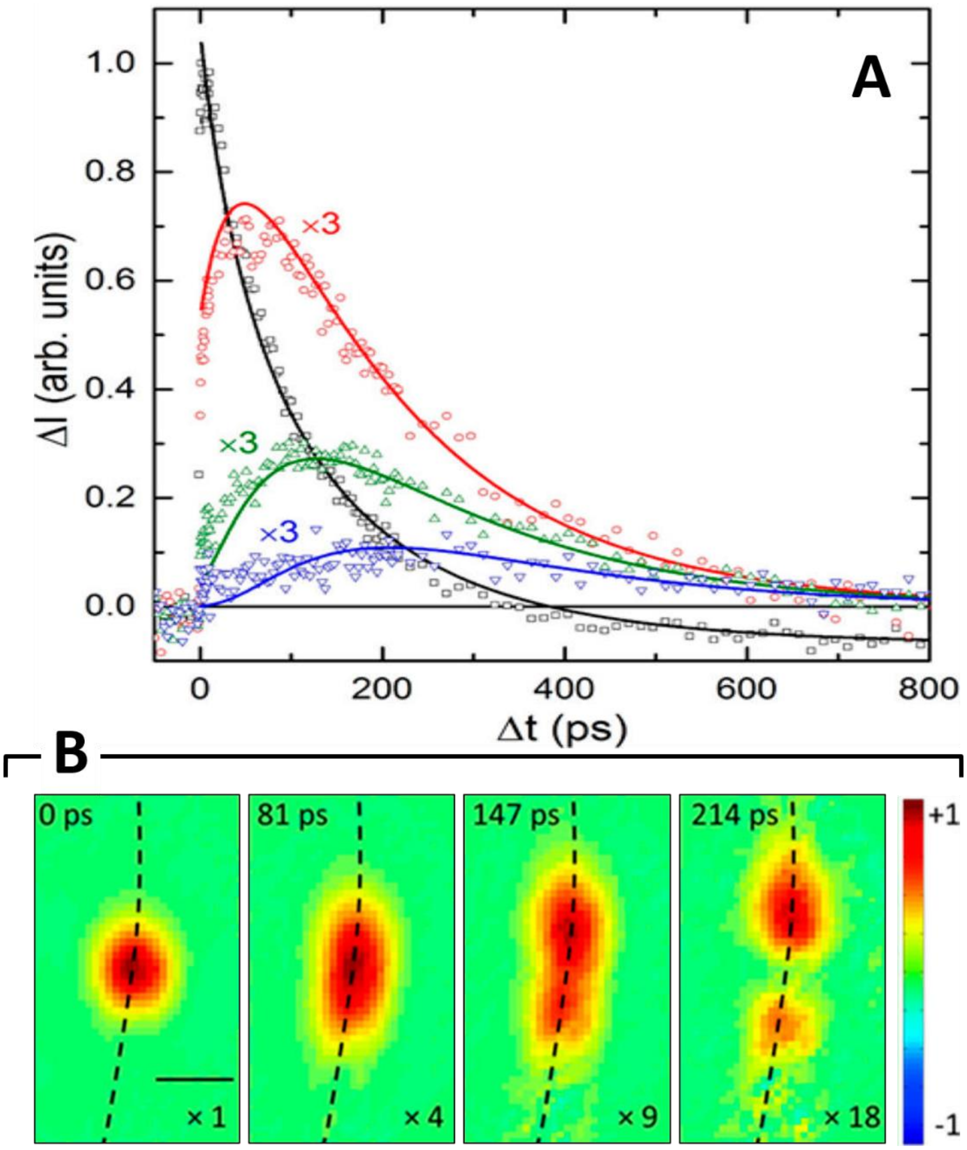

Figure 2.10. Kinetics of charge carrier diffusion. (A) SSPP transient kinetics collected at pump−probe separations (in μm) of Δ_{pp} = 0.0 (black squares), 0.56 (red circles), 0.87 (green triangles), and 1.18 (blue inverted triangles). Solid lines show a global fit of the experimental data. **(B)** SSPP images collected at the delay times denoted in the upper left of each image. The scale bar is 1 μm. Dashed black lines are guides indicating the location of the NW. Each image is depicted using a normalized color scale with the normalization factor denoted in the lower right corner. Adapted from reference [3].

The fourth mode is spatially-separated pump-probe imaging. In this mode, the pump is held fixed at a specific position on the sample and the pump-probe delay is set by the optical delay line. The probe is then scanned over the field of view to provide a spatial map of the excitation at a particular time. By collecting a series of frames over several delay times, one can produce “movies” depicting the spatial evolution of the excitation. In Figure 2.10B, the frames depict the spreading and recombination of photoexcited charge carriers (red positive-going signal) in a single SiNW whose position is represented by the black dashed line. More details and examples of these experiments will be provided in the following chapters.

REFERENCES

1 Gabriel, M. M., Grumstrup, E. M., Kirschbrown, J. R., Pinion, C. W., Christesen, J. D., Zigler, D. F., Cating, E. E., Cahoon, J. F. & Papanikolas, J. M. Imaging Charge Separation and Carrier Recombination in Nanowire p-i-n Junctions Using Ultrafast Microscopy. *Nano Letters* **14**, 3079-3087, (2014).

2 Gabriel, M. M., Kirschbrown, J. R., Christesen, J. D., Pinion, C. W., Zigler, D. F., Grumstrup, E. M., Mehl, B. P., Cating, E. E. M., Cahoon, J. F. & Papanikolas, J. M. Direct Imaging of Free Carrier and Trap Carrier Motion in Silicon Nanowires by Spatially-Separated Femtosecond Pump-Probe Microscopy. *Nano Letters* **13**, 1336-1340, (2013).

3 Grumstrup, E. M., Gabriel, M. M., Cating, E. M., Pinion, C. W., Christesen, J. D., Kirschbrown, J. R., Vallorz, E. L., Cahoon, J. F. & Papanikolas, J. M. Ultrafast Carrier Dynamics in Individual Silicon Nanowires: Characterization of Diameter-Dependent Carrier Lifetime and Surface Recombination with Pump-Probe Microscopy. *Journal of Physical Chemistry C* **118**, 8634-8640, (2014).

4 Grumstrup, E. M., Gabriel, M. M., Pinion, C. W., Parker, J. K., Cahoon, J. F. & Papanikolas, J. M. Reversible strain-induced electron-hole recombination in silicon nanowires observed with femtosecond pump-probe microscopy. *Nano Letters* **14**, 6287-6292, (2014).

5 Mehl, B. P., Kirschbrown, J. R., Gabriel, M. M., House, R. L. & Papanikolas, J. M. Pump-Probe Microscopy: Spatially Resolved Carrier Dynamics in ZnO Rods and the Influence of Optical Cavity Resonator Modes. *Journal of Physical Chemistry B* **117**, 4390-4398, (2013).

6 Mehl, B. P., Kirschbrown, J. R., House, R. L. & Papanikolas, J. M. The End Is Different than The Middle: Spatially Dependent Dynamics in ZnO Rods Observed by Femtosecond Pump–Probe Microscopy. *The Journal of Physical Chemistry Letters* **2**, 1777-1781, (2011).

7 Lo, S. S., Shi, H. Y., Huang, L. & Hartland, G. V. Imaging the extent of plasmon excitation in Au nanowires using pump-probe microscopy. *Optics Letters* **38**, 1265-1267, (2013).

CHAPTER 3: DIFFRACTION-LIMITED TRANSIENT ABSORPTION MICROSCOPY

3.1 Introduction

Disentangling signals from inhomogeneous nanomaterial samples presents a major obstacle for the rational design of new nanoscale devices. The ability to correlate function with underlying structure requires research techniques with combined temporal and spatial resolution. To this end, diffraction-limited pump-probe microscopy has been applied to studies on a particle-to-particle basis to provide insight into the distribution of phenomena emanating from each member of an ensemble. Ultrafast microscopy provides an exclusive view of the structure-function relationship, particularly in systems with variable compositions (e.g. heterojunctions and heterostructures), as well as systems with intricate shapes (e.g. ribbons or tetrapods). Many new modern nanotechnologies are even engaged to exploit secondary structure through mechanical deformation (e.g. bending or stretching) or application of electric and magnetic fields (e.g. piezoelectric) to manipulate properties of the material. The high spatial resolution of pump-probe microscopy enables characterization of the spatial variation in dynamical processes across these complicated structures. For example, the behavior at the end of a nanowire can be compared that of its interior sections. Similarly, pump-probe microscopy is advantageous for characterizing different chemical domains in heterostructures, phase-separated materials, and interfaces, which are often used to separate charges or support energy flow in photovoltaic or similar applications.

Though pump-probe microscopy techniques appeared as early as the 1990s,[1-3] the most common spatiotemporal imaging approaches relied primarily on fluorescence detection (i.e. fluorescence lifetime imaging)[4,5] where lifetime information is obtained by time-correlated single photon counting (TCSPC) or streak camera detection. However, these techniques require emissive samples and can only achieve picosecond time resolution.[6] These two drawbacks have inspired an increased interest in the advancement of pump-probe methods, especially concerning nanotechnology-based research on metallic and semiconducting samples. Pump-probe experiments offer a solution to both limitations. First, their superior temporal resolution is only limited by the duration of the pump and probe pulses, where the use of ultrafast Ti:Sapphire lasers makes femtosecond timescales readily achievable. These timescales are more than sufficient to investigate excited state lifetimes and electron trapping mechanisms in semiconductors as well as probe much faster processes such as Auger or excitonic recombination.

Pump-probe methods are also more versatile than other time-resolved techniques in that they can be carried out in a transient absorption (TA) or reflectivity mode. These configurations have many benefits for nanotechnology research efforts which focus heavily on metallic and semiconducting materials that do not always exhibit fluorescence. For example, with respect to semiconductors, in order for photon emission to occur with high probability, electrons and holes must have the same momentum. This is a limiting issue with indirect band gap semiconductors where the lowest energy transitions from the valence band to the conduction band (and vice versa) must be accompanied by a change in momentum. Because momentum is conserved, transitions at the band edge require simultaneous interaction with a phonon. Thus, the probability of photon emission is lower for indirect band gap semiconductors, and relaxation is dominated by nonradiative processes that are not detectable by fluorescence methods. Transient absorption, on the other hand, is sensitive to both electron and hole distributions, as only one species of carrier is required to induce a change in the absorption of photons. Consequently, TA pump-probe spectroscopy is advantageous for the study of both radiative and nonradiative transitions, in both direct and indirect band gap semiconductors as well as metals, with femtosecond temporal resolution. The following sections highlight and briefly discuss work on nanomaterials in our laboratory using pump-probe microscopy techniques to investigate structure-to-structure differences, variation within structures, and transport through nanomaterials.

3.2 Variation in Dynamical Behavior across an Ensemble

The use of ultrafast microscopy to focus on individual nanoparticles has circumvented the limitation of ensemble averaging inherent to conventional time-resolved spectroscopies. One such example from another group is the use of TA microscopy to characterize the breathing modes in silver nanocubes.[7,8] In previous ensemble measurements, coherent oscillations resulting from the excitation of acoustic phonons decayed after only a few recurrences. On the other hand, the experiments performed on individual particles revealed much longer dephasing times. These studies demonstrated that the ensemble dephasing time is the result of destructive interference from particles with different mode frequencies, as opposed to an intrinsic property of the nanoparticles themselves. Furthermore, particle-to-particle experiments established that the primary mechanism for phonon deactivation is not necessarily a homogeneous process determined by the size of the particle, but rather depends on the mechanical coupling of the nanomaterials to their local environment.

Work from our laboratory[9-11] on silicon nanowires (SiNWs) further emphasizes the importance of pump-probe microscopy for observing dynamical phenomena that might be otherwise overlooked in traditional transient absorption measurements. Figure 3.1 compares the results of ensemble TA spectroscopy with pump-probe microscopy. Both experiments were performed on the same four NW samples, which were grown at four different diameters (40 nm, 50 nm, 60 nm and 100 nm) and collapsed onto quartz substrates. The NWs were photoexcited with a pump pulse around 400 nm and electron-hole recombination was probed by monitoring changes in intensity of a near infrared probe. Figure 3.1A shows a compilation of pump-probe microscopy transient time-delay scans from a series of randomly selected NWs (green traces) with an average diameter of 50 nm. The electron-hole recombination time (τ) was extracted from each kinetics trace,[10] and the distributions of recombination times found for all four NW samples are displayed in Figure 3.1C. By comparison, TA measurements over ensembles of each NW sample (orange trace in Figure 3.1A and orange distributions in Figure 3.1C) consistently yield distributions of recombination times that are 2-3 times faster than those found using the microscopy method.

While both experiments were performed on the same sample, different regions of the sample slide were probed. The microscopy experiments focused on regions near the edges of the samples where individual NWs were easier to select, while the transient absorption measurements were made near the center of the substrate where the higher density of NWs produced larger signals. The origin of the discrepancy is attributed to differences in NW secondary structures occurring between the two regions of the sample slide. As evidenced in Figure 3.1B, the NWs near the edges of the sample are primarily straight; however, the high density of NWs near the center of the sample result in a high fraction of bent NWs. The resulting lattice strain induced by bending deformation, which will be discussed in more detail below, results in faster recombination, which shifts the kinetics distributions obtained from the ensemble TA measurements toward shorter recombination times.

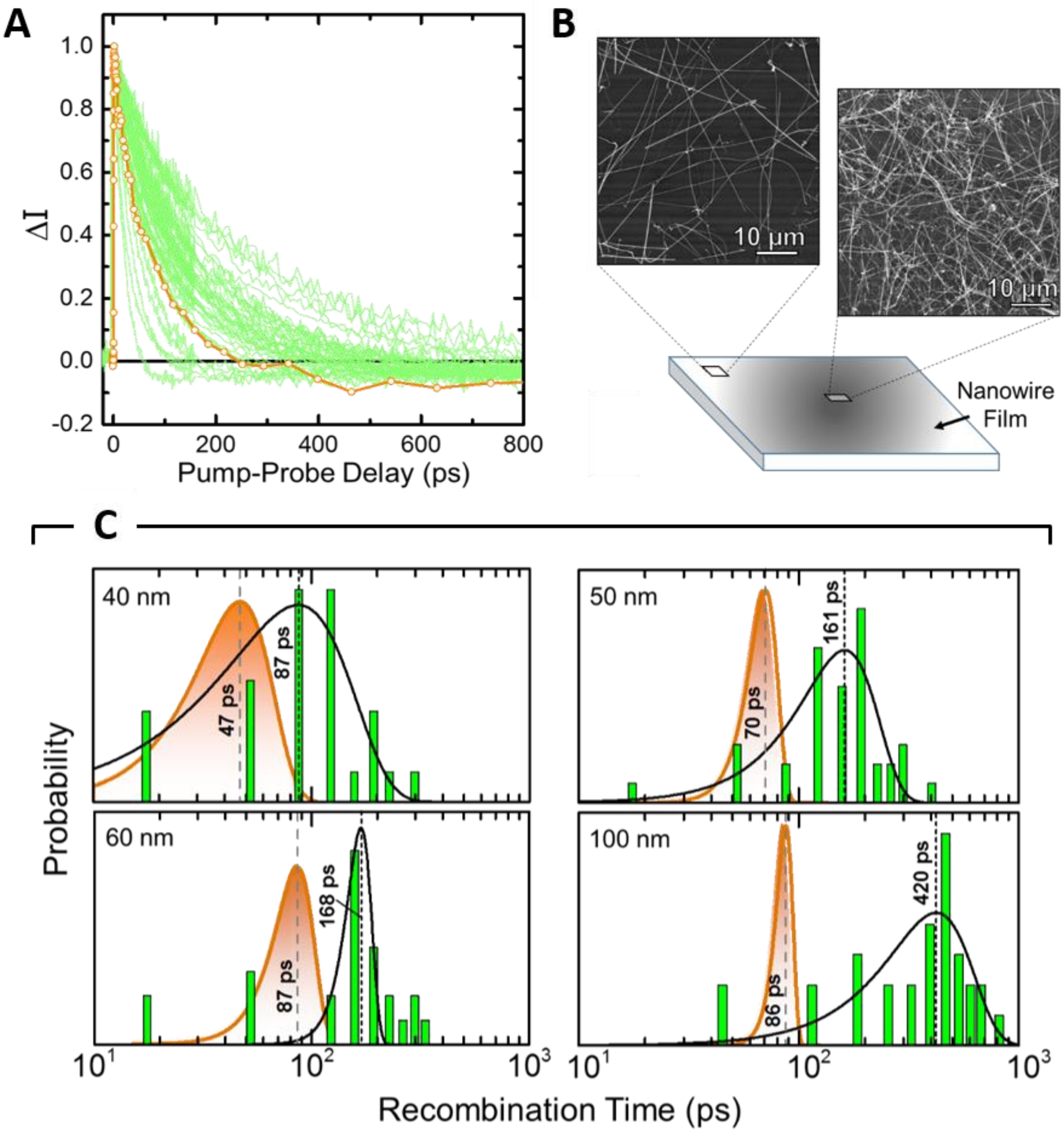

Figure 3.1: **Electron-hole recombination in a collection of Si NWs. (A)** Pump-probe delay scans from the NW sample with 50 nm average diameter. Green traces were obtained randomly selected individual points using pump-probe microscopy. Orange curve shows decay kinetics using conventional TA spectroscopy with a broad-band continuum probe. **(B)** Illustration of the NW film and SEM images of the center and edge of the slide. Microscopy sampled the edges of the film while ensemble experiments sampled the more dense central regions of the slide. **(C)** Lifetime distributions obtained from microscopy (green) and transient absorption spectroscopy (orange) for four samples with different average diameters. (Refs. [9-11])

The average recombination times are consistent with a surface mediated recombination model where τ is related to the NW diameter (d) and surface recombination velocity (S), by $\tau = d/4S$. The surface recombination velocity reflects the quality of the surface. It is often assumed that NWs grown under similar growth conditions have comparable S values. This would imply that the wide variation in transient kinetics is a direct consequence of the distribution of NW diameters present in each sample. Current work in our group indicates that there may be significant variation in S itself across a single sample. Therefore, the cause of the broad lifetime distribution may be much more complicated than simple heterogeneity in the NW diameters. These examples underscore the limitation of conventional ultrafast methods, and the need for high resolution studies such as ultrafast microscopy for disentangling the physical phenomena that contribute to excited state dynamics of complex nanomaterials.

3.3 Variation in Dynamics across Single Structures

Pump-probe microscopy has revealed dramatic spatial variation within individual structures. For example, in experiments from our group on zinc oxide (ZnO), the electron-hole recombination dynamics in ZnO nanorods exhibit differences that stem from spatial variation in the optical resonator modes supported by the varying diameter in the structure.[11-13] The nanorods investigated were 10-15 μm in length with a faceted, hexagonal cross-section that decreased from a few microns at the midpoint to down to 300-400 nm at the ends. Excitation at pump wavelengths of 360-390 nm produces strongly bound excitons that recombine through an electron-hole plasma (EHP) mechanism on the picosecond time scale. This fast band-to-band recombination produces a sharp photoluminescence band at 390 nm.[12-14] In addition to this band-edge mechanism, recombination can occur through a trap-mediated mechanism where photogenerated electrons and holes can become trapped at defect sites and recombine on a much longer timescale. The trap emission band from this process extends across much of the visible spectrum, from 425 nm to about 675 nm.[15]

The high spatial resolution of pump-probe microscopy enabled our group to characterize specific areas of the tapered ZnO rods.[12,13] As shown in Figure 3.2A, the dynamics at the end of the rod (blue curves) are dramatically different from the dynamics observed at the interior (red and green curves). The locations of data collection are indicated by colored circles in the SEM images in Figure 3.2B. Here, the ends show much faster recombination rates than any other point in the structure. The spatial variation is particularly apparent in images obtained by fixing the pump-probe delay and monitoring ΔI as a function of position (Figure 3.2C). At early delays the end of the rod gives rise to the largest signal. The interior regions show a less intense, but spatially structured, signal. As pump-probe delay increases, the intense signal at the end of the rod weakens, becoming less intense than the interior before eventually disappearing altogether. The difference in recombination rates reflects the two different decay pathways. The photoexcited electrons and holes at the end of the rod recombine predominately through the faster EHP mechanism, while in the interior region of the ZnO rods, electron-hole recombination is dominated by the trapping mechanism. Upon first glance, this result is unexpected given that the defect density at the end of rod is likely much higher than the interior sections where there is a more faceted crystal structure.

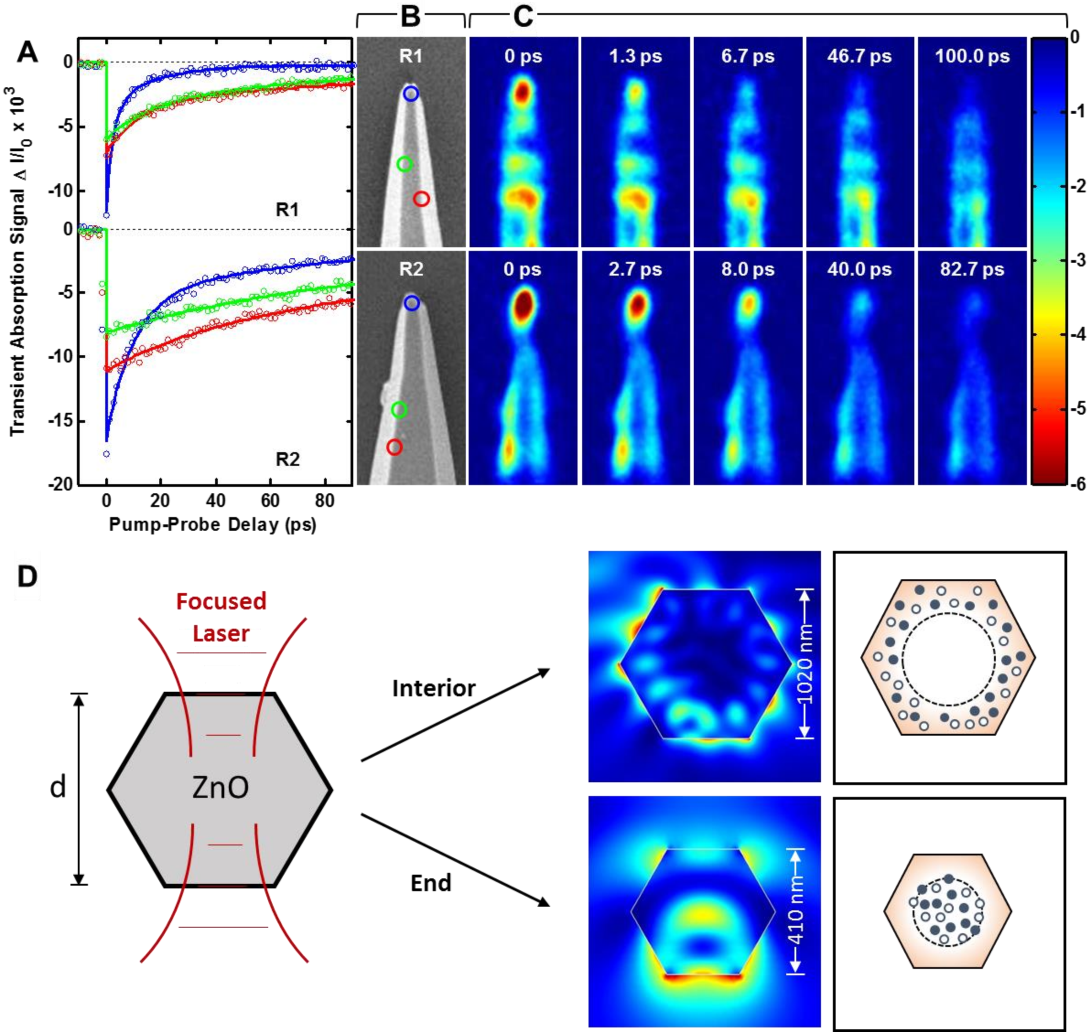

Figure 3.2: Transient absorption microscopy of tapered ZnO nanorods. (A) Decay scans obtained with spatially-overlapped pump and probe beams at the tip (blue) and interior points (red and green). (B) SEM images of the two structures with the locations of the delay scan marked by circles with the corresponding colors. (C) Transient absorption images showing the spatial decay of the photoinduced signal. Rapid decay is observed at the tip of the rod, while slower decay is observed in the interior sections. The spatial structure in the images is the result of the optical resonator modes supported in the cross section of the rod. (D) Optical fields associated with the resonator modes as calculated by FDFD simulations. In the larger cross-section (top) the field is distributed around the periphery of the structure, while in the smaller cross-section (bottom) the field is localized in the core. (Adapted with permission from Refs. [11,12] and [13]. Copyright 2011 and 2013, American Chemical Society)

This counterintuitive effect was investigated in detail and is attributed to the spatial characteristics of resonator modes supported within the cross section of the nanorod.[12,16] At the end of the rod, finite difference frequency domain (FDFD) simulations showed that optical modes have a high degree of Fabry-Perot character. Therefore, a majority of the optical field intensity is localized within the core.[16] In comparison, the diameter increases towards the middle of the rods. The center regions with larger cross-sections predominately support whispering gallery modes and the optical field is localized near the surfaces. Because the photogenerated carrier density is related to the optical field distribution, excited carriers created in the larger sections of the rod are primarily localized closer to the surface where there is a high density of trap states due to imperfect termination of the lattice and dangling bonds. Additionally, band-bending effects resulting at the surface can act to separate the electrons from the holes, resulting in much longer lived signals. Conversely, excitation of electrons and holes near the end of the rod produces a large charge carrier concentration the core. The intense spatial localization of the carriers allows band-edge mechanisms with faster recombination rates to dominate. The dynamic interplay between the optical resonator modes and the electron-hole recombination processes is only revealed through ultrafast microscopy with diffraction-limited spatial resolution and would be difficult, if not impossible, to observe through ensemble-based spectroscopies.

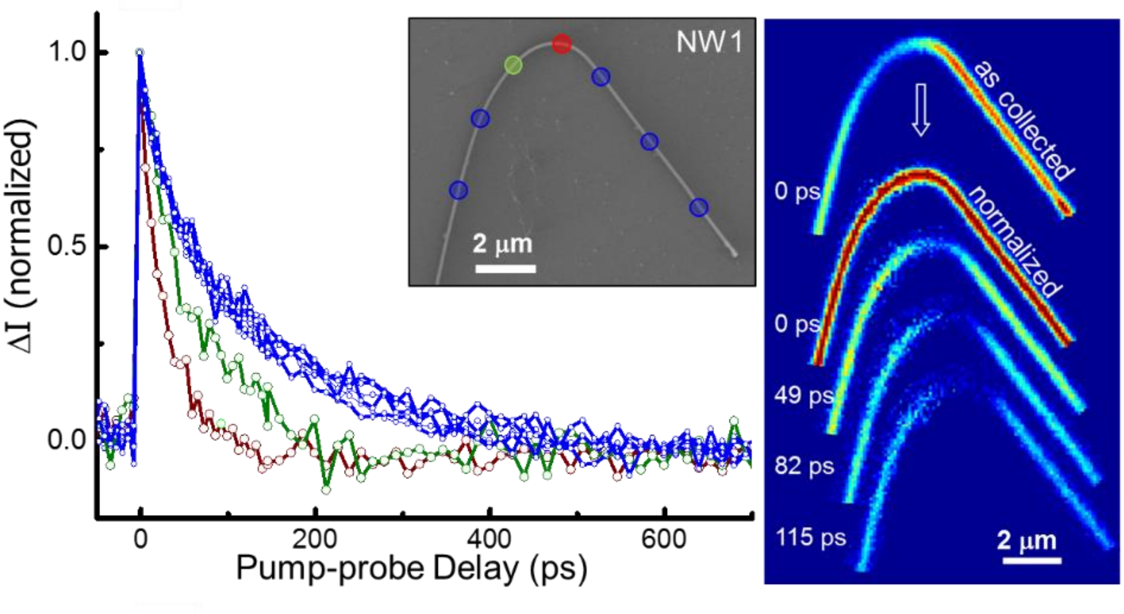

Figure 3.3: Effect of lattice strain on electron-hole recombination dynamics in Si nanowires. Pump-probe decays at different points along a NW. Location of measurements are indicated by corresponding colored circles in the SEM image (inset). At the right is a series of transient absorption images with spatially overlapped pump and probe beams that show rapid loss of the carrier population in the bent region. (Adapted with permission from Reference[11,17]. Copyright 2014, American Chemical Society)

Variation in the electronic dynamics is also evident in quasi- one dimensional NWs, where their high aspect ratios and flexibility make them susceptible to bending. Mechanical deformation can introduce defects and irreversibly alter the crystal lattice. With sufficient material elasticity, deformation can impose a strain that strongly perturbs the electronic structure and band energies. The effects of strain on electronic dynamics have been investigated by several groups. Agarwal *et. al*[18] observed shifts in the photoluminescence bands of bent cadmium sulfide NWs, while Fu et. al.[19] used time-resolved cathodoluminescene to observe exciton drift across strained ZnO NWs.

Investigations of strained and unstrained SiNWs in our group have revealed that bending deformation has a dramatic effect on the electron-hole recombination kinetics in these systems.[17] The deformation of the secondary structure in a single SiNW leads to variation in dynamical response from one point to another, with the bent regions exhibiting consistently faster recombination than straight regions within same nanowire. This concept is illustrated in the kinetics data shown in Figure 3.3 where transient decay curves were collected at various points along a single SiNW. The SEM image in the inset shows the points where data was collected. Blue traces correspond to the blue circles where the NW is mostly unbent. The red and green traces were collected along the bend of the nanowire and exhibit much faster decays. In fact, the recombination rate varies continuously along the bend, with the region of highest curvature exhibiting the fastest recombination.

The spatial variation of these dynamics can be effectively visualized by fixing the pump-probe delay and monitoring ΔI as a function of position as the sample is scanned across the pump-probe focal point. Images collected at increasing pump-probe delay times (0 ps, 49 ps, 82 ps, and 115 ps) map the carrier population along the wire over time, confirming that the recombination rate is largest at the point of highest curvature. Additionally, the images reveal that the variation between the straight and bent regions is not abrupt, but rather evolves smoothly between the two extremes.

Further experiments on NWs deposited on a flexible PDMS (poly-dimethylsiloxane) substrate demonstrate that the effect is reversible, with the recombination rate increasing as the NW is bent and then decreasing as it is re-straightened (Figure 3.4). The observed reversibility of the recombination rate suggests that the effect is not necessarily a result of the introduction of defects into the lattice, which one would expect to be an irreversible process. Instead, the increase in recombination rate is attributed to inhomogeneous lattice strain in the region of the bend which strongly alters the local electronic structure and therefore the intrinsic properties of the wire. For example, it is predicted that areas of tensile strain (along the exterior of the bend), lead to the stabilization of the conduction and valence band energies, whereas compressive strain (along the interior of the bend) increases the potential of the valence and conduction bands.[20] This band bending leads to a localized electric field along the cross-section of the wire within the bent regions which could contribute to field-induced recombination. At any rate, the observation of increased recombination rates within strained SiNWs supports the conclusions presented in section 3.2 where ensemble TA measurements collected at high density regions of a sample where wires are densely packed and strained would result in the observation of much faster overall recombination rates. The high spatial resolution of pump-probe microscopy eliminates this type of bias and enables correlation of physical phenomena with specific structural features within a single nanostructure.

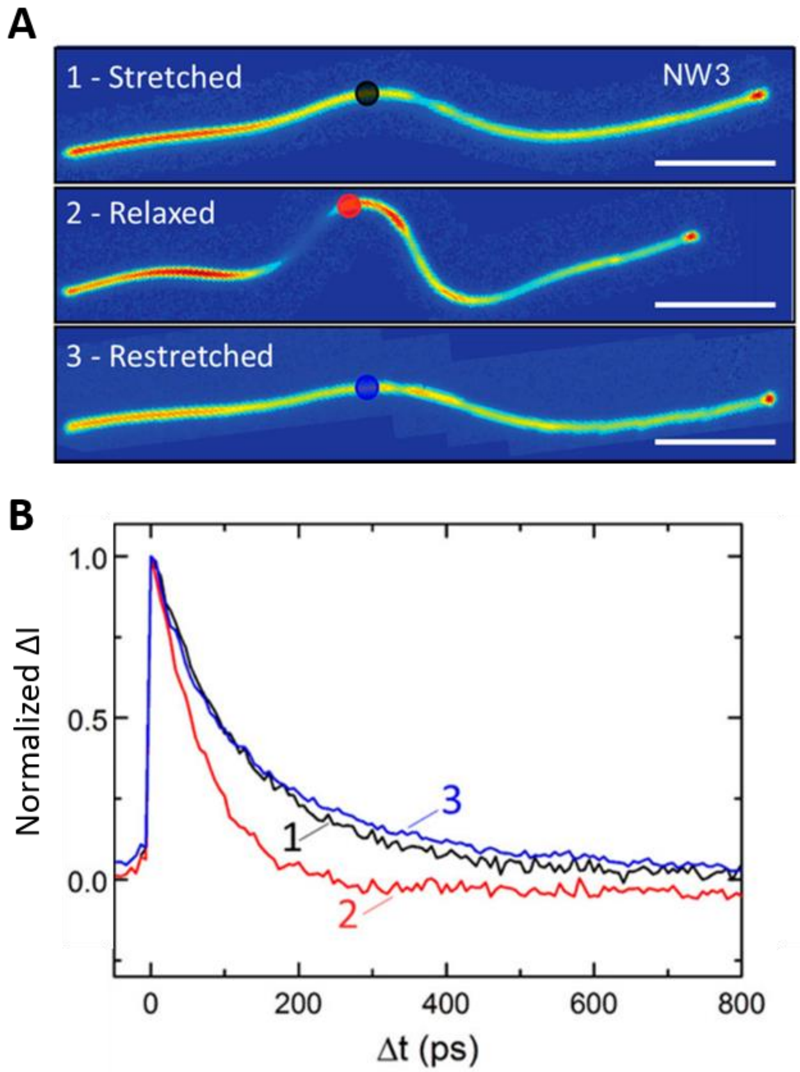

Figure 3.4: Reversibility of the strain-dependent carrier recombination rate. (A) Pump-probe images at Δt = 0 for a SiNW deposited on a flexible PDMS substrate in initial stretched (1), relaxed (2), and re-stretched (3) configurations. Scale bars are 5 μm. **(B)** Transient kinetic traces collected from the same position (indicated by circles in panel A) along the length of NW3 in its initial straight (1), bent (2), and straightened (3) configurations. Adapted from reference [17].

3.4 Transport through Structures

The combined spatial and temporal imaging capabilities of ultrafast microscopy have allowed the direct imaging of transport phenomena in nanomaterial systems. While transport properties are well understood in bulk materials, the motion of charge carriers and phonon propagation in nanostructured systems can be significantly more intricate. For example, many nanoscale electronic components incorporated in emerging technologies operate under high carrier density conditions resulting from heavy doping or high carrier injection conditions. In this regime, many body effects such as carrier-carrier interactions, dopant-carrier interactions, electron screening, and electron-phonon coupling can heavily influence the observed dynamics. Additionally, in such finite-sized structures, surface charging, ionized defects, grain boundaries, and strain more strongly affect the electronic structure leading to a spatial gradient in the energy landscape through which carrier motion evolves. Currently, most experimental information about nanoscale transport in the literature is indirectly inferred from steady-state observations using functional imaging techniques that often require complicated device fabrication and still average over entire structures.[21-25] Unlike the aforementioned methods, pump-probe microscopy offers a contact free approach to investigate transport phenomena, thus eliminating the need for electrical connections or harsh processing steps that can alter the observed electrical properties.

The investigation of carrier motion with micron spatial resolution appeared in the mid 1980’s on 2D quantum wells,[26] and was later extended later to other 2D structures[27-30] and bulk crystals.[29-33] In these experiments, charge carriers are photogenerated in one location by a focused laser pulse. As the carriers diffuse away from the excitation spot they are detected by second focused laser pulse that is spatially offset from the excitation spot. We have used this spatially-separated pump-probe (SSPP) microscopy technique to image the diffusion of photoexcited charge carriers in intrinsic silicon nanowires on diffraction-limited length scales and with ultrafast temporal resolution. This experiment will be described in greater detail in the next chapter.[34] In short, the pump beam is focused at a specific point on an individual nanowire. The lateral position of the probe beam is then scanned over a series of fixed pump-probe delay times, resulting in spatial maps of the free carrier evolution.

Using SSPP microscopy, charge carrier motion can be examined in nanoscale objects with complex inhomogeneous composition and structure. For example, SSPP microscopy has been used for the visualization of carrier motion in a single SiNW encoded with a *p*-type/intrinsic/*n*-type (*p*-*i*-*n*) junction.[35] In these measurements, which will be the focus of Chapter 5, the spatial evolution of the photoexcited charge carrier population is imaged following excitation at the midpoint of the intrinsic region. Additional finite element simulations reproduce the qualitative features of the transient absorption response and provide a detailed picture of the physical factors that govern the carrier dynamics.

More recently, the versatility of the SSPP microscope has been realized through investigations of coherent acoustic phonon mode propagation in a highly-correlated electron material that undergoes a structural phase transition from metallic to insulating upon sufficient photoexcitation. These pump-probe experiments on vanadium dioxide (VO_2) will be discussed further in Chapter 6. All of these experiments directly reveal the complex spatiotemporal processes that occur within a single nanostructure, a rich perspective that neither conventional transient absorption nor electrical or mechanical measurement techniques have been able to provide.

REFERENCES

1 Tamai, N., Asahi, T. & Masuhara, H. Femtosecond Transient Absorption Microspectrophotometer Combined with Optical Trapping Technique. *Review of Scientific Instruments* **64**, 2496-2503, (1993).

2 Tamai, N., Porter, C. F. & Masuhara, H. Femtosecond transient absorption-spectroscopy of a single perylene microcrystal under a microscope. *Chemical Physics Letters* **211**, 364-370, (1993).

3 Dong, C. Y., So, P. T., French, T. & Gratton, E. Fluorescence lifetime imaging by asynchronous pump-probe microscopy. *Biophysical Journal* **69**, 2234-2242, (1995).

4 Krishnan, R. V., Saitoh, H., Terada, H., Centonze, V. E. & Herman, B. Development of a multiphoton fluorescence lifetime imaging microscopy system using a streak camera. *Review of Scientific Instruments* **74**, 2714-2721, (2003).

5 Krishnan, R. V., Biener, E., Zhang, J.-H., Heckel, R. & Herman, B. Probing subtle fluorescence dynamics in cellular proteins by streak camera based fluorescence lifetime imaging microscopy. *Applied Physics Letters* **83**, 4658-4660, (2003).

6 Suhling, K., French, P. M. W. & Phillips, D. Time-resolved fluorescence microscopy. *Photochemical & Photobiological Sciences* **4**, 13-22, (2005).

7 Staleva, H. & Hartland, G. V. Transient absorption studies of single silver nanocubes. *Journal of Physical Chemistry C* **112**, 7535-7539, (2008).

8 Staleva, H. & Hartland, G. V. Vibrational Dynamics of Silver Nanocubes and Nanowires Studied by Single-Particle Transient Absorption Spectroscopy. *Advanced Functional Materials* **18**, 3809-3817, (2008).

9 Grumstrup, E. M., Cating, E. M., Gabriel, M. M., Pinion, C. W., Christesen, J. D., Kirschbrown, J. R., Vallorz, E. L., Cahoon, J. F. & Papanikolas, J. M. Ultrafast Carrier Dynamics of Silicon Nanowire Ensembles: The Impact of Geometrical Heterogeneity on Charge Carrier Lifetime. *Journal of Physical Chemistry C* **118**, 8626-8633, (2014).

10 Grumstrup, E. M., Gabriel, M. M., Cating, E. M., Pinion, C. W., Christesen, J. D., Kirschbrown, J. R., Vallorz, E. L., Cahoon, J. F. & Papanikolas, J. M. Ultrafast Carrier Dynamics in Individual Silicon Nanowires: Characterization of Diameter-Dependent Carrier Lifetime and Surface Recombination with Pump-Probe Microscopy. *Journal of Physical Chemistry C* **118**, 8634-8640, (2014).

11 Grumstrup, E. M., Gabriel, M. M., Cating, E. E. M., Van Goethem, E. M. & Papanikolas, J. M. Pump–probe microscopy: Visualization and spectroscopy of ultrafast dynamics at the nanoscale. *Chemical Physics* **458**, 30-40, (2015).

12 Mehl, B. P., Kirschbrown, J. R., Gabriel, M. M., House, R. L. & Papanikolas, J. M. Pump-Probe Microscopy: Spatially Resolved Carrier Dynamics in ZnO Rods and the Influence of Optical Cavity Resonator Modes. *Journal of Physical Chemistry B* **117**, 4390-4398, (2013).

13 Mehl, B. P., Kirschbrown, J. R., House, R. L. & Papanikolas, J. M. The End Is Different than The Middle: Spatially Dependent Dynamics in ZnO Rods Observed by Femtosecond Pump–Probe Microscopy. *The Journal of Physical Chemistry Letters* **2**, 1777-1781, (2011).

14 House, R. L., Kirschbrown, J. R., Mehl, B. P., Gabriel, M. M., Puccio, J. A., Parker, J. K. & Papanikolas, J. M. Characterizing Electron–Hole Plasma Dynamics at Different Points in Individual ZnO Rods. *The Journal of Physical Chemistry C* **115**, 21436-21442, (2011).

15 House, R. L., Mehl, B. P., Kirschbrown, J. R., Barnes, S. C. & Papanikolas, J. M. Characterizing the Ultrafast Charge Carrier Trapping Dynamics in Single ZnO Rods Using Two-Photon Emission Microscopy. *Journal of Physical Chemistry C* **115**, 10806-10816, (2011).

16 Kirschbrown, J. R., House, R. L., Mehl, B. P., Parker, J. K. & Papanikolas, J. M. Hybrid Standing Wave and Whispering Gallery Modes in Needle-Shaped ZnO Rods: Simulation of Emission Microscopy Images Using Finite Difference Frequency Domain Methods with a Focused Gaussian Source. *Journal of Physical Chemistry C* **117**, 10653-10660, (2013).

17 Grumstrup, E. M., Gabriel, M. M., Pinion, C. W., Parker, J. K., Cahoon, J. F. & Papanikolas, J. M. Reversible strain-induced electron-hole recombination in silicon nanowires observed with femtosecond pump-probe microscopy. *Nano Lett* **14**, 6287-6292, (2014).

18 Sun, L., Kim do, H., Oh, K. H. & Agarwal, R. Strain-induced large exciton energy shifts in buckled CdS nanowires. *Nano Letters* **13**, 3836-3842, (2013).

19 Fu, X., Jacopin, G., Shahmohammadi, M., Liu, R., Benameur, M., Ganiere, J. D., Feng, J., Guo, W., Liao, Z. M., Deveaud, B. & Yu, D. Exciton drift in semiconductors under uniform strain gradients: application to bent ZnO microwires. *ACS Nano* **8**, 3412-3420, (2014).

20 Wu, Z., Neaton, J. B. & Grossman, J. C. Charge Separation via Strain in Silicon Nanowires. *Nano Letters* **9**, 2418-2422, (2009).

21 Howell, S. L., Padalkar, S., Yoon, K., Li, Q., Koleske, D. D., Wierer, J. J., Wang, G. T. & Lauhon, L. J. Spatial Mapping of Efficiency of GaN/InGaN Nanowire Array Solar Cells Using Scanning Photocurrent Microscopy. *Nano Letters* **13**, 5123-5128, (2013).

22 Gutsche, C., Niepelt, R., Gnauck, M., Lysov, A., Prost, W., Ronning, C. & Tegude, F. J. Direct Determination of Minority Carrier Diffusion Lengths at Axial GaAs Nanowire p-n Junctions. *Nano Letters* **12**, 1453-1458, (2012).

23 Gu, Y., Romankiewicz, J. P., David, J. K., Lensch, J. L., Lauhon, L. J., Kwak, E. S. & Odom, T. W. Local Photocurrent Mapping as a Probe of Contact Effects and Charge Carrier Transport in Semiconductor Nanowire Devices. *Journal of Vacuum Science & Technology B: Microelectronics and Nanometer Structures* **24**, 2172, (2006).

24 Allen, J. E., Hemesath, E. R. & Lauhon, L. J. Scanning Photocurrent Microscopy Analysis of Si Nanowire Field-Effect Transistors Fabricated by Surface Etching of the Channel. *Nano Letters* **9**, 1903-1908, (2009).

25 Ahn, Y., Dunning, J. & Park, J. Scanning Photocurrent Imaging and Electronic Band Studies in Silicon Nanowire Field Effect Transistors. *Nano Letters* **5**, 1367-1370, (2005).

26 Smith, L., Wake, D., Wolfe, J., Levi, D., Klein, M., Klem, J., Henderson, T. & Morkoç, H. Picosecond imaging of photoexcited carriers in quantum wells: Anomalous lateral confinement at high densities. *Physical Review B* **38**, 5788-5791, (1988).

27 Ruzicka, B. A., Wang, S., Liu, J., Loh, K.-P., Wu, J. Z. & Zhao, H. Spatially resolved pump-probe study of single-layer graphene produced by chemical vapor deposition [Invited]. *Optical Materials Express* **2**, 708-716, (2012).

28 Ruzicka, B. A., Wang, S., Werake, L. K., Weintrub, B., Loh, K. P. & Zhao, H. Hot carrier diffusion in graphene. *Physical Review B* **82**, 195414, (2010).

29 Cui, Q., Ceballos, F., Kumar, N. & Zhao, H. Transient absorption microscopy of monolayer and bulk WSe2. *ACS Nano* **8**, 2970-2976, (2014).

30 Kumar, N., Ruzicka, B. A., Butch, N. P., Syers, P., Kirshenbaum, K., Paglione, J. & Zhao, H. Spatially resolved femtosecond pump-probe study of topological insulator Bi_2Se_3. *Physical Review B* **83**, 235306, (2011).

31 Ruzicka, B. A., Werake, L. K., Samassekou, H. & Zhao, H. Ambipolar diffusion of photoexcited carriers in bulk GaAs. *Applied Physics Letters* **97**, 262119, (2010).

32 Ruzicka, B. A. & Zhao, H. Optical studies of ballistic currents in semiconductors [Invited]. *Journal of the Optical Society of America B* **29**, A43, (2012).

33 Zhao, H. Temperature dependence of ambipolar diffusion in silicon on insulator. *Applied Physics Letters* **92**, 112104, (2008).

34 Gabriel, M. M., Kirschbrown, J. R., Christesen, J. D., Pinion, C. W., Zigler, D. F., Grumstrup, E. M., Mehl, B. P., Cating, E. E. M., Cahoon, J. F. & Papanikolas, J. M. Direct Imaging of Free Carrier and Trap Carrier Motion in Silicon Nanowires by Spatially-Separated Femtosecond Pump-Probe Microscopy. *Nano Letters* **13**, 1336-1340, (2013).

35 Gabriel, M. M., Grumstrup, E. M., Kirschbrown, J. R., Pinion, C. W., Christesen, J. D., Zigler, D. F., Cating, E. E., Cahoon, J. F. & Papanikolas, J. M. Imaging Charge Separation and Carrier Recombination in Nanowire p-i-n Junctions Using Ultrafast Microscopy. *Nano Letters* **14**, 3079-3087, (2014).

CHAPTER 4: DIRECT IMAGING OF FREE CARRIER AND TRAP CARRIER MOTION IN SILICON NANOWIRES BY SPATIALLY-SEPARATED PUMP-PROBE MICROSCOPY

[Reproduced from Nano letters 13(3), 2013, 1336-40]

We have developed a pump-probe microscope capable of exciting a single semiconductor nanostructure in one location and probing it in another with both high spatial and temporal resolution. Experiments performed on Si nanowires enable a direct visualization of the charge cloud produced by photoexcitation at a localized spot as it spreads along the nanowire axis. The time-resolved images show clear evidence of rapid diffusional spreading and recombination of the free carriers, which is consistent with ambipolar diffusion and a surface recombination velocity of ~10^4 cm/s. The free carrier dynamics are followed by trap carrier migration on slower time scales.

4.1 Background

The motion of charge carriers through nanoscale structures is of central importance to many emerging technologies in nanoscale electronics, optoelectronics and solar energy conversion.[1-4] Interaction of charge carriers with the surfaces, localized defects and electrical contacts in nanostructured devices can have a profound influence on the migration of electrons and holes through a semiconductor structure. These effects have generally been inferred through optical and electrical measurements that average over an entire structure, or an ensemble of structures, and do not directly measure the local carrier motion. To acquire this information, methods with sub-micron spatial resolution and picosecond temporal resolution are needed. The pursuit of such methods is not new, and time-resolved optical microscopies have been applied to a broad range of problems.[5-18] The most common approaches are emission-based but are limited to the picosecond time range and require fluorescent samples. Pump-probe methods provide access to faster time scales but are more difficult to implement. Nevertheless, several recent reports from our group,[5,6] and others,[10-18] describe their extension to microscopy, particularly in far-field configurations.

Here, direct imaging of carrier motion in Si nanowires is accomplished using a pump-probe microscope that can excite a structure in one location and monitor the arrival of photoexcited carriers in another. Similar examples[19-22] have appeared in the literature. In this work, we present results with diffraction-limited pump-probe beams that provide a high (sub-micron) lateral resolution. This unique configuration permits the collection of spatially-separated pump-probe (SSPP) *images*, allowing direct visualization of the carrier population over time. This capability permits us to distinguish between rapid free carrier motion and the slower migration of trapped carriers, as discussed below.

4.2 Experimental

Intrinsic Si nanowires (*i*-Si) were grown by a vapor-liquid-solid (VLS) mechanism[23] using a home-built, hot-wall chemical vapor deposition (CVD) system.[3] For a typical growth run, Au nanoparticles with diameters of ~250 nm were dispersed on Si (100) wafers coated with 600 nm thermal oxide, and these wafers were inserted into the center of a quartz-tube furnace. Nanowires were grown with a total reactor pressure of 40 Torr using a gas flow of 2.00 standard cubic centimeters per minute (sccm) silane and 200 sccm hydrogen as carrier gas. The reactor was held at 600 °C for 2 minutes to nucleate wire growth and then cooled (10 °C/min) to 450 °C for continued wire growth over two hours. For *n*-type Si nanowires (*n*-Si), an additional flow of 10.00 sccm phosphine (1000 ppm in hydrogen) was used to provide a source of phosphorus dopant at a relative concentration of ~200:1 Si:P. After completion of wire growth, nanowires were thermally oxidized at 1000 °C for 60 s in 100 Torr flowing oxygen to form a 5-10 nm-thick thermal oxide. Nanowires were then mechanically transferred onto quartz substrates for microscopy imaging.

The transient absorption microscope is illustrated in Figure 4.1. The 850 nm output of a mode-locked Ti:Sapphire oscillator is split by a 10/90 beam splitter. The higher power beam is frequency doubled to 425 nm and used as the pump while the other is used as the probe. Two synchronized acousto-optic modulator (AOM) pulse pickers reduce the repetition rates of the pump and probe beams to 1.6 MHz, thus ensuring complete relaxation before the next pump-probe pulse pair arrives at the sample. A motorized linear stage controls the time delay between excitation and probe pulses. Both the pump and probe beams are attenuated to 20 pJ per pulse, recombined using a dichroic beam splitter, and then directed onto the back aperture of a 50x (0.8 NA) objective that focuses them to diffraction-limited spots within a single structure. Diffraction-limited spatial resolution in our instrument has been confirmed in two-photon emission images.[5] Images of the UNC logo defined in gold Au on a quartz substrate (Figure 4.1C) obtained using the pump and probe beams (Figure 4.1D) are consistent with diffraction-limited focusing of the two spots, with the pump spot being smaller than the probe. The probe beam is collected by a condenser lens, filtered to remove residual pump light, and directed onto a balanced photodiode. The pump beam is modulated at 10 kHz using the AOM, and pump-induced changes in the intensity of the probe pulse are monitored by a digital lock-in amplifier, producing the measured change in intensity, ΔI, plotted in the figures discussed below. The time-resolution of the instrument is ~500 fs.[5,6]

4.3 Results and Discussion

Initial experiments were performed by measuring kinetics from spatially overlapped pump and probe beams positioned 3-5 μm from the end of three nanowire samples (Figure 4.2). We estimate that photoexcitation by the pump pulse produced ~10^{19}-10^{20} carriers/cm^3 assuming an absorption efficiency of 10-100% at the excitation wavelength of 425 nm.[1,2] Pump-probe transient signals are shown for two *i*-Si wires, NW1 and NW2, and an *n*-Si wire, NW3, with diameters of 160, 210, and 330 nm, respectively. Exact locations of excitation are indicated on the respective SEM images in Figure 4.2. The two *i*-Si NW transient signals exhibit an intense positive going (bleach) feature that becomes weakly negative (absorptive) at several 100 ps before returning to zero signal. These transient signals are similar to pump-probe measurements performed on ensembles of Si nanowires.[24] The signals include contributions from the free carrier (electron and hole) and trap carrier populations and can arise from changes in absorptivity and/or reflectivity upon photoexcitation as well as carrier lensing effects due to the spatially localized excitation.[5,6]

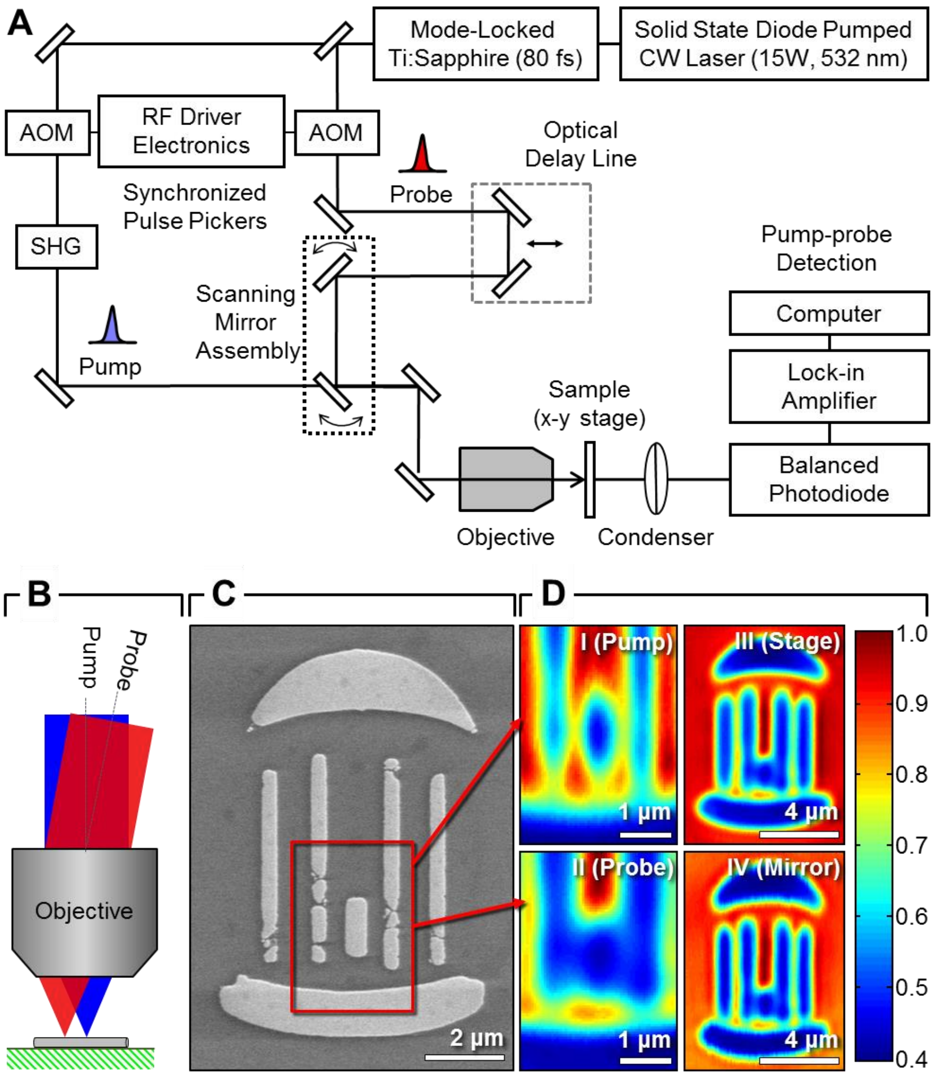

Figure 4.1. Overview of the experimental system. (A) Illustration of the spatially separated pump−probe (SSPP) microscope. An x−y scanning stage positions the structure under the 425 nm pump spot; the 850 nm probe spot is positioned relative to the pump with a scanning mirror assembly. **(B)** Schematic illustration of spatially separated scanning. **(C)** SEM image of the UNC logo defined in Au by electron-beam lithography; scale bar, 2 μm. **(D)** Left, optical transmission images obtained with the pump (I) and probe (II) beams scanned over a lower-center portion of the Au structure, as denoted by the inset box in panel C, that contains an ~400 nm gap; scale bars, 1 μm. Red indicates maximum transmission and blue minimum transmission. Right, comparison of transmission images acquired by raster-scanning the probe beam over the entire Au structure shown in panel C using either the x-y stage (III) or the mirror assembly (IV); scale bars, 4 μm.

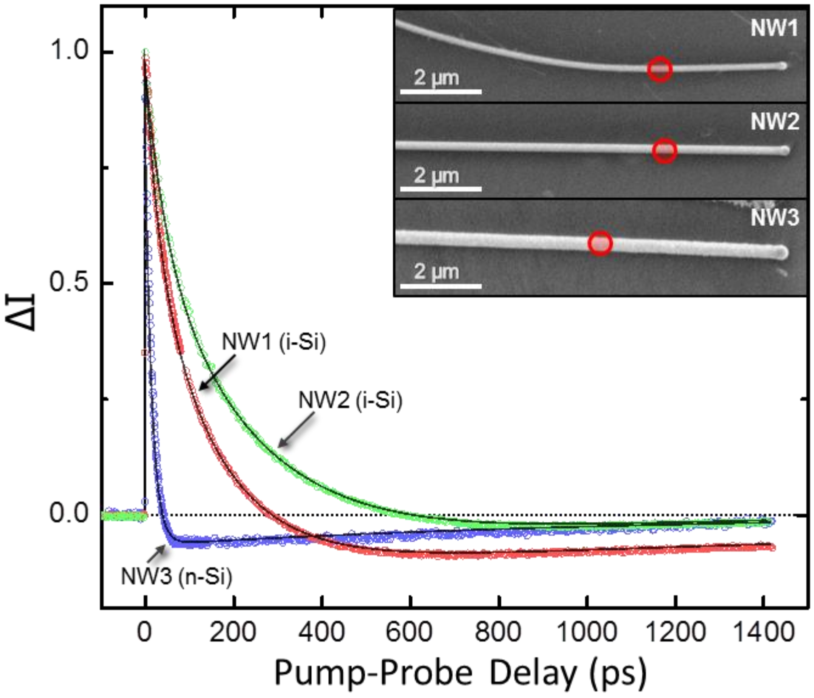

Figure 4.2: Normalized pump-probe microscopy decay kinetics following photoexcitation of a localized region in three different Si nanowires; NW1 (red) and NW2 (green) are intrinsic, NW3 (blue) is *n*-type. All three were fit to a triexponential decay (solid lines, see Table 4.1 for fitting parameters). Inset: SEM images of the three wires showing the location of pump excitation as a red circle; scale bars, 2 µm.

Table 4.1: Parameters used to fit kinetics derived from pump-probe microscopy to a sum of three exponentials, $\Delta I(t)=A_1e^{-t/\tau 1} + A_2e^{-t/\tau 2}+ A_3e^{-t/\tau 3}$.

	$\tau_1(A_1)$	τ_2 (A_2)	τ_3 (A_3)	τ_{avg}[a]
NW1	29.8 ps (0.34)	144 ps (0.78)	2300 ps (-0.12)	67 ps
NW2	46.8 ps (0.34)	248 ps (0.87)	551 ps (-0.23)	112 ps
NW3	1.75 ps (0.06)	15 ps (1.01)	1146 ps (-0.07)	11 ps

[a] Average decay time for the two fast components, i.e. $(1/\tau_{Avg}) = [(A_1/\tau_1) + (A_2/\tau_2)]/(A_1+A_2)$

All three transient signals can be well fit to a superposition of a positive going signal that decays with biexponential kinetics (τ_1, τ_2), and a smaller negative going signal with a much slower decay time, τ_3 (see Table 4.1).[25] The two *i*-Si wires exhibit different decay kinetics, with NW1 showing a faster initial decay (τ_{avg} = 67 ps) than NW2 (τ_{avg} = 112 ps), but with a slower recovery time back to zero signal, τ_3 = 2300 ps (NW1) versus 551 ps (NW2). We attribute the initial decay to free carrier recombination and diffusion and the slower component to trap recombination. For semiconductor nanowires, surface recombination is often the predominant recombination mechanism, and the surface recombination velocity, S, can be calculated from the carrier lifetime, τ, as $S = d/4\tau$, where d is the nanowire diameter.[3,4,26,27] The values derived from this analysis using the measured τ_{avg} are 6.0×10^4 cm/s and 4.7×10^4 cm/s for NW1 and NW2, respectively. These values are upper limits to the actual surface recombination velocities because Auger recombination and carrier diffusion (discussed below) also contribute to the decay. Nevertheless, the similarity between the S values for these two wires suggests that the initial decay is dominated by a surface recombination mechanism.

The *n*-Si wire (NW3) shows a much faster initial decay (τ_{avg} = 11 ps) and recovers with τ_3 = 1146 ps. The origin of the much faster decay in the *n*-Si wire is possibly a result of increased Auger recombination due to the high electron majority-carrier concentration. A second possibility is the presence of an amorphous Si shell surrounding the crystalline core, as suggested by the rougher surface and larger diameter observed in the SEM image. Regardless of the exact origin, the electron-hole recombination rate in this *n*-Si wire is substantially greater than the *i*-Si wires.

In order to characterize the diffusion process in the Si nanowires, we have directly imaged charge carrier motion using SSPP microscopy, in which the structure is excited in one location and probed in another. This experiment is accomplished by incorporating two separate positioning mechanisms for the pump and probe beams. The pump spot is positioned over a particular point in the structure through adjustment of the x-y sample stage. Independent placement of the probe beam is accomplished by directing it through a pair of mirrors with computer-controlled actuators, which vary the angle of the probe beam relative to the fixed pump beam (Figure 4.1C). The use of two (master/slave) mirrors allows adjustment of this angle while keeping the beam centered on the objective aperture. By scanning this angle, the position of the focused probe spot can be displaced from the pump by a distance (Δ_{pp}) of 10-20 μm while still remaining within the objective's field of view. Figure 4.1D compares transmission images taken using the scanning mirror assembly and the scanning stage. Both transmission images reproduce not only the general shape, but also the finer details of the structure, and the similarity of these two images to the SEM image demonstrates the distortion-free imaging capability of this scanning mechanism.

The SSPP microscope can be operated in two different modes. In one operational mode, the delay time between the pump and probe beams is held fixed and the spatial displacement of the pump and probe is scanned, resulting in an image of the spatial variation in the transient absorption signal at a particular time after photoexcitation. SSPP images are shown for three different nanowires (NW1, NW2 and NW3) in Figure 4.3. At early pump-probe delays (near $\Delta t = 0$ ps), the images show an intense positive (red) transient absorption feature, with a spatial extent commensurate with the size of the pump spot. For the *i*-Si wires (NW1 and NW2), this spot spreads rapidly along the long axis of the nanowire, growing 4-5 μm in length during the first 300-500 ps. At the pump-probe delay time in which the transient signal crosses zero (refer to Figure 4.2), a trough appears at the location of the excitation spot that eventually becomes a net negative signal. The final images show the positive features disappearing altogether, leaving behind a negative (blue) region that broadens on a slow time scale. We attribute the rapid evolution of the intense positive signal to the diffusion of free carriers (electrons and holes) out of the excitation volume and the negative signal at long times to trap carrier motion. Rapid electron-hole recombination in the *n*-Si wire (NW3), on the other hand, limits the extent of spatial diffusion and the initial feature shows no substantial broadening.

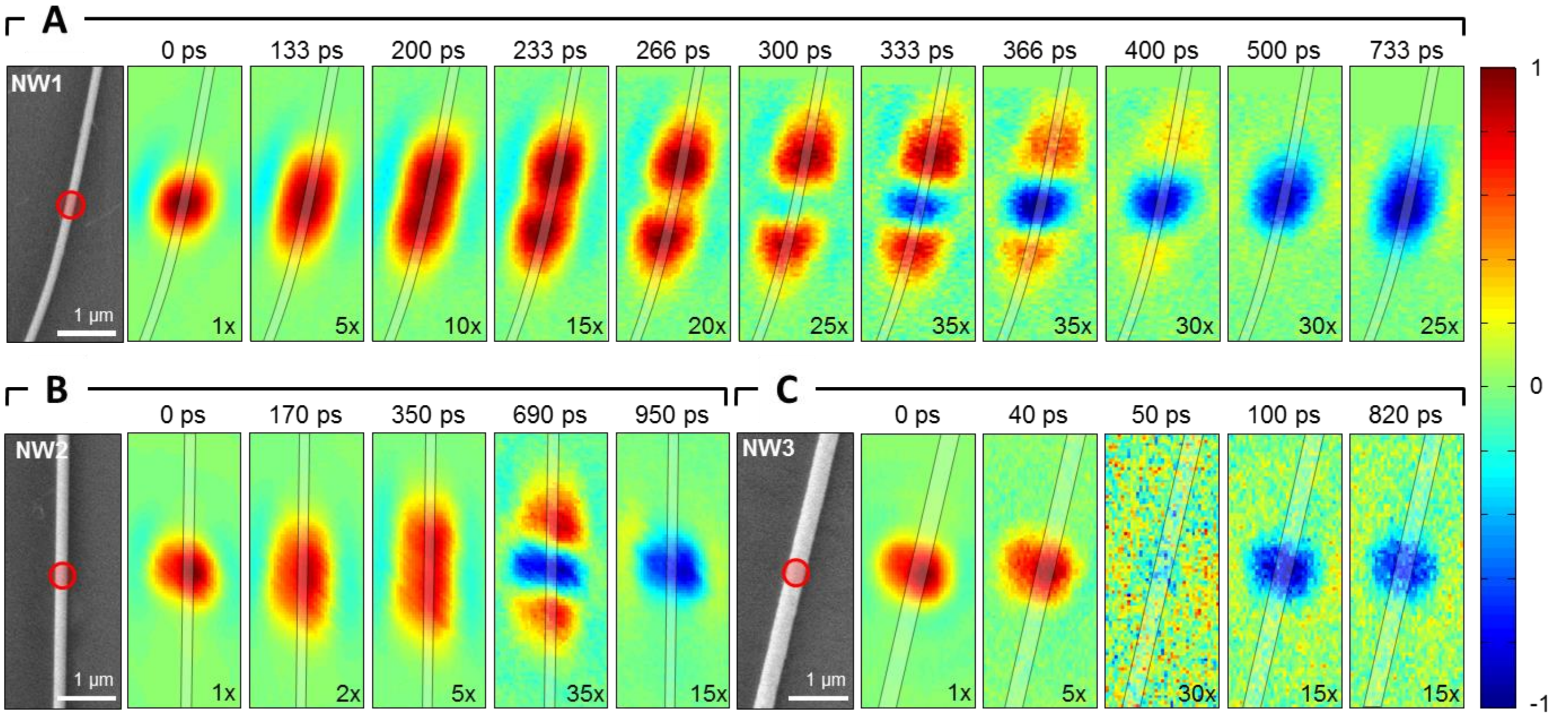

Figure 4.3: Time-resolved SSPP microscopy images. (A) NW1, **(B)** NW2, and **(C)** NW3. Left, SEM images of 5 μm sections of each wire centered around the pump laser excitation spot; (image sizes, 2 μm x 5 μm; scale bars, 1 μm). The location of the excitation spot is depicted by the red circle. For each sample, the tip of the wire lies beyond the top of the image. Right, series of SSPP images acquired at the pump-probe delay times denoted above each image. Location of the nanowire is depicted by the faint lines. Each image is 2 μm x 5 μm and is depicted using a normalized color scale with the relative amplitudes indicated by the scaling factors in the bottom right corner of each image.

The second operational mode of the SSPP microscope fixes the displacement between the pump and probe laser spots and scans the delay time between them. Figure 4.4 shows decay traces for five different separations, Δ_{pp}, along the NW2 nanowire axis. When the pump and probe are spatially coincident ($\Delta_{pp} = 0$), the maximum signal intensity is observed at $\Delta t = 0$ ps. A delayed rise in the signal is observed when the probe pulse is positioned away from the excitation spot ($\Delta_{pp} > 0$), reflecting the time needed for carriers to migrate from the pump region to the probe region. There is also an overall decrease in the intensity of the signal as the pump-probe separation is increased. At $\Delta_{pp} = 2.32$ μm, the overall intensity of the signal makes it difficult to discern the arrival of carriers when depicted on an absolute scale (Figure 4.4); however, when the transients are displayed normalized to their respective maxima (Figure 4.5A), it is clear that free carriers are migrating as far as 2.7 μm from the excitation region. These time-resolved data indicate that the spatially coincident pump-probe transient signals shown in Figure 4.2 are influenced by the diffusional motion of charge carriers away from the excitation region. In principal, the summation of transient signals obtained at different pump-probe separations (shown as the curve Σ in Figure 4.4) should rlect the total free carrier population and remove effects from diffusional motion. This curve is well fit to a superposition of decays with positive and negative amplitudes; however, unlike the $\Delta_{pp} = 0$ μm signal, the decay of the positive signal in the superposition is reproduced by a single exponential with time constant of $\tau = 380$ ps, providing a more accurate measure of the free carrier lifetime. This value for τ gives a revised surface recombination velocity for NW2 of $1.4\text{x}10^4$ cm/s, which is comparable to the value, $S = 7\text{x}10^3$ cm/s, determined for wires grown under similar growth conditions.[3]

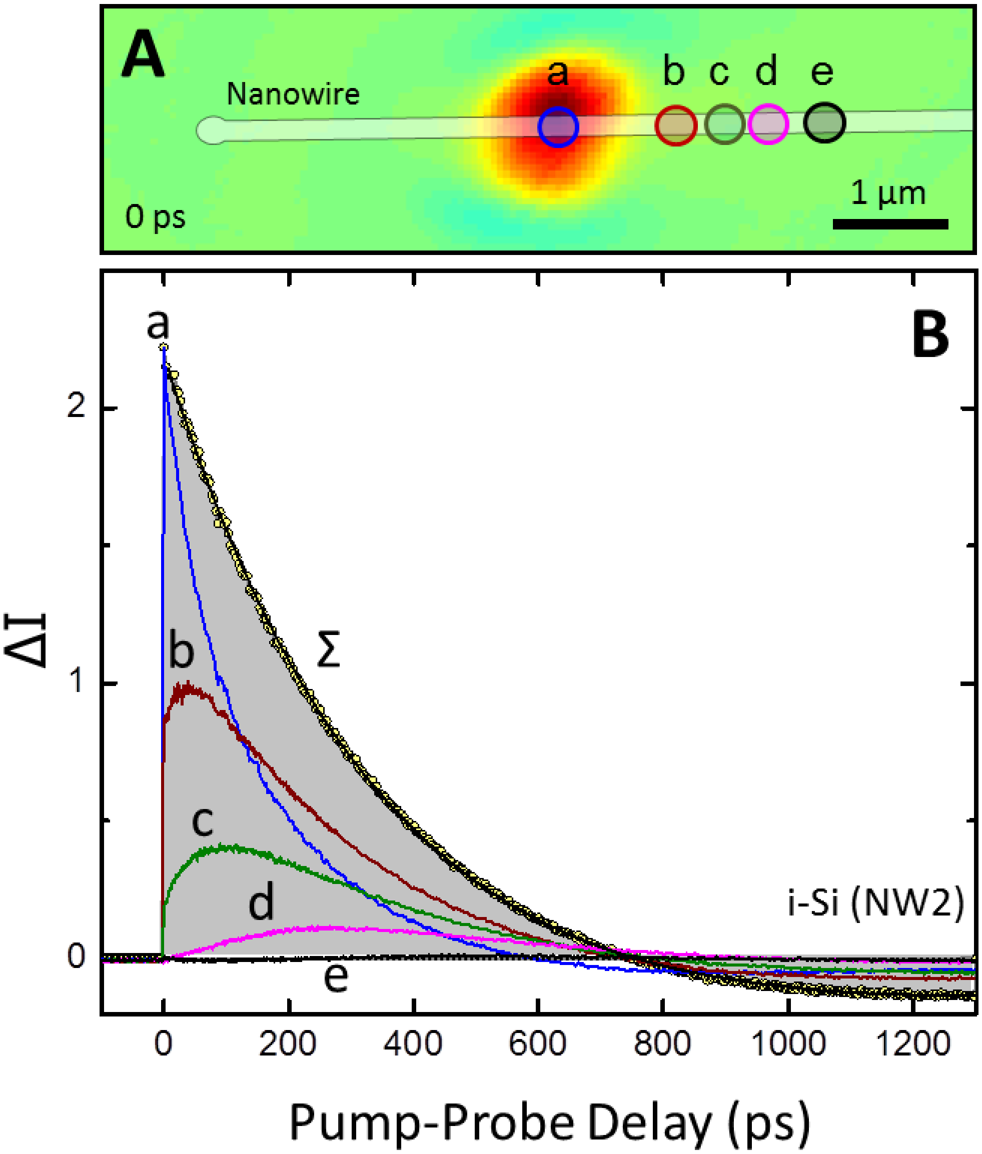

Figure 4.4: Spatially separated pump-probe (SSPP) transient signals. (A) SSPP image obtained at $\Delta t = 0$ overlaid with the spatial locations, a-e, of the displaced probe beam, which correspond to separations of $\Delta_{pp} = 0$, 1.02, 1.45, 1.83, and 2.32 µm, respectively; scale bar, 1 µm. **(B)** Transient signals obtained from NW2 by fixing the spatial separation, Δ_{pp}, between the pump and probe spots and scanning the pump-probe delay. The curves labeled a-e correspond to the positions indicated in panel A. Also shown is the transient signal, labeled Σ, obtained by summation of the individual SSPP signals. Individual data points are denoted by open yellow circles and the solid line is a fit to $\Delta I(t) = A_1e^{-t/\tau 1} + A_2e^{-t/\tau 2}$ with $\tau_1 = 380$ ps ($A_1 = 3.21$) and $\tau_2 = 900$ ps ($A_2 = -1.02$).

In order to quantitatively interpret the charge carrier motion observed with SSPP microscopy, we have developed a simple model that includes ambipolar diffusion of the free carrier population, a recombination process with a single first-order rate constant (1/ τ), and Gaussian profiles that represent the pump and probe laser beams centered at $x = 0$ and $x = \Delta_{pp}$, respectively. In this model, the number of carriers interacting with the displaced probe beam can be written as:

$$N(\Delta_{pp}, t) = \int_{-\infty}^{\infty} I(x - \Delta_{pp}) \eta(x,t) \, dx, \tag{4.1}$$

where $I(x\text{-}\Delta_{pp})$ is a normalized Gaussian centered at $x = \Delta_{pp}$ that describes the intensity profile of the probe beam, and η(x,t) is the carrier distribution created by the pump pulse. At t = 0 this distribution will mirror the intensity profile of the pump beam and spread with increasing time. It can be written as:

$$\eta(x,t) = \int_{-\infty}^{\infty} I(x') \, p(x - x', t) \, dx', \tag{4.2}$$

where $I(x)$ is the optical intensity profile of the focused pump laser beam used in the experiment (represented by a normalized Gaussian) and p(ξ,t) describes the diffusional spreading of N carriers from an initial point located at ξ=0, i.e.:

$$p(\xi, t) = \frac{N}{\sqrt{4\pi D t}} \exp\left(-\frac{t}{\tau}\right) \exp\left(-\frac{\xi^2}{4Dt}\right). \tag{4.3}$$

In this expression τ is the free carrier lifetime and D is the ambipolar diffusion constant.[28]

Figure 4.5 compares this diffusional model (Eq. 4.1) with the experimentally observed SSPP transient signals from NW2. The experimental data shows a steady increase in the spreading of the carrier cloud, reaching several microns in a few hundred picoseconds. The calculated curves (Figure 4.5B) were obtained using the ambipolar diffusion constant for bulk Si ($D \sim 18$ cm^2/s) and a carrier lifetime τ = 380 ps. The calculated curves qualitatively resemble those observed in the SSPP experiment, indicating that diffusional processes in Si nanowires grown by a VLS mechanism are remarkably similar to those in single-crystalline bulk Si materials. There are differences, however, particularly at smaller pump-probe displacements and shorter time delays. In this regime, the model predicts a greater extent of diffusion than observed experimentally, a difference which could be the result of changes in the diffusion constant because of carrier scattering within the nanowires. The exact reasons are currently under investigation.

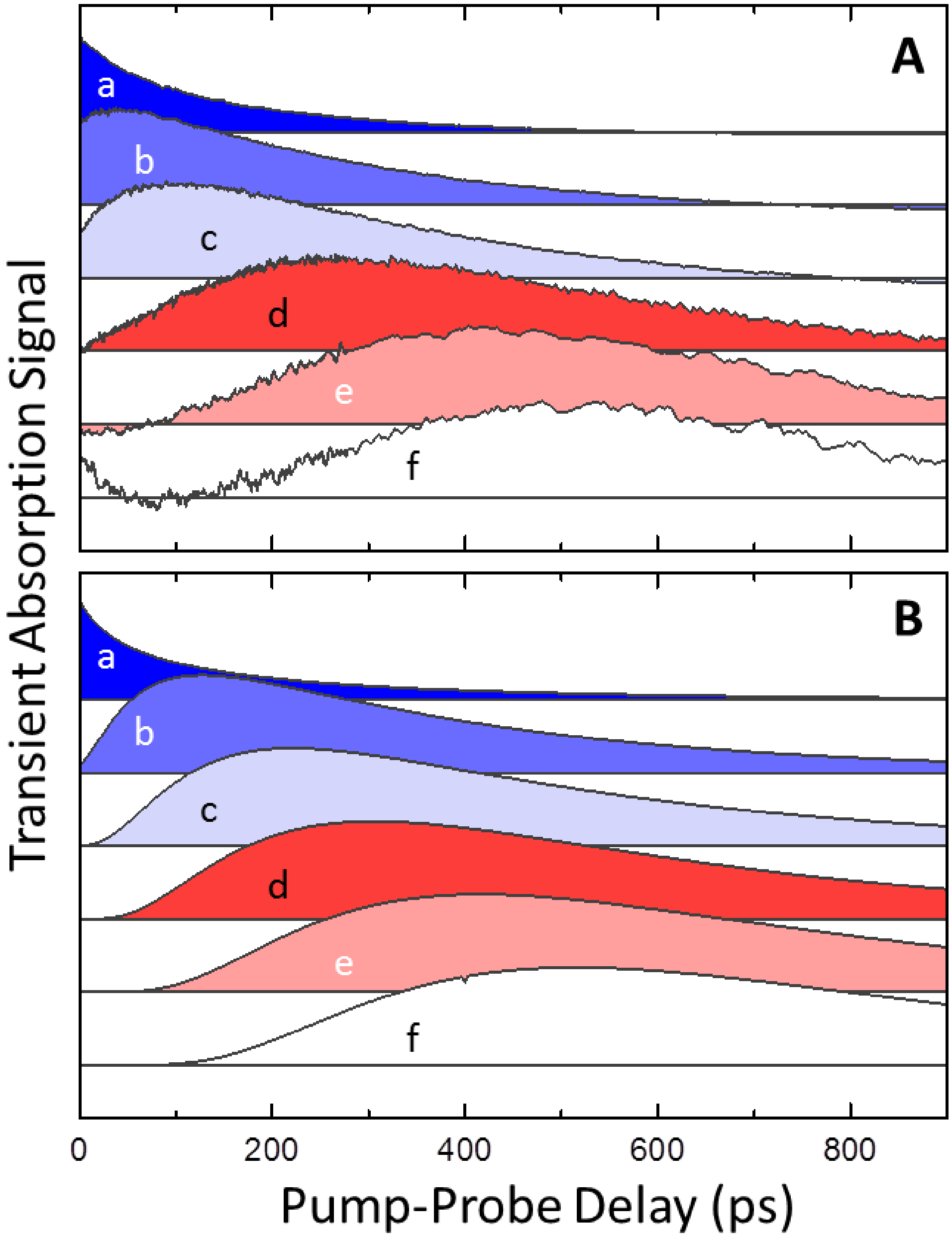

Figure 4.5: Experimental and simulated transient signals (A) Normalized SSPP transient signals obtained from NW2. The curves labeled a-f correspond to separations Δ_{pp} = 0, 1.02, 1.45, 1.83, 2.32 and 2.76 μm, respectively. **(B)** Analogous set of SSPP curves predicted by Eq. 4.1 using D = 18 cm^2/s and τ = 380 ps. The pump and probe laser profiles have FWHM values of 350 nm and 700 nm, respectively, and are included in the simulation curves.

4.4 Conclusion

We have developed a pump-probe microscope capable of photoexciting a single nanostructure in one location and probing it in another. Experiments performed on Si nanowires enable a direct visualization of the charge cloud produced by photoexcitation of a localized spot and spreading of this cloud along the nanowire axis. The time resolved images show clear evidence of rapid diffusion and recombination of the free carries followed by trap carrier migration on slower time scales.

4.5 Acknowledgement

This work was supported by a grant from the National Science Foundation (CHE-1213379). J.D.C, C.W.P, and J.F.C acknowledge support from UNC-Chapel Hill start-up funding.

REFERENCES

1 Kempa, T. J., Cahoon, J. F., Kim, S. K., Day, R. W., Bell, D. C., Park, H. G. & Lieber, C. M. Coaxial multishell nanowires with high-quality electronic interfaces and tunable optical cavities for ultrathin photovoltaics. *Proceedings of the National Academy of Sciences of the United States of America* **109**, 1407-1412, (2012).

2 Kim, S. K., Day, R. W., Cahoon, J. F., Kempa, T. J., Song, K. D., Park, H. G. & Lieber, C. M. Tuning Light Absorption in Core/Shell Silicon Nanowire Photovoltaic Devices through Morphological Design. *Nano Letters* **12**, 4971-4976, (2012).

3 Christesen, J. D., Zhang, X., Pinion, C. W., Celano, T. A., Flynn, C. J. & Cahoon, J. F. Design Principles for Photovoltaic Devices Based on Si Nanowires with Axial or Radial p-n Junctions. *Nano Letters* **12**, 6024-6029, (2012).

4 Kelzenberg, M. D., Turner-Evans, D. B., Putnam, M. C., Boettcher, S. W., Briggs, R. M., Baek, J. Y., Lewis, N. S. & Atwater, H. A. High-performance Si microwire photovoltaics. *Energy & Environmental Science* **4**, 866-871, (2011).

5 Mehl, B. P., Kirschbrown, J. R., Gabriel, M. M., House, R. L. & Gabriel, M. M. Pump-Probe Microscopy: Spatially Resolved Carrier Dynamics in ZnO Rods and the Influence of Optical Cavity Resonator Modes. *Journal of Physical Chemistry B,* ASAP Article, (2013).

6 Mehl, B. P., Kirschbrown, J. R., House, R. L. & Papanikolas, J. M. The End Is Different than The Middle: Spatially Dependent Dynamics in ZnO Rods Observed by Femtosecond Pump-Probe Microscopy. *Journal of Physical Chemistry Letters* **2**, 1777-1781, (2011).

7 House, R. L., Mehl, B. P., Kirschbrown, J. R., Barnes, S. C. & Papanikolas, J. M. Characterizing the Ultrafast Charge Carrier Trapping Dynamics in Single ZnO Rods Using Two-Photon Emission Microscopy. *Journal of Physical Chemistry C* **115**, 10806-10816, (2011).

8 House, R. L., Kirschbrown, J. R., Mehl, B. P., Gabriel, M. M., Puccio, J. A., Parker, J. K. & Papanikolas, J. M. Characterizing Electron-Hole Plasma Dynamics at Different Points in Individual ZnO Rods. *Journal of Physical Chemistry C* **115**, 21436-21442, (2011).

9 House, R. L., Mehl, B. P., Zhang, C., Kirschbrown, J. R., Barnes, S. C. & Papanikolas, J. M. Investigation of ultrafast carrier dynamics in ZnO rods using two-photon emission and second harmonic generation microscopy. *Proceedings of the SPIE* **7396**, 73960G, (2009).

10 Gundlach, L. & Piotrowiak, P. Femtosecond Kerr-gated wide-field fluorescence microscopy. *Optics Letters* **33**, 992-994, (2008).

11 Djurisic, A. B., Kwok, W. M., Leung, Y. H., Phillips, D. L. & Chan, W. K. Stimulated emission in ZnO nanostructures: A time-resolved study. *Journal of Physical Chemistry B* **109**, 19228-19233, (2005).

12 Song, J. K., Willer, U., Szarko, J. M., Leone, S. R., Li, S. & Zhao, Y. Ultrafast upconversion probing of lasing dynamics in single ZnO nanowire lasers. *Journal of Physical Chemistry C* **112**, 1679-1684, (2008).

13 Johnson, J. C., Knutsen, K. P., Yan, H. Q., Law, M., Zhang, Y. F., Yang, P. D. & Saykally, R. J. Ultrafast carrier dynamics in single ZnO nanowire and nanoribbon lasers. *Nano Letters* **4**, 197-204, (2004).

14 Huang, L. B., Hartland, G. V., Chu, L. Q., Luxmi, Feenstra, R. M., Lian, C. X., Tahy, K. & Xing, H. L. Ultrafast Transient Absorption Microscopy Studies of Carrier Dynamics in Epitaxial Graphene. *Nano Letters* **10**, 1308-1313, (2010).

15 Carey, C. R., Yu, Y. H., Kuno, M. & Hartland, G. V. Ultrafast Transient Absorption Measurements of Charge Carrier Dynamics in Single II-VI Nanowires. *Journal of Physical Chemistry C* **113**, 19077-19081, (2009).

16 Fujino, T., Fujima, T. & Tahara, T. Femtosecond fluorescence dynamics imaging using a fluorescence up-conversion microscope. *Journal of Physical Chemistry B* **109**, 15327-15331, (2005).

17 Fu, D., Ye, T., Matthews, T. E., Grichnik, J., Hong, L., Simon, J. D. & Warren, W. S. Probing skin pigmentation changes with transient absorption imaging of eumelanin and pheomelanin. *Journal of Biomedical Optics* **13**, 054036, (2008).

18 Polli, D., Grancini, G., Clark, J., Celebrano, M., Virgili, T., Cerullo, G. & Lanzani, G. Nanoscale Imaging of the Interface Dynamics in Polymer Blends by Femtosecond Pump-Probe Confocal Microscopy. *Advanced Materials* **22**, 3048-3051, (2010).

19 Seo, M. A., Yoo, J., Dayeh, S. A., Picraux, S. T., Taylor, A. J. & Prasankumar, R. P. Mapping Carrier Diffusion in Single Silicon Core-Shell Nanowires with Ultrafast Optical Microscopy. *Nano Letters* **12**, 6334-6338, (2012).

20 Seo, M. A., Dayeh, S. A., Upadhya, P. C., Martinez, J. A., Swartzentruber, B. S., Picraux, S. T., Taylor, A. J. & Prasankumar, R. P. Understanding ultrafast carrier dynamics in single quasi-one-dimensional Si nanowires. *Applied Physics Letters* **100**, 071104, (2012).

21 Ruzicka, B. A. & Zhao, H. Optical studies of ballistic currents in semiconductors. *Journal of the Optical Society of America B-Optical Physics* **29**, A43-A54, (2012).

22 Kumar, N., Ruzicka, B. A., Butch, N. P., Syers, P., Kirshenbaum, K., Paglione, J. & Zhao, H. Spatially resolved femtosecond pump-probe study of topological insulator Bi2Se3. *Physical Review B* **83**, 235306, (2011).

23 Schmidt, V., Wittemann, J. V. & Gosele, U. Growth, Thermodynamics, and Electrical Properties of Silicon Nanowires. *Chemical Reviews* **110**, 361-388, (2010).

24 Kar, A., Upadhya, P. C., Dayeh, S. A., Picraux, S. T., Taylor, A. J. & Prasankumar, R. P. Probing Ultrafast Carrier Dynamics in Silicon Nanowires. *IEEE Journal of Selected Topics in Quantum Electronics* **17**, 889-895, (2011).

25 The n-Si wire transient depicted in Figure 2 has been inverted (i.e. multiplied by -1). The reason this wire shows an initial absorption rather than a bleach is not entirely clear; however, in other experiments on ZnO we observed [Ref. 4] similar sign-changes that stemmed from a Kerr lensing contribution (in addition to absorptive features) to the overall signal. This contribution could either be positive or negative, depending upon the details of the pump-probe overlap. This process could be at play in this wire

26 Mohite, A. D., Perea, D. E., Singh, S., Dayeh, S. A., Campbell, I. H., Picraux, S. T. & Htoon, H. Highly Efficient Charge Separation and Collection across in Situ Doped Axial VLS-Grown Si Nanowire p-n Junctions. *Nano Letters* **12**, 1965-1971, (2012).

27 Allen, J. E., Hemesath, E. R., Perea, D. E., Lensch-Falk, J. L., Li, Z. Y., Yin, F., Gass, M. H., Wang, P., Bleloch, A. L., Palmer, R. E. & Lauhon, L. J. High-resolution detection of Au catalyst atoms in Si nanowires. *Nature Nanotechnology* **3**, 168-173, (2008).

28 Sze, S. M. & Ng, K. K. in *Physics of Semiconductor Devices* 566 (Wiley-Interscience, 2007).

CHAPTER 5: IMAGING CHARGE SEPARATION AND CARRIER RECOMBINATION IN NANOWIRE P-N JUNCTIONS USING ULTRAFAST MICROSCOPY

[Reproduced from Nano letters 14(6), 2014, 3079-3087]

Silicon nanowires incorporating *p*-type/*n*-type (*p*-*n*) junctions have been introduced as basic building blocks for future nanoscale electronic components. Controlling charge flow through these doped nanostructures is central to their function, yet our understanding of this process is inferred from measurements that average over entire structures or integrate over long times. Here, we have used femtosecond pump-probe microscopy to directly image the dynamics of photogenerated charge carriers in silicon nanowires encoded with *p*-*n* junctions along the growth axis. Initially, motion is dictated by carrier-carrier interactions, resulting in diffusive spreading of the neutral electron-hole cloud. Charge separation occurs at longer times as the carrier distribution reaches the edges of the depletion region, leading to a persistent electron population in the *n*-type region. Time-resolved visualization of the carrier dynamics yields clear, direct information on fundamental drift, diffusion, and recombination processes in these systems, providing a powerful tool for understanding and improving materials for nanotechnology.

5.1 Background

A detailed understanding of the factors that govern the motion of mobile charge carriers through nanostructures is critical to the rational design of nanoscale devices.[1-8] Understanding carrier motion is particularly important for nanowires (NWs) encoded with *p*-*n* junctions, which have been widely explored for use in photovoltaic devices based on a range of materials including Si,[9-16] InP,[17] GaAs,[18,19] and CdS.[20,21] Because of the inherently small dimensions, many nanoelectronic components operate at high carrier concentrations resulting from heavy doping or high injection conditions. In this regime, carrier-carrier interactions and other many body effects (e.g. dopant/carrier interactions, electron screening, and electron-hole scattering) must be considered.[22-24] Charge carrier dynamics in nanostructures are further complicated by unintentional electric fields created through surface charging[25,26] or ionized defects. Under conditions of high carrier density and short length scales, our understanding of charge carrier flow through nanostructures draws heavily on experimental observations coupled with sophisticated simulations. Most experimental information of this type is inferred from ultrafast time-resolved measurements that are spatially averaged over entire structures[27-30] or steady-state observations made on single structures or devices using functional imaging techniques.[31-35] While such methods are powerful tools for probing nanomaterials and have been applied with great success, the combination of spatial and temporal information provided by ultrafast microscopy[36-44] enables a characterization of carrier dynamics in relation to specific structural features, and it does so using all optical detection without the need for active electrical connection.

This report describes the use of a femtosecond pump-probe microscopy technique[36-39] to visualize charge carrier motion across axial *p*-type/intrinsic/*n*-type (*p*-*i*-*n*) silicon nanowire (SiNW) junctions. The microscopy results are combined with finite element simulations[15,45] to yield a detailed picture of the charge separation process. Our results reveal characteristics of these junctions that could not be obtained without the spatiotemporal resolution of the microscope. For instance, we find that the lifetime of charge carriers depends sensitively on position in the junction, changing by more than one order of magnitude from the *p*-type to *n*-type segments. Significant variation is also observed across the intrinsic segment, with faster population loss near the boundaries being consistent with deformation of the built-in electric field predicted by finite element simulations. The ultrafast microscope used in this work is capable of exciting a structure in one location and probing it in another, enabling the direct visualization of the charge carrier motion. Pump-probe images obtained following excitation in the middle of the intrinsic segment show that the evolution of the charge carrier cloud is initially dominated by carrier-carrier interactions, causing it to spread at early times through ambipolar diffusion. It is not until 300-400 ps after excitation, when the cloud reaches the boundaries of the intrinsic segment and depletion region, that evidence of charge separation is observed. The insights gained from visualization of the carrier dynamics have direct implications for the synthesis, design, and performance of many nanoscale devices.

5.2 Nanowire Junctions

The SiNW structures used in this study, which were synthesized by the vapor-liquid-solid (VLS) mechanism, are ~100 nm in diameter and consist of a long (>10 µm) *p*-type region followed by a 2 µm intrinsic segment and 3 µm *n*-type region. The *p*-type and *n*-type regions are doped with boron and phosphorus, respectively, at a nominal doping level of 3×10^{19} cm^{-3}. The location of the *p*-*i*-*n* junction is determined by its proximity to the ~100 nm gold catalyst used for VLS growth, which is easily identified at the tip of each *p*-*i*-*n* junction (J1, J2, and J3) in the three scanning electron microscopy (SEM) images in Figure 5.1A. The intrinsic layer grown between the *p*-type and *n*-type segments increases the length of the depletion region, giving rise to an internal electric field that extends across the intrinsic segment. When the layer is short (<100 nm), this field is nearly constant;[45] however, as its length increases, the electric field produced by the junction becomes more complicated.[46] This increased complexity is illustrated by finite element simulations of a *p*-*i*-*n* junction with a 2 μm intrinsic segment, which show significant variation in both the charge density and electric field near the interfaces. The charge density distribution at the *i*-*n* boundary consists of fixed positive charges in the *n*-type material that are partially counter balanced by the accumulation of free electrons within the intrinsic segment (Figure 5.1B). At the *p*-*i* boundary, the situation is reversed, with the fixed negative charges being offset by the accumulation of mobile holes. Thus, the *p*-*i*-*n* junction behaves more like two separate junctions[46] (a *p*-*i* junction and an *i*-*n* junction) that are close enough that partial recombination of the mobile electrons and holes is possible but far enough apart that it is not complete. The close proximity of the positive and negative charge distributions at the interfaces give rise to a spike in the electric field magnitude (10^7 V/m) with a smaller (10^5 V/m) but relatively constant field in the center of the intrinsic segment (Figure 5.1C).

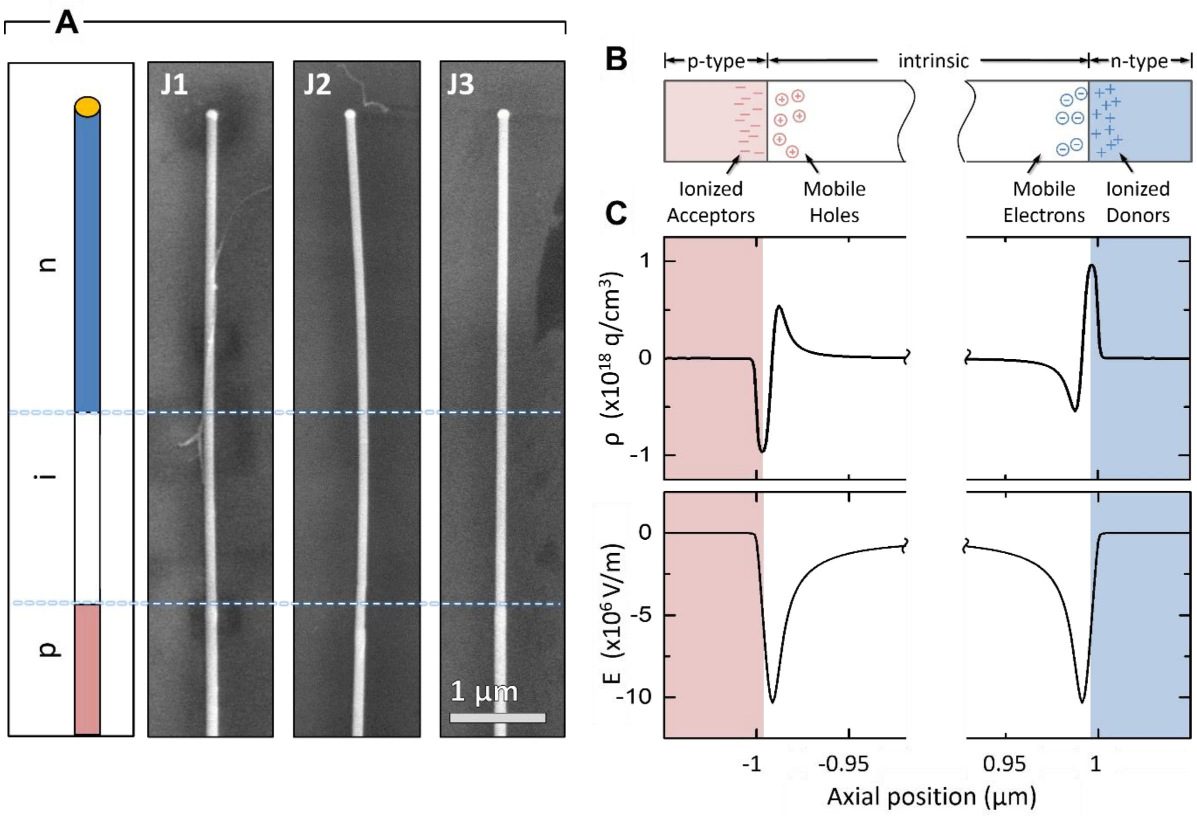

Figure 5.1: Characteristics of silicon NW *p-i-n* junctions. (A) The *p-i-n* axial doping profile (left) compared with corresponding SEM images (right) for three silicon NW structures denoted J1, J2, and J3. Horizontal dashed lines represent junction positions estimated from growth parameters. (**B)** Illustration of charges present within the junction. Mobile holes (circled positive charges) in the *p*-type region (pink) diffuse into the intrinsic segment leaving behind fixed negatively charged acceptors. On the other side, mobile electrons (circled negative charges) in the *n*-type region (blue) diffuse into the intrinsic segment leaving behind fixed positively charged donors. Incomplete recombination in the intrinsic segment leads to residual free carriers at the interfaces. **(C)** Finite element solutions for charge density, ρ, and electric field, E, along the axis of a *p-i-n* junction. The model consists a 100 nm cylindrical wire with a 2 µm *p*-type region, a 2 µm intrinsic region, and a 2 µm *n*-type region. To simulate the characteristics of the *p-i-n* junction, the built-in potential is calculated and applied across contacts placed at either end of the wire. Note the break in the x-axis such that only ~150 nm around each interface is displayed.

5.3 Spatially Resolved Population Decay of Photogenerated Carriers

A free carrier population of ~10^5 electron-hole pairs (5×10^{19} carriers/cm^3) is generated in a localized region of the SiNW by photoexcitation with a 425 nm femtosecond laser pulse focused to a diffraction-limited spot by a microscope objective (100x, 0.8 NA). The decay of this photogenerated population is monitored using a delayed 850 nm probe pulse that is also focused to a diffraction-limited spot by the objective and spatially overlapped with the pump beam. Pump-probe measurements are performed by positioning the focal point of the two beams at a specific location within a single NW structure using a piezoelectric scanning stage. The pump and probe pulses have equivalent pulse energies (2.5 pJ at a 1.6 MHz repetition rate); however, the absorption coefficient for Si at the 850 nm probe wavelength is ~100 times smaller than at the 425 nm pump wavelength. Thus, absorption of the probe beam is negligible compared to the pump, as is customary for transient absorption measurements. After passing through the sample, the probe beam is collected and focused onto a balanced photodiode detector. Pump-induced changes in the probe intensity (ΔI) are then monitored as a function of pump-probe delay using lock-in detection. The microscope is capable of measuring the transient response of a single NW structure with ~700 nm lateral resolution and a time resolution of ~500 fs.[38]

Pump-probe measurements obtained at the center of the intrinsic region of a *p*-*i*-*n* SiNW (green curve in Figure 5.2A) show an initial photoinduced transparency (i.e. bleach) that decays during the first 500 ps after photoexcitation, ultimately becoming a net absorptive signal at long delays. The transient bleach originates from several potential contributions, including changes in the NW absorption that arise from state filling by photoexcited holes in the valence band and electrons in the conduction band or from changes in the NW scattering cross section that arise from a transient modulation of the refractive index due to photoexcited carriers.[47] With either mechanism, the magnitude of the bleach signal reflects the population of free carriers (electrons and holes). The long-lived absorption is attributed to absorption by carriers that become trapped at defect sites in the lattice and to a thermal modulation of refractive index that results from the ~10 ^{o}C rise in temperature caused by carrier relaxation.[47]

Changes in the amplitude of the bleach signal can reflect several dynamical processes. Transient absorption experiments performed on undoped Si NWs show an initial increase in the amplitude of the bleach during the first 500 fs that results from the relaxation of carriers to the band edge.[47] On the picosecond time scale, the decay of the bleach reflects the decrease in the free carrier population within the localized probe spot due to electron-hole recombination and diffusion away from the point of excitation.[38] For indirect band gap semiconductors, electron-hole recombination occurs through a mixture of trap-mediated recombination processes, which take place predominately at the surface in nanostructures. At high doping levels or photoexcited carrier densities, Auger recombination can also become a dominant process; however, in order to minimize its contribution, pump-probe experiments were performed at excitation intensities in which the time scale for recombination was independent of the pump pulse energy.

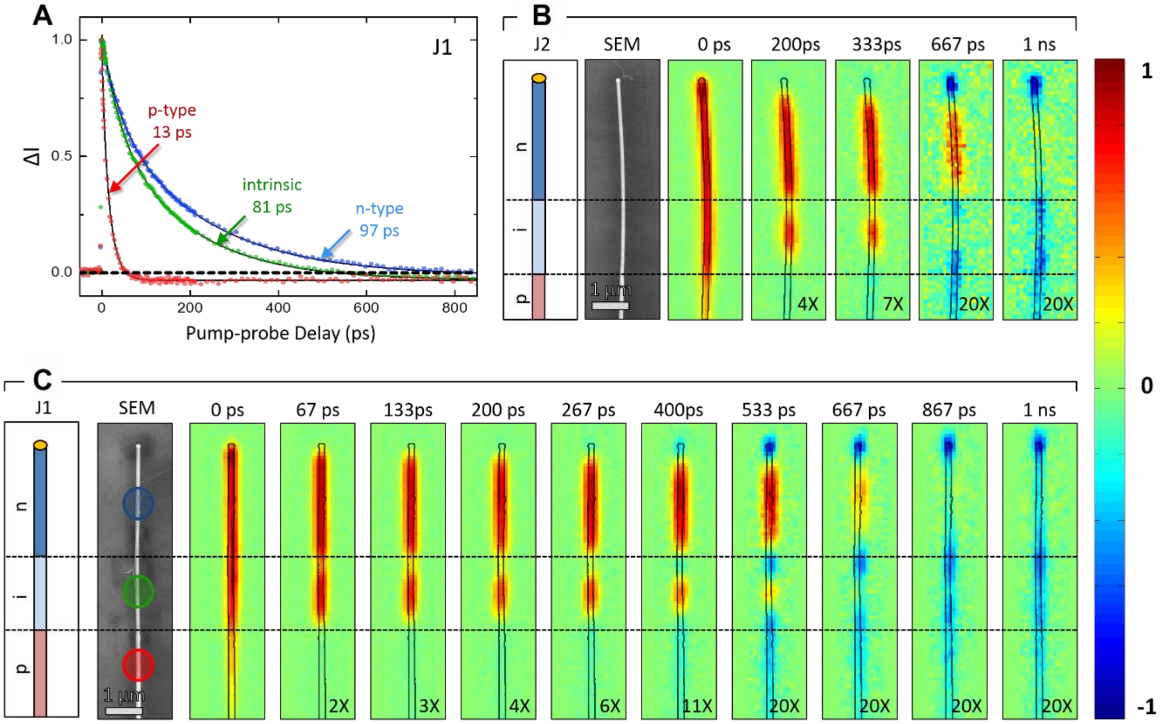

Figure 5.2: Time-resolved measurements with spatially-overlapped pump-probe microscopy. (A) Normalized decay kinetics in a *p-i-n* NW (J1) following localized photoexcitation within the *n*-type region (blue curve), the intrinsic region (green curve), and the *p*-type region (red). The exact locations of photoexcitation are indicated with colored circles on the SEM image in panel c. All three decays were fit (solid traces) to a sum of two exponentials with a negative offset, $\Delta I(t)=A_1e^{-t/\tau 1}+A_2e^{-t/\tau 2}-y_0$, in which the average lifetime was determined by $(1/\tau)_{\text{Avg}} = [(A_1/\tau_1)+(A_2/\tau_2)]/(A_1+A_2)$. **(B)** and **(C)**, Spatially-resolved transient absorption images collected at various pump-probe delays for *p-i-n* silicon NW junctions, J2 and J1, respectively. Doping profile schematics and corresponding SEM images are shown to the left of the pump-probe images. The same scale is used for SEM and pump-probe images, and scale bars are 1 μm. Dotted lines represent the approximate locations of the junction interfaces, and outlines from the SEM images are superimposed on each pump-probe image to represent approximate location of the wire. Each pump-probe image is depicted using a normalized color scale with the relative amplitudes indicated by the scaling factors at the bottom right of each image.

Pump-probe microscopy enables direct observation of the carrier lifetime as a function of position in the *p*-*i*-*n* junction. Excitation of the intrinsic and *n*-type regions exhibit similar decay kinetics (81 ps and 97 ps, respectively) but differ from the transient response in the *p*-type region, which occurs much more rapidly (13 ps). The faster decay in this region suggests a characteristically higher surface recombination velocity for the *p*-type region of the SiNWs. This observation is consistent with passivation of the NW surface by a native oxide layer, which is known to serve as better surface passivation for *n*-type Si than *p*-type Si.[48] While kinetic measurements at discreet spatial locations can be used to quantify decay rates, spatial variation in the lifetime of the free carrier population is more easily visualized by scanning the pulse pair over the structure at a series of fixed pump-probe delay times to generate time-resolved images. Pump-probe images for several time delays are shown for two *p*-*i*-*n* junctions, J2 and J1, in Figure 5.2B and 5.2C, respectively. At early times (0 ps) a positive going (bleach) signal is observed throughout the entire structure. As the pump-probe delay increases, a complex spatial variation in the transient signal emerges, in which three distinct regions that coincide with the *p*-type, intrinsic, and *n*-type segments of the junction are evident. Within the *p*-type and *n*-type regions there is nearly uniform behavior,[49] with the rapid loss of the bleach signal in the *p*-type region and the slower loss in the *n*-type segment being consistent with the pump-probe transients collected at single points (Fig 5.2A). The intrinsic segment, on the other hand, shows distinctly different behavior in the center compared to the two ends, with regions near the *i*-*n* and *p*-*i* boundaries decaying faster. While the faster decay observed at the *p*-*i* boundary is likely influenced by the rapid loss of the bleach in the *p*-type region itself, the *i*-*n* interface is surrounded by longer lived bleach signals, suggesting that the rapid decay is a consequence of the boundary. This spatial variation in the dynamics may be an indicator of the intense electric field at the interfaces predicted by the finite element simulations (Figure 5.1C). The electric field could induce charge separation or enhance free carrier tunneling into trap sites,[50,51] and both processes would appear as a rapid decay of the signal in this region. The results clearly demonstrate that pump-probe microscopy provides far more specific details on the spatial variation of carrier dynamics than can be measured by established methods, such as scanning photocurrent microscopy.[31-34]

5.4 Imaging Charge Carrier Motion

The spatial evolution of the charge carrier cloud along the NW axis is mapped with a spatially-separated imaging mode that uses two separate positioning mechanisms for the pump and probe beams. The pump spot is positioned over a particular point in the structure through adjustment of the x−y sample stage. Independent placement of the probe beam is accomplished by directing it through a pair of scanning mirrors that vary the angle of the probe beam relative to the fixed pump beam, enabling the position of the focused probe spot to be displaced from the pump by a distance of up to 20 μm.

Spatially-separated pump-probe (SSPP) images collected with the pump focused on the center of the intrinsic segments in wires J1 and J3 are shown in Figure 5.3 for several pump-probe delay times. (Figure 5.3). The image at 0 ps reflects the size of the charge carrier cloud produced by the pump pulse. Initially, this cloud spreads symmetrically in both directions along the wire, reaching the boundaries of the intrinsic segment within 300-400 ps after excitation. As the charge cloud approaches the edges of the intrinsic segment, its evolution becomes asymmetric, and over the next 200 ps a bleach appears in the *n*-type region that then persists well beyond 1 ns. In the case of J3, free carriers are discernible in the *n*-type region even at 12.5 ns after excitation. This result is qualitatively different than observations in intrinsic NWs, in which the free carrier population disappears within 600-700 ps due to electron-hole recombination.[38] The persistent signal observed in the *n*-type region is indicative of the formation of a long-lived charge separated state. The absence of a signal from the holes in the *p*-type region could be an indication that transient absorption signal arises primarily from the electrons or that the hole population is distributed over a large region of the *p*-type segment and is simply not detected in this experiment.

The simplest picture of charge carrier motion in a *p*-*n* junction would show electrons and holes drifting in opposite directions with independent, uncorrelated motion as a result of the built-in electric field. However, the evolution of the charge cloud observed by ultrafast microscopy clearly conflicts with this simple picture. Instead, the initial symmetric spreading of the cloud closely resembles carrier diffusion,[38] suggesting that the electric field in the middle of the junction is too weak to influence carrier motion at early times. This result is most likely a consequence of a strong electrostatic attraction between the photogenerated charge carriers that opposes separation of the positive (hole) and negative (electron) charge clouds. At low carrier densities, these interactions are negligible and motion is largely governed by the built-in field of the *p*-*n* junction. However, at higher carrier concentrations, carrier interactions begin to dominate and screen the effects of the built-in electric field. It is because of these carrier-carrier interactions that the neutral electron-hole cloud persists and (ambipolar) diffusion is initially observed. At later times, once the cloud has reached the edges of the intrinsic segment, the built-in field of the junction begins to affect the dynamics, ultimately leading to formation of a long-lived charge-separated state.

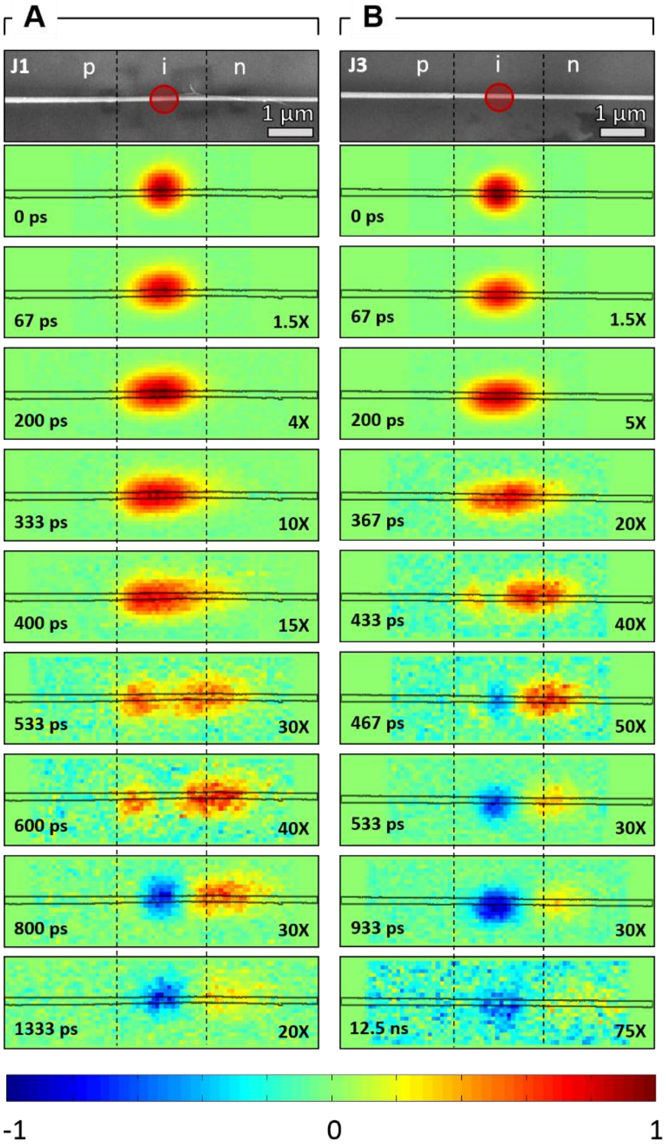

Figure 5.3: Time-resolved measurements with spatially-separated pump-probe microscopy. (A) and **(B)** Evolution of photoexcited charge carrier cloud after excitation in the center of the intrinsic region of SiNW *p*-*i*-*n* junctions J1 (panel A) and J3 (panel B). Top, SEM images of each wire with 1 μm scale bars. The location of the excitation spot is depicted by the red circle. Bottom, series of SSPP images acquired at the pump-probe delay times denoted in lower left of each image. Location of the NW is depicted by black outlines. Each image is displayed using a normalized color scale with the relative amplitudes indicated by the scaling factors at the lower right of each image. Vertical dashed lines mark the positions of dopant transitions in each NW. Animations of the SSPP images for each of the junctions (SAnimation-J1.gif and SAnimation-J3.gif) are provided as online supplementary information.

5.5 Computational Simulations of Charge Carrier Motion at Low and High Injection

The role of carrier-carrier interactions in the motion of the charge carriers is illustrated by a simple time-propagated finite element simulation. The model consists of an intrinsic SiNW 100 nm in diameter and 10 µm in length with an applied electric field along the NW axis to represent the built-in field of an axial *p-i-n* junction (Figure 5.4A). A localized Gaussian distribution (600 nm FWHM) of carriers (electrons and holes) is generated at the center of the wire with a temporal growth profile that corresponds to excitation by an ultrafast laser pulse (500 fs FWHM). The spatial distributions for both the electron and hole populations evolve in time subject to drift and diffusion as well as electron-hole recombination by Auger, surface, and Shockley-Read-Hall mechanisms as described previously.[45]

The charge carrier distribution exhibits qualitatively different behavior depending upon the initial density of photoinjected carriers and the magnitude of the applied field. At the lowest injection level (~10^{15} cm^{-3}), the electrons and holes are easily separated by the applied field (10^6 V/m) and move rapidly in opposite directions, traversing the first 2 μm in ~30-50 ps (Figure 5.4B). The electron and hole populations move with different speeds due to the difference in electron and hole mobilities. The separation of the electron and hole distributions occurs faster than electron-hole recombination and, as a result, almost all (97%) of the carriers are extracted by the electrodes. As the carrier density increases to 10^{16} cm^{-3}, interactions between electrons and holes become increasingly important (Figure 5.4C). At this injection level, charge separation is observed at the edges of the distribution where the carrier density is lower and the field is able to strip the electrons from the right-hand side of the distribution and holes from the left-hand side, accelerating the carriers toward the more positive and negative electrodes, respectively. In the center of the distribution, where the carrier density is higher, charge separation is suppressed by strong electron-hole electrostatic attraction. The quasi-neutral charge cloud formed by the overlapping electron and hole populations (indicated by purple shading) spreads through ambipolar diffusion while simultaneously decaying in amplitude due to electron-hole recombination. Because electron-hole recombination competes with charge separation, only 70% of the carriers are extracted through the electrodes. At the highest densities simulated (10^{17} cm^{-3}), charge separation occurs only in the wings of the distribution (Figure 5.4D), and as a result, only 40% of the carriers are collected by the electrodes. The quasi-neutral charge cloud that remains exhibits a net flow toward the positive electrode as it broadens and decays in amplitude. This directional motion is a consequence of the applied electric field and mobility difference between electrons and holes. The carrier-carrier interactions cause the less mobile carriers (holes) to be dragged along with the higher mobility carriers (electrons). While the carriers move quickly at low carrier density, the time scale associated with the evolution of the quasi-neutral charge cloud observed at high density is significantly slower, occurring over hundreds of picoseconds. This time scale is similar to that observed in the evolution of the SSPP images, implying the spatial evolution observed in the SSPP images corresponds largely to evolution of the quasi-neutral charge cloud.

Although the simulations confirm that charge carrier evolution within the *p*-*i*-*n* junctions is largely governed by carrier-carrier interactions, they also indicate that the junction can separate electrons and holes only when the carrier density drops below 10^{16}-10^{17} cm^{-3}. This regime is ~2-3 orders of magnitude lower than the injection level estimated for the SSPP experiment.

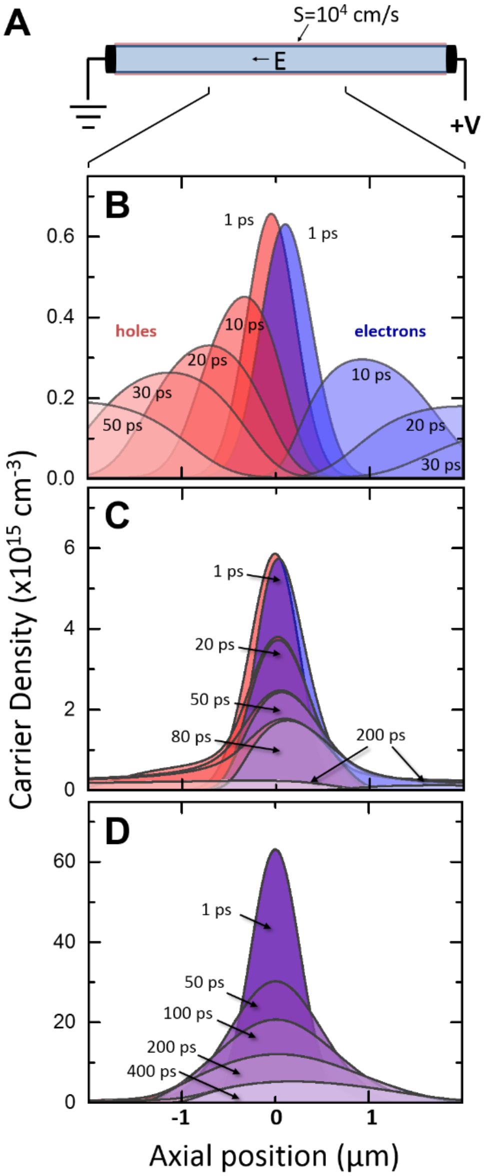

Figure 5.4: Finite element simulation of charge carrier evolution through a NW under applied bias. (A) Diagram of the intrinsic NW finite element simulation. Metal contacts are placed at the ends of a 10 µm long NW with 100 nm diameter. A bias is applied across the wire to induce an electric field with a magnitude of 10^6 V/m. A Gaussian distribution of carriers is generated at the center of the NW (corresponding to an axial position of 0 µm). **(B-D)** Charge carrier evolution along the wire axis under **(B)** low injection (~10^{15} cm^{-3} electrons and holes), **(C)** intermediate injection (~ 10^{16} cm^{-3}) and **(D)** high injection (~ 10^{17} cm^{-3}). Hole distributions are shaded in red and electron distributions in blue with shading getting lighter at longer times. Areas where the distributions overlap appear purple.

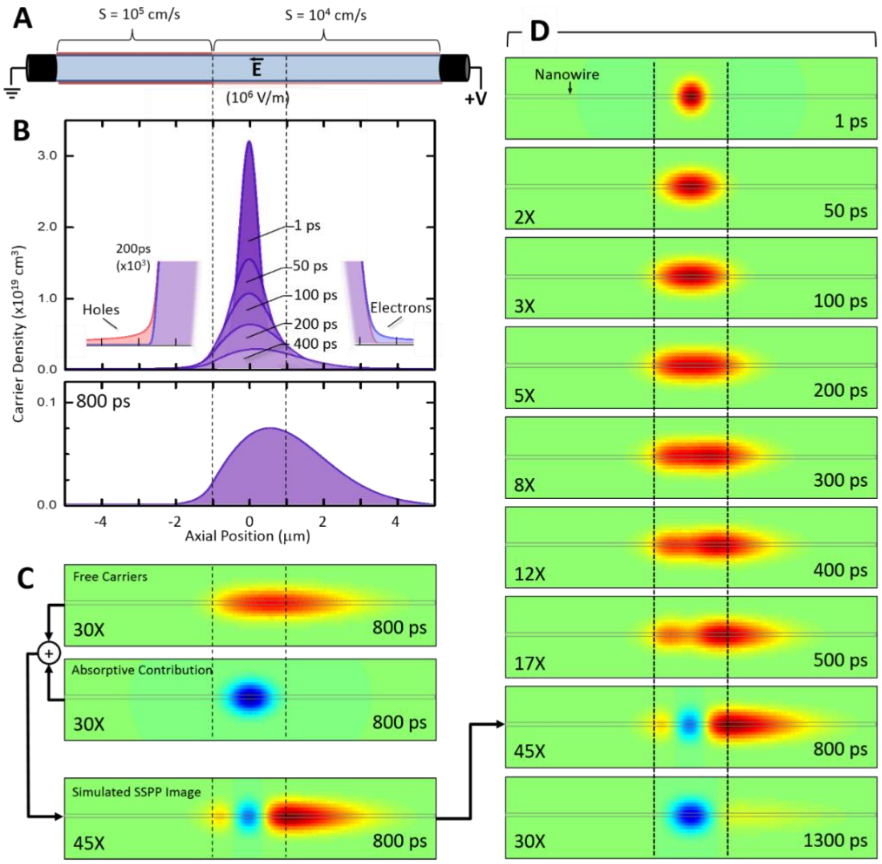

Figure 5.5. Finite element simulation of the spatially-separated pump-probe images. **(A)** Illustration of the finite element simulation model, which consists of a cylindrical intrinsic NW. Metal contacts with applied bias provide the internal electric field. The surface recombination velocity (S) varies along the length of the NW to mimic the spatial variation in the recombination time and enhanced recombination in the *p*-type region. A Gaussian distribution of carriers ($3x10^{19}$ cm^{-3}) is generated at the center of the NW at an axial position of 0 µm. **(B)** Charge carrier evolution along the wire axis. Hole distributions are shaded in red and electron distributions in blue with lighter shading at longer times. Areas where the distributions overlap appear purple. Inset shows the 200 ps time slice with an expanded vertical scale to show the charge separation that occurs in the wings of the distribution. Lower panel shows time slice at 800 ps. **(C)** Construction of simulated image. Upper image depicts the bleach contribution arising from the free carrier (electron and hole) population. Middle image depicts the absorptive contribution (negative signal). Lower image is the simulated SSPP image which is obtained by summing the bleach and absorptive contributions. **(D)** Simulated SSPP images at a series of pump-probe delays.

5.6 Simulation of SSPP Images

While the model depicted in Figure 5.4 is valuable for illustrating the dependence of the carrier motion on photogenerated carrier density, it does not account for the spatial variation in the electron-hole recombination (Figure 5.2). In addition, the photogenerated carrier density in the simulation is significantly smaller than the density created experimentally by the pump pulse, preventing a direct comparison between the simulations and the transient absorption images.

The model illustrated in Figure 5.5A expands upon the previous simulation by including a surface recombination rate that varies along the length of the NW. In order to account for the faster electron-hole recombination observed in the *p*-type segment, the surface recombination velocity for the left-most 4 μm of the NW is 10 times greater ($S=10^5$ cm/s) than the rest of the wire ($S=10^4$ cm/s). Furthermore, the initial peak carrier density is set to $3\text{x}10^{19}$ cm^{-3}, which is comparable to the photogenerated carrier density in the SSPP experiment but is about 500 times greater than highest carrier density depicted in Figure 5.4. As a result of the strong carrier-carrier interactions, the charge cloud spreads as a quasi-neutral packet, exhibiting a net flow towards the positive electrode (Figure 5.5B). While this net shift arises in part from the difference in carrier mobilities, the faster surface recombination in the left-most section of the wire also contributes to the asymmetry of the carrier packet evolution. Charge separation is also observed but only in the wings of the distribution where the carrier density is low enough that the electric field can overcome the carrier-carrier interactions (Figure 5.5B, insets). Approximately 1% of the electrons and holes are separated in this manner, with the remaining carriers recombining within the first nanosecond after excitation.

To facilitate direct comparison of the experiment and computational model, simulated SSPP images are constructed as illustrated in Figure 5.5C for the 800 ps time frame. The bleach signal (red) resulting from free carriers is obtained by convolving the density profile obtained from the simulations with a Gaussian (650 nm FWHM) transverse to the NW axis. The long-lived absorptive signal (blue) is represented in an ad-hoc fashion by a fixed, two-dimensional Gaussian with an amplitude and width determined from SSPP images at long times. The full simulated image is formed from a linear addition of these two contributions. The simulated images (Figure 5.5D) show a strong resemblance to the SSPP images, reproducing both the time scale and asymmetry of the evolution. Because the separated charges are extracted by the electrodes, the positive-going amplitude depicted in the simulated images represents a quasi-neutral charge cloud consisting of *both* electrons and holes with nearly equal carrier densities. The similarity between the simulated images and the SSPP images suggests that much of the asymmetric evolution observed in the pump-probe images arises from a combination of two factors: (i) differences in the electron and hole mobilities, which causes the quasi-neutral charge cloud to drift towards the positive electrode, and (ii) faster electron-hole recombination in the *p*-type segment compared to the intrinsic and *n*-type regions.

Although the simulations are intended to mimic the *p-i-n* junctions, there is a notable difference between the model and the experimental measurements. The SSPP experiments are performed on isolated wires under open-circuit conditions whereas the simulations model the junction as a wire connected to an external circuit, which is needed to mimic the built-in electric field. A long-lived charge-separated state can be produced in the experiment but would not be expected in the simulations because separated charges are extracted by the electrodes.

Thus, the simulations recover many of the qualitative features of the SSPP images but do not reproduce the long-lived signals that are observed on the nanosecond time scale (e.g. 12.5 ns frame in Figure 5.3B) and attributed to charge separation.

This analysis leads to the description of carrier migration and separation illustrated in Figure 5.6. Photoexcitation produces a neutral electron-hole cloud consisting of free electrons and holes in the middle of the intrinsic segment (Figure 5.6i). Because of the high photogenerated carrier density, carrier-carrier interactions result in a significant energy penalty for charge separation, and as a consequence, the neutral distribution spreads across the intrinsic segment with little influence from the built-in electric field (Figure 5.6ii). As it spreads, electron-hole recombination reduces the carrier density by a factor 10-20. Once the charge cloud reaches the depletion region boundaries (200-400 ps), photogenerated carriers near the *n*-type region encounter the free electrons that have accumulated near the *i*-*n* boundary, resulting in enhanced recombination, with a similar process occurring at the *p*-*i* boundary. Recombination may also be assisted by the larger field[50,51] predicted to be at the boundary by the finite element simulations (Fig 5.6iii). Together, these processes further decrease the overall charge density, and the lower carrier density — combined with the larger field — facilitates charge separation. At 400-500 ps after photoexcitation, the edge of the charge cloud that is enriched with electrons (holes) passes into the *n*-type (*p*-type) region through a combination of both diffusion and field-induced drift (Figure 5.6iv). As the cloud enters the *p*-type region, rapid electron-hole surface recombination occurs, leaving behind the excess holes. The analogous process occurs in the *n*-type region but on a longer time scale. By 500-1000 ps only the excess electrons and holes remain, giving rise to the long-lived charge-separated state that is observed experimentally (Fig 5.6v).

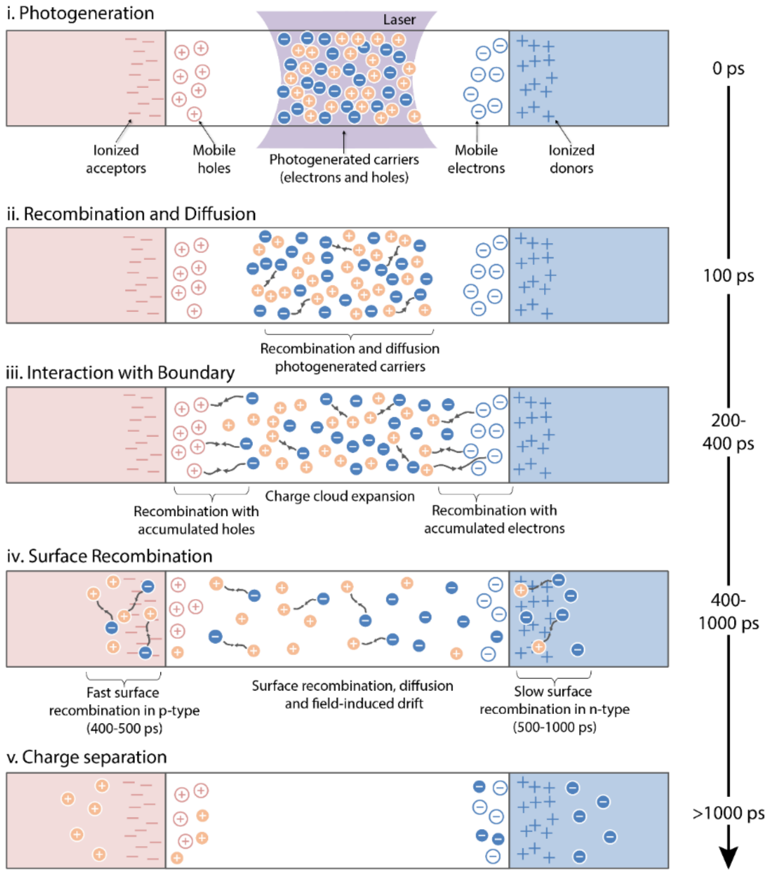

Figure 5.6: Mechanism for charge separation in a *p-i-n* NW junction under high photogenerated carrier densities. i. Carriers are generated at the center of the intrinsic region by an ultrafast laser pulse focused to a diffraction-limited spot. Photoexcited carriers are depicted as solid circles (blue for electrons and light orange for holes). Due to the high photoexcited charge carrier density, carrier-carrier interactions dominate, screening the influence of the electric field that results from the presence of fixed negative charges in the *p*-type region (pink) and fixed positive charges in the *n*-type region (blue), as well as mobile carriers that accumulate near the boundaries. **ii.** Carrier density is reduced by electron-hole recombination as the photogenerated carrier cloud spreads across the intrinsic region. **iii**. Further reduction in the photogenerated carrier density occurs as the photogenerated holes reach the *n*-type boundary and recombine with free electrons (open blue circles). On the opposite side, photogenerated electrons recombine with free holes (open light pink circles) from the *p*-type region. **iv.** Rapid surface recombination in *p*-type, with slower recombination in *n*-type regions. **v.** The reduced carrier density and large field at the boundary leads to the formation of a long-lived charge-separated state.

5.7 Conclusion

Visualization of charge carrier motion with ultrafast microscopy provides a window through which the physical factors that influence carriers as they navigate through individual nanostructures can be viewed. The combined spatial and temporal resolution of pump-probe microscopy makes it well-suited to capture the complexities of the charge carrier behavior. A detailed understanding of how charges move through individual nanostructures will only become increasingly important as materials with greater complexity are targeted for sophisticated nanoscale electronic and optoelectronic applications.

5.8 Acknowledgements

This project was supported by the National Science Foundation under grant numbers CHE-1213379 (M.M.G, E.M.G., E.E.M.C, D.F.Z. and J.M.P) and DMR-1308695 (C.W.P., J.D.C and J.F.C).

REFERENCES

1 Lieber, C. M. Semiconductor Nanowires: A Platform for Nanoscience And Nanotechnology. *MRS Bulletin* **36**, 1052-1063, (2011).

2 Yang, P. D., Yan, R. X. & Fardy, M. Semiconductor Nanowire: What's Next? *Nano Letters* **10**, 1529-1536, (2010).

3 Garnett, E. C., Brongersma, M. L., Cui, Y. & McGehee, M. D. Nanowire Solar Cells. *Annual Review of Materials Research* **41**, 269-295, (2011).

4 Peng, K. Q. & Lee, S. T. Silicon Nanowires for Photovoltaic Solar Energy Conversion. *Advanced Materials* **23**, 198-215, (2011).

5 Cui, Y. & Lieber, C. M. Functional Nanoscale Electronic Devices Assembled Using Silicon Nanowire Building Blocks. *Science* **291**, 851-853, (2001).

6 Cui, Y., Zhong, Z., Wang, D., Wang, W. U. & Lieber, C. M. High Performance Silicon Nanowire Field Effect Transistors. *Nano Letters* **3**, 149-152, (2003).

7 Lu, W. & Lieber, C. M. Semiconductor Nanowires. *Journal of Physics D: Applied Physics* **39**, R387-R406, (2006).

8 Goldberger, J., Hochbaum, A. I., Fan, R. & Yang, P. Silicon Vertically Integrated Nanowire Field Effect Transistors. *Nano Letters* **6**, 973-977, (2006).

9 Kempa, T. J., Tian, B. Z., Kim, D. R., Hu, J. S., Zheng, X. L. & Lieber, C. M. Single and Tandem Axial p-i-n Nanowire Photovoltaic Devices. *Nano Letters* **8**, 3456-3460, (2008).

10 Kempa, T. J., Day, R. W., Kim, S. K., Park, H. G. & Lieber, C. M. Semiconductor Nanowires: A Platform for Exploring Limits and Concepts for Nano-Enabled Solar Cells. *Energy & Environmental Science* **6**, 719-733, (2013).

11 Tian, B. Z., Zheng, X. L., Kempa, T. J., Fang, Y., Yu, N. F., Yu, G. H., Huang, J. L. & Lieber, C. M. Coaxial Silicon Nanowires as Solar Cells and Nanoelectronic Power Sources. *Nature* **449**, 885-890, (2007).

12 Kempa, T. J., Cahoon, J. F., Kim, S. K., Day, R. W., Bell, D. C., Park, H. G. & Lieber, C. M. Coaxial Multishell Nanowires with High-Quality Electronic Interfaces and Tunable Optical Cavities for Ultrathin Photovoltaics. *Proceedings of the National Academy of Sciences of the United States of America* **109**, 1407-1412, (2012).

13 Kim, S.-K., Day, R. W., Cahoon, J. F., Kempa, T. J., Song, K.-D., Park, H.-G. & Lieber, C. M. Tuning Light Absorption in Core/Shell Silicon Nanowire Photovoltaic Devices through Morphological Design. *Nano Letters* **12**, 4971-4976, (2012).

14 Kelzenberg, M. D., Turner-Evans, D. B., Putnam, M. C., Boettcher, S. W., Briggs, R. M., Baek, J. Y., Lewis, N. S. & Atwater, H. A. High-Performance Si Microwire Photovoltaics. *Energy & Environmental Science* **4**, 866-871, (2011).

15 Zhang, X., Pinion, C. W., Christesen, J. D., Flynn, C. J., Celano, T. A. & Cahoon, J. F. Horizontal Silicon Nanowires with Radial p–n Junctions: A Platform for Unconventional Solar Cells. *The Journal of Physical Chemistry Letters* **4**, 2002-2009, (2013).

16 Mohite, A. D., Perea, D. E., Singh, S., Dayeh, S. A., Campbell, I. H., Picraux, S. T. & Htoon, H. Highly Efficient Charge Separation and Collection Across in-situ Doped Axial VLS-Grown Si Nanowire p-n Junctions. *Nano Letters* **12**, 1965-1971, (2012).

17 Wallentin, J., Anttu, N., Asoli, D., Huffman, M., Aberg, I., Magnusson, M. H., Siefer, G., Fuss-Kailuweit, P., Dimroth, F., Witzigmann, B., Xu, H. Q., Samuelson, L., Deppert, K. & Borgstrom, M. T. InP Nanowire Array Solar Cells Achieving 13.8% Efficiency by Exceeding the Ray Optics Limit. *Science* **339**, 1057-1060, (2013).

18 Krogstrup, P., Jorgensen, H. I., Heiss, M., Demichel, O., Holm, J. V., Aagesen, M., Nygard, J. & Morral, A. F. I. Single-Nanowire Solar Cells Beyond the Shockley-Queisser Limit. *Nature Photonics* **7**, 306-310, (2013).

19 Colombo, C., Heiss, M., Gratzel, M. & Morral, A. F. I. Gallium Arsenide p-i-n Radial Structures for Photovoltaic Applications. *Applied Physics Letters* **94**, 173108, (2009).

20 Tang, J. Y., Huo, Z. Y., Brittman, S., Gao, H. W. & Yang, P. D. Solution-Processed Core-Shell Nanowires for Efficient Photovoltaic Cells. *Nature Nanotechnology* **6**, 568-572, (2011).

21 Fan, Z. Y., Razavi, H., Do, J. W., Moriwaki, A., Ergen, O., Chueh, Y. L., Leu, P. W., Ho, J. C., Takahashi, T., Reichertz, L. A., Neale, S., Yu, K., Wu, M., Ager, J. W. & Javey, A. Three-Dimensional Nanopillar-Array Photovoltaics on Low-Cost and Flexible Substrates. *Nature Materials* **8**, 648-653, (2009).

22 Mnatsakanov, T. T., Rostovtsev, I. L. & Philatov, N. I. Investigation of the effect of nonlinear physical phenomena on charge carrier transport in semiconductor devices. *Solid-State Electronics* **30**, 579-585, (1987).

23 Mnatsakanov, T. T., Shuman, V. B., Pomortseva, L. I., Schröder, D. & Schlögl, A. Effect of nonlinear physical phenomena on the photovoltaic effect in silicon p+–n–n+ solar cells. *Solid-State Electronics* **44**, 383-392, (2000).

24 Kerr, M. J. & Cuevas, A. General Parameterization of Auger Recombination in Crystalline Silicon. *Journal of Applied Physics* **91**, 2473, (2002).

25 Schmidt, V., Senz, S. & Gösele, U. Influence of the Si/SiO2 interface on the charge carrier density of Si nanowires. *Applied Physics A* **86**, 187-191, (2007).

26 Schmidt, V., Wittemann, J. V., Senz, S. & Gösele, U. Silicon Nanowires: A Review on Aspects of their Growth and their Electrical Properties. *Advanced Materials* **21**, 2681-2702, (2009).

27 Kar, A., Upadhya, P. C., Dayeh, S. A., Picraux, S. T., Taylor, A. J. & Prasankumar, R. P. Probing Ultrafast Carrier Dynamics in Silicon Nanowires. *Ieee Journal of Selected Topics in Quantum Electronics* **17**, 889-895, (2011).

28 Prasankumar, R. P., Upadhya, P. C. & Taylor, A. J. Ultrafast carrier dynamics in semiconductor nanowires. *physica status solidi (b)* **246**, 1973-1995, (2009).

29 Song, J. K., Willer, U., Szarko, J. M., Leone, S. R., Li, S. & Zhao, Y. Ultrafast Upconversion Probing of Lasing Dynamics in Single ZnO Nanowire Lasers. *Journal of Physical Chemistry C* **112**, 1679-1684, (2008).

30 Styers-Barnett, D. J., Ellison, S. P., Mehl, B. P., Westlake, B. C., House, R. L., Park, C., Wise, K. E. & Papanikolas, J. M. Exciton Dynamics and Biexciton Formation in Single-Walled Carbon Nanotubes Studied with Femtosecond Transient Absorption Spectroscopy. *Journal of Physical Chemistry C* **112**, 4507-4516, (2008).

31 Ahn, Y., Dunning, J. & Park, J. Scanning Photocurrent Imaging and Electronic Band Studies in Silicon Nanowire Field Effect Transistors. *Nano Letters* **5**, 1367-1370, (2005).

32 Howell, S. L., Padalkar, S., Yoon, K., Li, Q., Koleske, D. D., Wierer, J. J., Wang, G. T. & Lauhon, L. J. Spatial Mapping of Efficiency of GaN/InGaN Nanowire Array Solar Cells Using Scanning Photocurrent Microscopy. *Nano Letters* **13**, 5123-5128, (2013).

33 Gu, Y., Romankiewicz, J. P., David, J. K., Lensch, J. L., Lauhon, L. J., Kwak, E. S. & Odom, T. W. Local Photocurrent Mapping as a Probe of Contact Effects and Charge Carrier Transport in Semiconductor Nanowire Devices. *Journal of Vacuum Science & Technology B: Microelectronics and Nanometer Structures* **24**, 2172, (2006).

34 Allen, J. E., Hemesath, E. R. & Lauhon, L. J. Scanning Photocurrent Microscopy Analysis of Si Nanowire Field-Effect Transistors Fabricated by Surface Etching of the Channel. *Nano Letters* **9**, 1903-1908, (2009).

35 Gutsche, C., Niepelt, R., Gnauck, M., Lysov, A., Prost, W., Ronning, C. & Tegude, F. J. Direct Determination of Minority Carrier Diffusion Lengths at Axial GaAs Nanowire p-n Junctions. *Nano Letters* **12**, 1453-1458, (2012).

36 Mehl, B. P., Kirschbrown, J. R., Gabriel, M. M., House, R. L. & Papanikolas, J. M. Pump-Probe Microscopy: Spatially Resolved Carrier Dynamics in ZnO Rods and the Influence of Optical Cavity Resonator Modes. *Journal of Physical Chemistry B* **117**, 4390-4398, (2013).

37 Mehl, B. P., Kirschbrown, J. R., House, R. L. & Papanikolas, J. M. The End Is Different than The Middle: Spatially Dependent Dynamics in ZnO Rods Observed by Femtosecond Pump–Probe Microscopy. *The Journal of Physical Chemistry Letters* **2**, 1777-1781, (2011).

38 Gabriel, M. M., Kirschbrown, J. R., Christesen, J. D., Pinion, C. W., Zigler, D. F., Grumstrup, E. M., Mehl, B. P., Cating, E. E. M., Cahoon, J. F. & Papanikolas, J. M. Direct Imaging of Free Carrier and Trap Carrier Motion in Silicon Nanowires by Spatially-Separated Femtosecond Pump-Probe Microscopy. *Nano Letters* **13**, 1336-1340, (2013).

39 Grumstrup, E. M., Gabriel, M. M., Cating, E. M., Pinion, C. W., Christesen, J. D., Kirschbrown, J. R., Vallorz, E. L., Cahoon, J. F. & Papanikolas, J. M. Ultrafast Carrier Dynamics in Individual Silicon Nanowires: Characterization of Diameter-Dependent Carrier Lifetime and Surface Recombination with Pump-Probe Microscopy. *The Journal of Physical Chemistry C*, DOI: 10.1021/jp502737e, (2014).

40 Berweger, S., Atkin, J. M., Olmon, R. L. & Raschke, M. B. Light on the Tip of a Needle: Plasmonic Nanofocusing for Spectroscopy on the Nanoscale. *Journal of Physical Chemistry Letters* **3**, 945-952, (2012).

41 Schumacher, T., Giessen, H. & Lippitz, M. Ultrafast Spectroscopy of Quantum Confined States in a Single CdSe Nanowire. *Nano Letters* **13**, 1706-1710, (2013).

42 Gao, B., Hartland, G. V. & Huang, L. B. Transient Absorption Spectroscopy and Imaging of Individual Chirality-Assigned Single-Walled Carbon Nanotubes. *ACS Nano* **6**, 5083-5090, (2012).

43 Carey, C. R., Yu, Y., Kuno, M. & Hartland, G. V. Ultrafast Transient Absorption Measurements of Charge Carrier Dynamics in Single II−VI Nanowires. *The Journal of Physical Chemistry C* **113**, 19077-19081, (2009).

44 Seo, M. A., Yoo, J., Dayeh, S. A., Picraux, S. T., Taylor, A. J. & Prasankumar, R. P. Mapping carrier diffusion in single silicon core-shell nanowires with ultrafast optical microscopy. *Nano Letters* **12**, 6334-6338, (2012).

45 Christesen, J. D., Zhang, X., Pinion, C. W., Celano, T. A., Flynn, C. J. & Cahoon, J. F. Design Principles for Photovoltaic Devices Based on Si Nanowires With Axial or Radial p-n Junctions. *Nano Letters* **12**, 6024-6029, (2012).

46 Shah, A. *Thin-Film Silicon Solar Cells*. (EFPL Press, 2010).

47 Grumstrup, E. M., Cating, E. M., Gabriel, M. M., Pinion, C. W., Christesen, J. D., Kirschbrown, J. R., Vallorz, E. L., Cahoon, J. F. & Papanikolas, J. M. Ultrafast Carrier Dynamics of Silicon Nanowire Ensembles: The Impact of Geometrical Heterogeneity on Charge Carrier Lifetime. *The Journal of Physical Chemistry C*, DOI: 10.1021/jp501079b, (2014).

48 Aberle, A. G. Surface Passivation of Crystalline Silicon Solar Cells: A Review. *Progress in Photovoltaics: Research and Applications* **8**, 473-487, (2000).

49 Also apparent at the tip of the wire is a transient response from the catalyst, which shows an initial bleach that quickly decays, becoming a long-lived absorption.

50 Schenk, A. A model for the field and temperature dependence of Shockley-Read-Hall lifetimes in silicon. *Solid-State Electronics* **35**, 1585-1596, (1992).

51 Hurkx, G. A. M., Klaassen, D. B. M. & Knuvers, M. P. G. A new recombination model for device simulation including tunneling. *Electron Devices, IEEE Transactions on* **39**, 331-338, (1992).

CHAPTER 6: IMAGING ACOUSTIC PHONON MODES IN VANADIUM DIOXIDE

6.1 Introduction

6.1.1 Vanadium Dioxide Background

One-dimensional nanostructures, which often exhibit novel physical characteristics that differ from those of their bulk counterparts, represent an attractive class of materials for the rational development of nanoscale electronics. Vanadium dioxide (VO_2), represents a prototypical strongly correlated electron compound and has been the subject of extensive experimental investigation, in large part, due to its insulator-to-metal transition (IMT) near ambient temperature which involves a structural transformation from a low temperature monoclinic insulating (or semiconducting) phase to a high-temperature rutile metallic phase at 340K. The easily accessible phase transition makes VO_2 a prime candidate for fundamental studies of phase transition materials. Additionally, the transition features drastic changes in the electronic and optical properties of the material, making vanadium dioxide nanomaterials with wire-like connectivity ideal candidates for a variety of novel nanoscale electronic applications, such as field effect transistors (FETs), optical switches, photonics, and sensors.

The exact mechanism of the phase transition is still the subject of considerable debate, mostly revolving around the nature of the nature of the insulating state and the delicate balance of cooperative interactions involved in the structural transition. Competing theories have attributed the effect to either a Peiels instability[1-4] or a Mott transtion[5-8], with the central question being whether or not the transition is predominantly driven by electron-electron interactions, electron-lattice contributions, or a combination of the two.[9-17]

6.1.2 Advantages of Pump-probe Microscopy

Ultrafast pump-probe techniques involving the use of ultrafast laser pulses to drive the phase transition have been used to monitor electronic and structural changes down to femtosecond timescales. Time-resolved photo-electron spectroscopy (TR-PES) has been used to directly probe ultrafast changes in the electronic structure during the phase transition,[10,18,19] while structural lattice changes have been followed using time-resolved electron[20-23] and x-ray diffraction[24,25] methods. Similarly, ultrafast optical spectroscopies have been used to probe photoinduced changes in the optical properties of VO_2 which can be correlated with electronic and structural changes.[6,26-33] Though these studies have significantly advanced the understanding of the dynamical electronic and structural complexities associated with the IMT in vanadium dioxide, many of them have centered on polycrystalline films or averaged over ensembles of single crystals. Heterogeneity within the samples, such as variations in grain size, morphology, orientation, and defect concentration can drastically alter the measured experimental response.[23,33-35] Additionally lattice strain can change the relative stability of various phases that coexist in VO_2 over a range of temperatures, further complicating the interpretation of experimental data that average over an ensemble crystallites.[36-42] In this regard, ultrafast spatially-resolved techniques capable of probing individual structures, and even localized regions along a single structure, are preferred.

6.2 Imaging VO_2 Phase Transition

6.2.1 Description of Experiment

Our strategy involves the combination of transient absorption (TA) pump-probe spectroscopy with optical microscopy.[43-49] With diffraction-limited spatial resolution (~700 nm) and ultrafast temporal resolution (~500 fs), this technique enables the investigation of dynamical phenomena from individual structures within an ensemble, as well as at different points within a single structure. Recent studies from our group focused on photoexcited charge carrier dynamics silicon nanowires (NWs).[45-49] In these pump-probe experiments, charge carriers (electrons and holes) are excited in localized regions on individual NWs by a femtosecond pump pulse that has been focused to a diffraction-limited spot by a microscope objective. After a well-defined delay, the excited carrier population is probed by a second femtosecond laser pulse that is either spatially-overlapped with the pump pulse or spatially-separated from the pump. The pump-induced changes to the transmission of the probe are measured. In the spatially-overlapped pump-probe (SOPP) configuration, the decay of the signal reflects both electron-hole recombination. Additionally, because the pump and probe spot sizes are small relative to the axis of the wire, motion of carriers out of the probe volume also contributes to signal decay. This motion is directly observed using the spatially-separated pump-probe (SSPP) configuration, where carriers are created in one location and detected in another. The ability to vary the position of the probe beam relative to the pump enables the correlation of transport properties as well as electron-hole recombination with specific structural features such as diameter, orientation, composition, and conformation.

In this work, we apply the same spatially-separated pump-probe microscopy technique, previously described in more detail elsewhere,[45] to examine the photoinduced dynamical properties of VO_2. In this case, at high enough pump fluences, the pump pulse drives the IMT, altering the optical properties of the sample, which are monitored by the probe pulse in the transient absorption configuration.

6.2.2 Description of Samples

The VO_2 samples in this work were obtained through collaboration with the Haglund group and Vanderbilt. The micro/nanowires (MNWs) were grown using a thermal transport method which was first developed by Guiton and coworkers.[50] For this work, VO_2 MNWs were grown using a deposition process that is somewhat modified from that reported by Cheng *et al*.[51] The VO_2 samples were grown on a Si substrate using V_2O_5 powder obtained from Sigma Aldrich Co. The growth process was carried out in a two-inch horizontal tube furnace filled with Ar gas flowing at 28 sccm and 1.7 mTorr. The furnace temperature was ramped up from room temperature at $\sim 10°C\ min^{-1}$, held at 825°C for one hour and then allowed to cool. Though the MNWs ranged in size and morphology, the individual wires studied in this work ranged in diameter from ~200 nm to ~350 nm and most likely have rectangular or hexagonal cross-sections. Representative SEM images of the wires are shown in Figure 6.1A and 6.2B.

6.2.3 Power Dependent Transients

To demonstrate the ultrafast transient response of the material, the pump and probe beams were spatially-overlapped and collinearly focused to diffraction-limited spots by an ultralong working distance microscope objective (100 X, 0.8 NA). The 425 nm pump pulse, which is frequency doubled from the 850 nm output of an ultrafast Ti:Sapphire laser, excites the VO_2 well above the 0.67 eV band gap.[52] The 850 nm probe beam is passed through a mechanical stage to control the time delay between the pump and the probe pules. Both pump and probe beams are passed through a pair of synchronized AOMs to reduce the repetition rate from 80 MHz to 1.67 MHz to ensure that the insulating state is completely recovered before the next pump-probe pulse pair arrives. Additionally, longer pump-probe delays at 12.5 ns intervals can be achieved by adjusting the pump AOM to selectively pick earlier pulses. The change in transmitted probe intensity (ΔI) is monitored using a balanced photodiode and lock-in detection. While the pump pulse energies vary in the following experiments, the probe energy is fixed at approximately 10 pJ/pulse. Figure 6.1A shows an SEM image of a VO_2 nanowire (NW1) with a corresponding pump-probe image of the same wire pumped at 28 pJ/pulse. The SOPP image is obtained by holding the pump-probe delay fixed at zero ps while scanning pump-probe pulse pair over the wire. The positive-going signal at time zero indicates a photoinduced increase in probe transmission across the wire. Note that the magnitude of the pump-probe signal is not consistent along the wire axis even though the wire appears uniform in the corresponding SEM image. This concept demonstrates that the pump-probe microscope is sensitive to heterogeneities not readily apparent in SEM imaging. To eliminate possible disparities caused by defects or other impurities, the subsequent analysis of the phase transition in NW1 is performed in a spatial region exhibiting homogeneous in behavior in both (SEM and pump-probe) images. To investigate the onset and behavior of the phase transition in VO_2 NWs, transient data were collected at ambient temperature at a single localized point along the axis of NW1, as indicated in Figure 6.1A by the blue circle on the 0 ps pump-probe image. Figure 6.1B shows the transient curves collected at increasing pump fluences with light blue colored traces corresponding to the lowest fluences and increasing color saturation corresponding with increasing fluence.

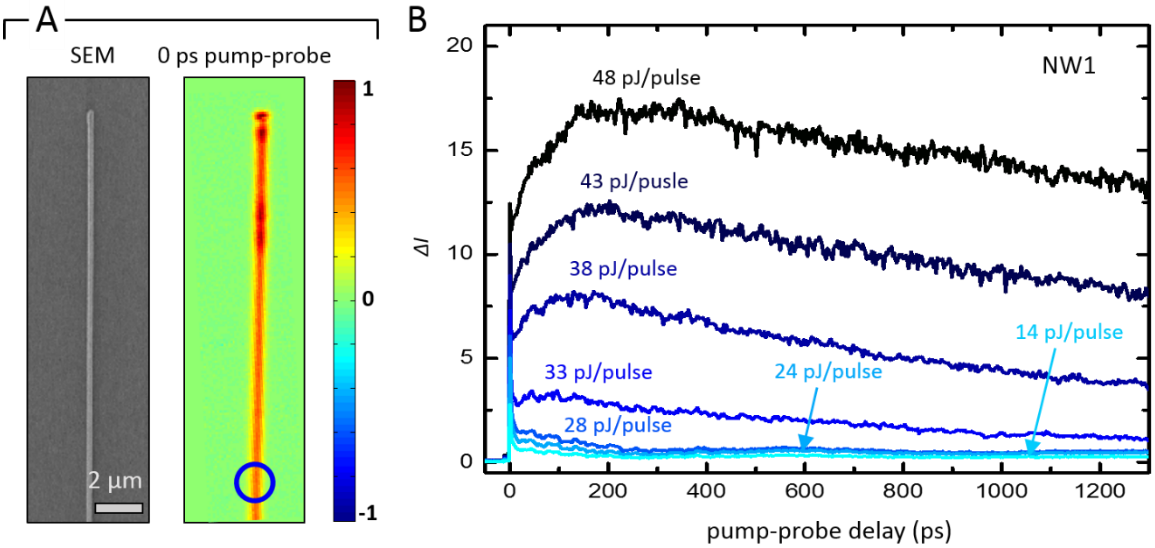

Figure 6.1: Pump-probe microscopy of VO_2 phase transition. (A) SEM of VO_2 NW (NW1) and corresponding pump-probe image, collected by scanning the sample stage over the focal point of the spatially overlapped pump (425 nm, 28 pJ/pulse) and probe (850 nm, 10 pJ/pulse) pulses with a fixed pump-probe delay of 0 ps. The pump-probe image is depicted using a normalized color scale with red representing positive-going signal. The same spatial scale is used for both images with a scale bar of 2 µm. NW1 is approximately 230 nm in diameter. **(B)** Power-dependent transient kinetics on a single position of NW1 following localized photoexcitation (λ = 420 nm) at the point indicated by the blue circle on the zero ps delay pump-probe image. Seven transient scans are shown for pump fluences of 14 pJ/pulse, 24 pJ/pulse, 28 pJ/pulse, 33 pJ/ pulse, 38 pJ/pulse, 43 pJ/pulse and 48 pJ/pulse, with light colored traces corresponding to the lowest fluences and increasing in color saturation with increasing fluence.

In general, transient absorption signals are affected by pump-induced changes in optical properties of the sample such as absorption, reflection, and scattering. In the case of VO_2, the observed pump-probe response is sensitive to both, pump-induced changes in excited-carrier concentration as well as structural changes associated with the IMT. The power dependent studies here show a threshold-like behavior similar to previous reports.[30,31,52] At the lowest excitation fluences (14-28 pJ/pulse in Figure 6.1B) a quasi-instantaneous (faster than the temporal resolution of the microscope) change in transmission of the probe is observed, indicative of the presence of excited electrons and holes. Their subsequent relaxation results in a fast decay of the signal over the first few picoseconds. At longer times, a small positive-going signal remains, likely the result of a thermal change in reflectivity due to heating of the lattice.[48,53] This signal is modulated by oscillations which will be discussed in further detail below. As the pump fluence is increased, the transient signature evolves, with a second ultrafast component emerging while the oscillations disappear. The disappearance of the oscillations and onset of a nonlinear increase in signal at energies above 28 pJ/pulse could be indicative of the structural transformation. However, determining exactly when the metallic state forms is challenging because the signal could arise from a combination of many processes such as changes in the band structure, volume expansion, lattice heating, and thermal diffusion, which can all occur simultaneously with the phase transition. For example, many sources have suggested that the structural transformation occurs within 1 ps at high pump powers;[13,24,29] however, time-resolved x-ray[24,25] and electron diffraction[20,22] studies have shown that the lattice evolves to the rutile phase on the order of 10's of picoseconds. This discrepancy could be due to an instantaneous photoinduced collapse of the band gap that leads to a transient monoclinic metallic state that exhibits similar electronic and optical properties to that of the rutile metallic state.[10,18,19] In our case, the second component that reaches a maximum at about 100 ps and persists over hundreds of nanoseconds is consistent with monoclinic to rutile phase transition in the first few hundred ps and a much longer-lived quasi-stable metal-like state,[54] the exact structure of which is unclear.

6.2.4 Spatially-Separated Pump-Probe Imaging

We have investigated the nature of the long-lived transient component by imaging the spatial evolution of the phase transition using the SSPP imaging mode. The pump fluence (60 pJ/pulse) is significantly above the threshold to drive the IMT in a VO_2 nanowire (NW2). The probe spot is laterally positioned relative to the pump spot by adjusting the angle of incidence at the back aperture of the microscope objective using a pair of computer controlled scanning mirrors. The position of the probe is scanned over the wire while the pump pulse is held fixed at the position indicated by the red circle on the SEM image in Figure 6.2. A series of SSPP images is collected at variable pump-probe delays. On relatively short timescales (not shown) over the length of the delay stage, negligible spreading of the signal is observed. However, images collected on longer timescales, accessed by adjusting the AOM pulse picker, show progressive broadening of the pump-probe signal.

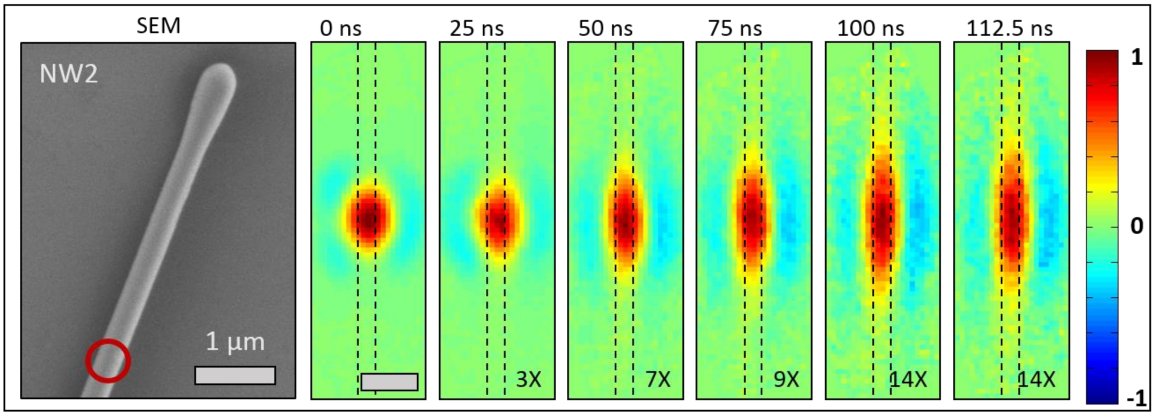

Figure 6.2: Spatially-separated imaging. Spatially-separated transient absorption images collected at various pump-probe delays (0 ps, 25 ns, 50 ns, 75 ns, 100 ns, and 112.5 ns) for VO_2 NW2 with the corresponding SEM image shown to the left of the pump-probe images. The red circle indicates the stationary position of the pump pulse. Scale bars are 1 µm. NW2 is approximately 330 nm in diameter. Dotted lines on the pump-probe image represent the approximate location of the NW. Each pump-probe image is depicted using a normalized color scale with the relative amplitudes indicated by the scaling factors at the bottom right of each image.

The growth of the signal is characterized in a manner similar to previous analyses of photogenerated carrier diffusion in SiNWs.[46,48,49] Growth profiles are obtained by integrating the images along the direction normal to the NW axis. The normalized profiles are then fit to a Gaussian function to extract the full-width at half-maximum ($\beta(\Delta t)$) which is related the diffusion constant (D) by the expression:

$$\beta(\Delta t) = \sqrt{\gamma_{pu}^2 + \gamma_{pr}^2 + 16\ln(2)\,Dt} \qquad \text{Eq. 6.1}$$

where γ_{pu} and γ_{pr} are the full-width at half-maximums (FWHMs) of the pump and probe spots. A plot of pump-probe delay (Δt) vs $\beta(\Delta t)^2/(16*\ln 2)$ should yield a linear trend where the slope is equal to the diffusion constant. Figure 6.3A shows the diffusion profiles extracted from the SSPP images for NW2 shown in Figure 6.2B. Similar data is shown for a single point on NW1 in Figure 6.4C and 6.4D. The profiles for NW1 were extracted from SSPP images (not shown) collected using the highest pump energy in Figure 6.1B (48 pJ/pulse), well above the transition threshold. The FWHM plots in Figure 6.3B and 6.3D both show a relatively linear trend at earlier times, but deviate from linearity at longer times. The diffusion constant is estimated using an instrumental weighted linear fit (solid blue lines in Figure 6.4B and 6.4D). The weight, w, for each data point is calculated using the expression:

$$w_i = \frac{1}{\sigma_i^2} \qquad \text{Eq. 6.2}$$

where σ is the size of the error bars for each point (red bars in Figure 6.4B and 6.4D). Using these fits we find estimate diffusion constants D_{NW2} = 0.0175 cm^2/s and D_{NW1} = 0.0218 cm^2/s. Both values are consistent with thermal diffusion in VO_2 (0.02 cm^2/s).[22]

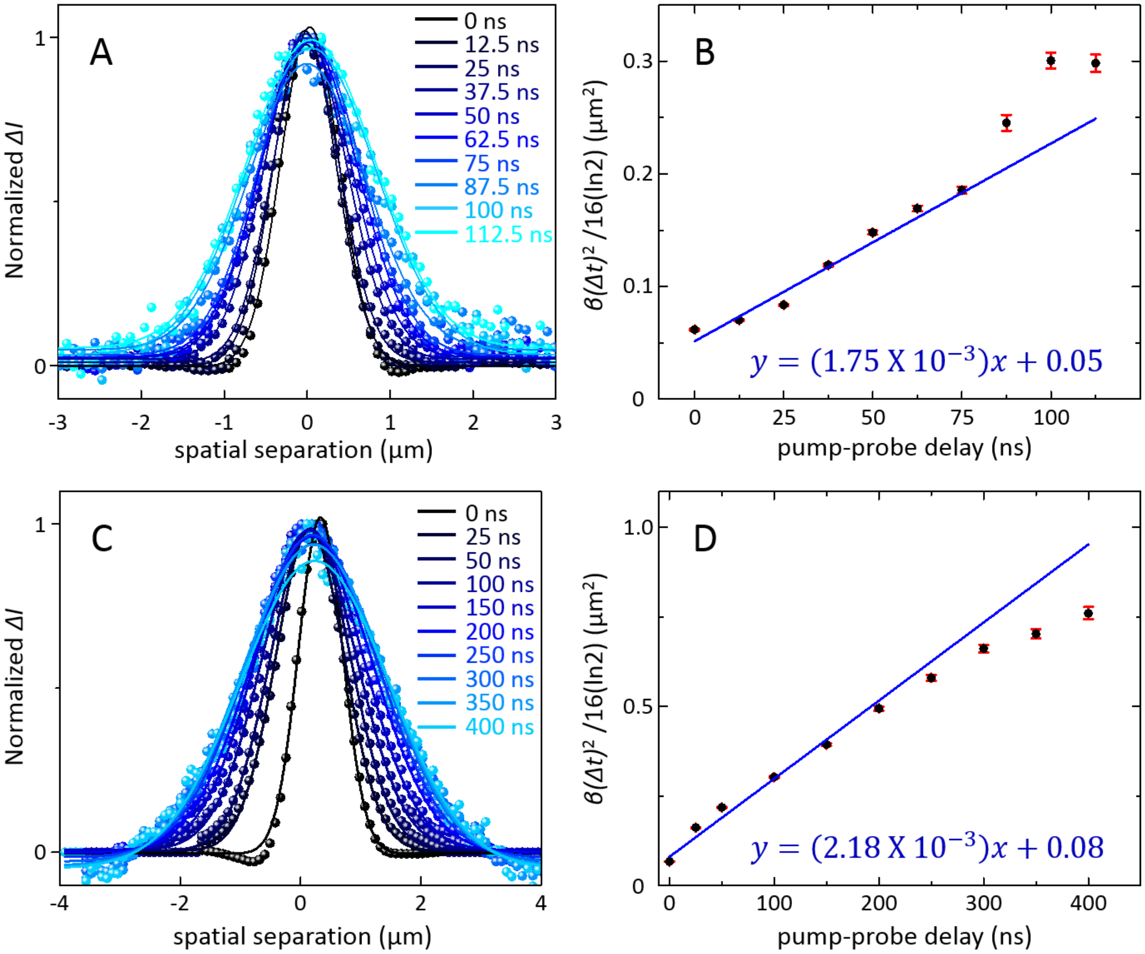

Figure 6.3: Spatial evolution of VO_2 transient signal. (A) Normalized diffusion profiles for VO_2 NW (NW2) following localized photoexcitation at the point indicated in Figure 6.1D. Diffusion profiles were obtained by integrating SSPP images collected at pump-probe delays of 0 ns, 12.5 ns, 25 ns, 37.5 ns, 50 ns, 62.5 ns, 75, ns, 87.5 ns, 100 ns, and 112.5 ns. **(B)** A plot pump-probe delay (Δt) vs $\beta(\Delta t)^2/(16*\ln 2)$. The diffusion constant is estimated using the slope of the weighted instrumental linear fit (solid blue line). The fit yields a slope of $1.75 \text{ X } 10^{-3}$ μm^2/ns. **(C)** Normalized diffusion profiles of signal for VO_2 NW1 following localized photoexcitation at an individual point (not shown). Diffusion profiles were obtained by integrating SSPP images collected at pump-probe delays of 0 ns, 25 ns, 50 ns, 100 ns, 150 ns, 200 ns, 250 ns, 300 ns, 350 ns, and 400 ns. **(D)** A plot pump-probe delay (Δt) vs $\beta(\Delta t)^2/(16*\ln 2)$. The diffusion constant is estimated using the slope of the weighted instrumental linear fit (solid blue line). The fit yields a slope of $2.18 \text{ X } 10^{-3}$ μm^2/ns.

Since the change in pump-probe signal is influenced by heating of the lattice as well as the structural transition, it is difficult to say whether or not the IMT is spreading along the wire axis or if the signal is a result of thermal diffusion alone. However, we would expect the diffusion of the IMT to spread on the same timescale as thermal diffusion, since the photoexcited carriers (which drive the initial transition) recombine after only a few picoseconds. In this case, the spreading that occurs over 100's of nanoseconds is most likely the result of lattice heating above (or near) the 340 K threshold due to thermal expansion.

Further quantitative analysis is needed in order to aid in distinguishing between the two processes. For example, knowledge of the exact temperature rise induced by pump pulses and the temperature gradient along the wire axis over time would determine the spatial extent over which the transition temperature is reached. Simple qualitative examination of the expansion profile itself supports some degree of IMT expansion. Of particular interest is the leveling off (and even slight reduction at the last data point for NW2) in the Gaussian FWHM at long delays. If the signal was a result of thermal diffusion alone, one would expect growth profiles that simply decay in magnitude while linearly spreading, much like that observed in the ambipolar diffusion of photoexcited electrons and holes in SiNWs.[46] While we do not consider signal magnitude here, the leveling off of the FWHM could be explained by lattice cooling and the percolative nature of the IMT. At long times, the wings of the Gaussian no longer reach a temperature high enough for the IMT. Though heat still expands, the structural change does not, leading to a smaller FWHM than predicted. As the lattice cools further, conversion of the metallic state back to the insulating (or semiconducting) state likely follows the temperature gradient in a reverse manner, receding from the wings of the Gaussian back towards the center.

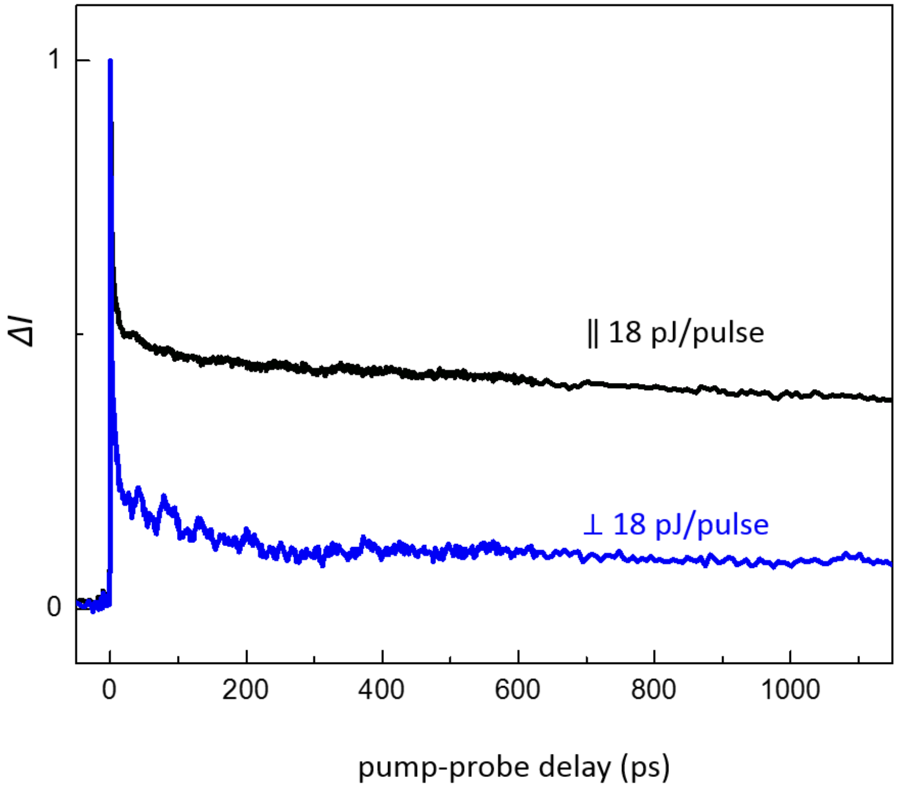

Figure 6.4: Polarization Dependence. Normalized transient absorption traces for a single point on VO_2 NW1 collected with pump and probe pulses parallel to the NW axis (black trace) and with pump and probe pulses perpendicular to the NW axis (blue).

6.3 Probing Coherent Acoustic Behavior in VO_2 NWs

In order to understand the nature of the coherent signals observed at low pump powers, several pump-probe experiments were performed on individual points along several different wires at pump fluences just below the transition threshold. In general the frequencies of acoustic modes in nanomaterials have been shown to be strongly coupled to geometry, orientation, and strain.[55-60] With diffraction-limited spatial resolution, we have investigated the behavior of coherent acoustic phonon modes in VO_2 NWs on a wire-to-wire and point-to-point basis to eliminate heterogeneity effects in the measured transient response.

6.3.1 Polarization Dependence

Initial experiments focused on the polarization dependence of transient signals. Figure 6.4 shows representative transient decay curves for pump and probe polarizations parallel to the NW axis (black curve) and pump and probe polarizations perpendicular to the NW axis (blue curve). Like the results for the low fluence regime in Figure 6.1B (which were performed in the perpendicular configuration) the decay traces exhibit an initial quasi-instantaneous change in transmission of the probe that occurs on a timescale faster than the temporal resolution of our microscope. The decay of this first ultrafast component that transpires over a few picoseconds is attributed the relaxation of the initially excited electron and hole populations. In the perpendicular configuration, the long-lived signal is oscillatory in time, likely due to the impulsive excitation of coherent acoustic phonons. In contrast, recurrences in the signal are not present in the parallel configuration, while the magnitude of the positive going signal attributed to a thermal component is much greater. Considering the mechanisms of acoustic phonon generation, these observations can be explained by the preferential conversion of optical energy into thermal energy in the parallel configuration and mechanical energy in the perpendicular case.

6.3.2 Mechanisms of Phonon Generation

Coherent vibrations can be generated in nanoscale metallic and semiconducting materials using ultrafast laser pump pulses. Numerous reports of phonon emission in both the semiconducting and metallic phase of VO_2 appear in the literature; however detailed accounts of phonon emission thus far correspond to Raman active vibrational modes in the THz frequency regime.[28-31,35-37,54] These are optical phonons which are caused by the motion of vanadium and oxygen atoms and cause oscillations with periods of about 100 – 200 fs. Since the temporal resolution of our microscope is ~ 500 fs, these modes cannot be resolved. Instead, we observe signal recurrences over much longer periods comparable to the excitation of acoustic phonons. Similar observations have been reported in a variety of nanoparticle and thin film systems[55-72] and several different mechanisms have been described.[55,56,70-72]

Two of the most commonly described are thermoelastic generation and deformation potential coupling. In the case of semiconductors (and the insulating phase of VO_2), ultrafast excitation promotes electrons (holes) into the conduction (valence) band of the material. Upon relaxation, the carriers rapidly transfer their excess energy into the lattice through the emission of phonons. Emission of incoherent phonons produces rapid heating of the lattice. The increase in temperature produces a thermoelastic stress which results in the generation of acoustic oscillations. The deformation potential mechanism involves a non-thermal process whereby excited electrons undergo spatial redistribution which causes a change in the internal electric field of the lattice. This causes a physical displacement of cations in the material leading to compressive or tensile stress which launches an acoustic wave through the lattice. In both cases, optical energy absorbed from the pump pulse ultimately undergoes conversion into mechanical energy (i.e. vibrations within the lattice). As the lattice vibrates, it modulates the optical properties of the wire.

The results of our experiments suggest that the acoustic phonon generation in VO_2 is not exclusively thermoelastic, since a thermoelastic stress induced by rapid heating of the lattice wouldn’t result in a polarization dependence. The anisotropic oscillatory response, is more indicative of a displacive excitation mechanism whereby the relaxation occurs with the emission of coherent acoustic phonons and pump energy is directly converted into mechanical energy. Interestingly, this response is comparable to optical phonon mode observations in transient reflectivity studies where optical modes are more prominent for pump polarizations perpendicular to the crystallographic *c*-axis.[54] This could indicate that the acoustic phonon generation mechanism is somehow coupled to the generation of optical phonons, whose relaxation is orientation dependent. At any rate, in the case of pump-probe pulses that are polarized parallel to the wire axis, the relaxation of electrons and holes likely occurs with emission of incoherent phonons. The increase in lattice temperature is evidenced by the long-lived background in the transient signal. The absence of signal recurrences in this configuration indicates that a thermoelastic stress is either not produced upon lattice heating or not detected by the optical probe pulse.

In following experiments, the perpendicular pump-probe microscopy configuration is used to investigate spatial dependence along different wires as well as the diameter dependence from wire to wire. The oscillatory signal is complex involving a combination of several different acoustic modes. These modes can be categorized by their period of oscillation and, for the following discussion, are separated into two acoustic frequency regimes, higher frequency modes between 10 and 70 GHz (100 ps and ~15 ps periods respectively) and lower frequency modes below 10 GHz.

6.4 Higher Frequency Modes

6.4.1 Spatial Dependence

In order to investigate the spatial dependence of acoustic phonon behavior in VO_2 NWs, transients were collected at different points along the interior of a wire as well as at the ends of the wire. To quantitatively analyze the response, the transients were fit to multi-exponential decays. The residuals of the multi-exponential fits represent the acoustic response. The complex assortment of resonant frequencies within the wires was extracted using Fourier transform (FT) analysis (Figures 6.5 and 6.6).

Along the points within the interior of the wire, the oscillatory response showed very little variance, likely due to the uniform homogeneous growth of the NWs. The only significant difference in the oscillatory pattern of the signal is seen at the ends of the nanowires. Figure 6.5 summarizes the spatially-dependent results for the ends and interior points of NW1 and NW3. The exact locations of data collection are indicated in Figure 6.5A with color-coded circles. The corresponding color-coded transients, residuals, and FT spectra are shown in Figures 6.5B, 6.5C and 6.5D respectively. The transients are normalized and arbitrarily offset for clarity. The residuals are also arbitrarily offset for clarity. The residuals and FT spectra and are depicted with arbitrary units for comparison.

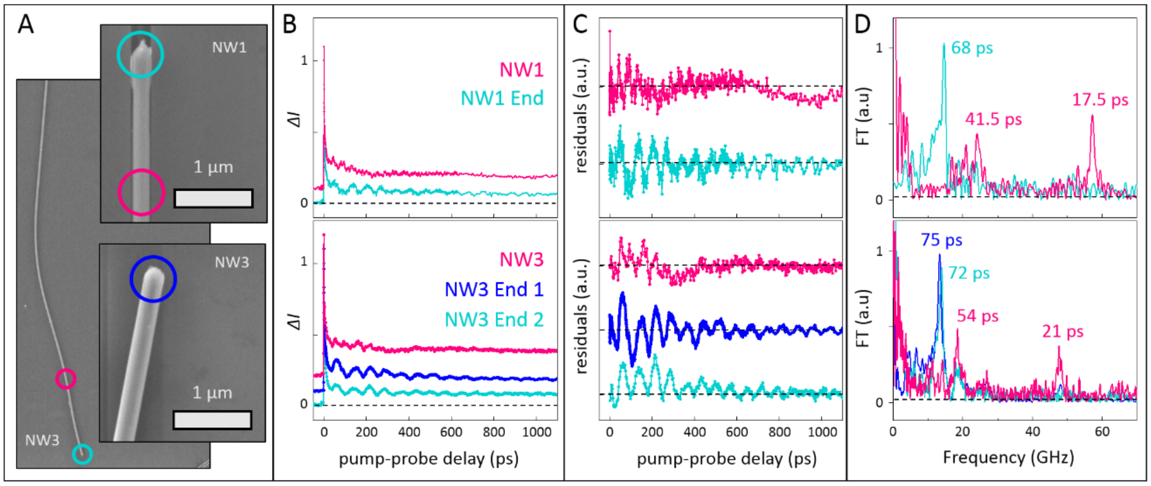

Figure 6.5: Spatial dependence of acoustic phonon modes. (A) SEM images of VO_2 NW1 and NW3. The zoomed-in inset images of the ends are magnified 10X compared to the larger image of NW3. Scale Bars are 1 µm. NW1 is approximately 230 nm in diameter and NW3 is approximately 260 nm in diameter. **(B)** Offset normalized transients collected at the ends (cyan and blue curves) vs interior points (pink curves) for the two VO_2 wires (NW1 and NW3). Color-coded circles on the SEM images correspond to collection points on each wire. **(C)** Residuals for transients in 6.5B after multi-exponential decay fits for each trace. **(D)** Fourier transform spectra of corresponding residuals.

Though the FT spectra are very complex, some clear observations can be made. It is worth mentioning that a complicated spectrum of peaks exists below 10 GHz, some of which can be attributed to the limited temporal window of the transient decay scan. However, lower frequency recurrences are apparent in a few of the transients and corresponding residuals, particularly for data collected at points within the interior of the wire (pink traces). These signals will be discussed further in section 6.5 below; meanwhile, the current discussion will be limited to modes that can be clearly resolved in our experiment within a time window of 1 ns (between 10 and 70 GHz). In this range, FT spectra for the various positions on NW1 and NW3 exhibit complimentary features. At points along the interior of the two wires (indicated in pink), two dominant frequency modes are apparent. On the interior point in NW3, one peak appears around 20 GHz corresponding to a period of 54 ps; whereas in NW1 a cluster of peaks appears in this region, with the largest peak corresponding to a period of 41.5 ps. Additionally both interior positions also accommodate similar higher frequency modes where NW3 exhibits a mode with a period of 21 ps and for NW1, 17.5 ps. At the ends of both wires (represented in cyan and royal blue), only one peak is apparent at slightly lower frequencies corresponding to a mode period of around 70 ps. In NW3 the transient data collected at both ends of the wire and corresponding analysis are remarkably similar considering the NW length, which is well over 60 μm. This supports the idea that geometry aspects such as size and shape play a significant role in the acoustic phonon response of nanomaterials.

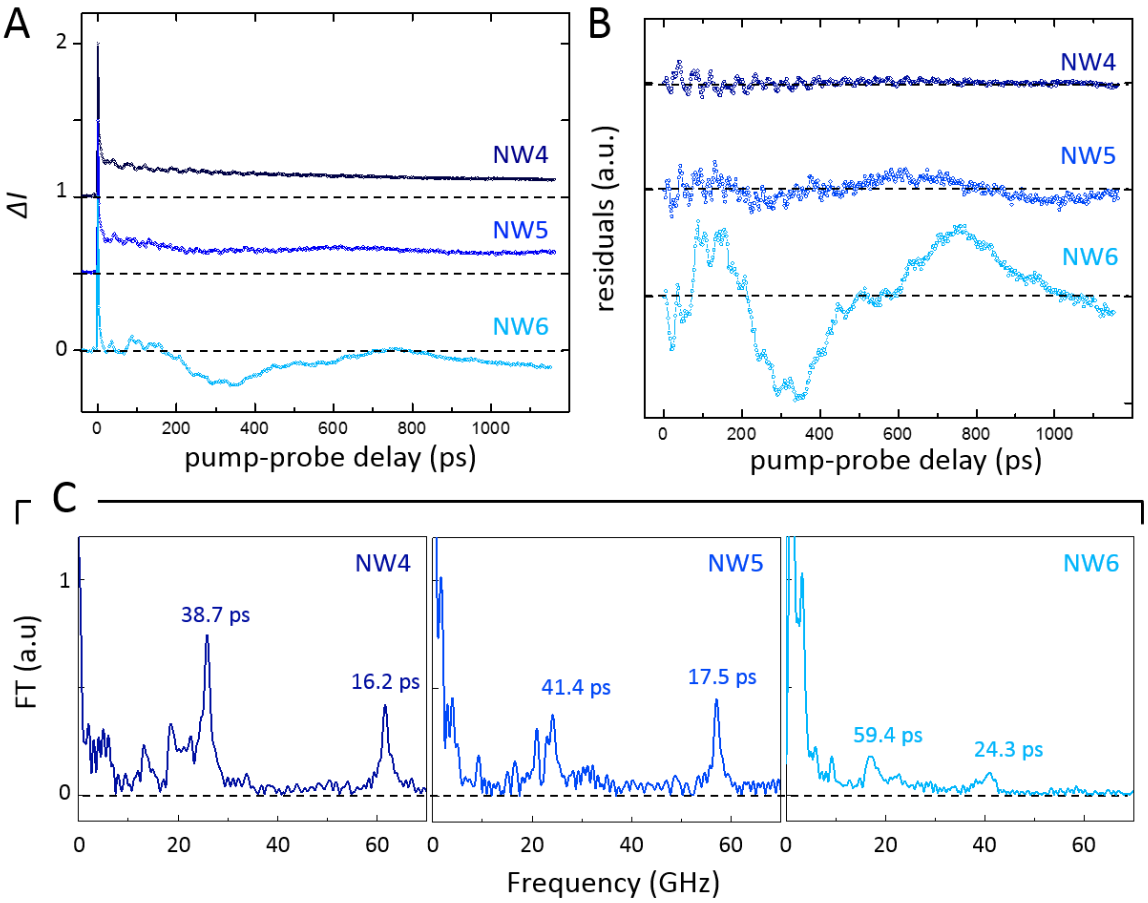

Figure 6.6: (A) Offset normalized transient signals for three VO_2 wires, NW4 (d = 220 nm), NW5 (d = 230 nm), and NW6 (d = 340 nm). Data for NW6 was collected at a single localized point whereas data for NW4 and NW6 represent an average of several homogeneous points along the interior of each wire. **(B)** Residuals for transients in 6.4A after multi-exponential decay fit for each wire. **(C)** Fourier transform spectra of corresponding residuals.

6.4.2 Diameter Dependence

In order to strengthen our understanding of the geometric aspects that influence acoustic phonon mods in VO_2 nanowires, we consider diameter as a simplistic fundamental parameter. Nanowire diameters were measured using SEM imaging. The diameters were measured at specific points along each wire where data was collected. Uniform diameters (like the uniform transient response) were observed along the length of each wire. Figure 6.6 shows data collected for three additional VO_2 NWs, NW4, NW5, and NW6 with diameters of 220 nm, 230 nm, and 340 nm respectively. Ideally a wider range of diameters would be more suitable, however our experiment is limited in the range of NW diameters that provide adequate pump-probe signal. This is likely due to the pump and probe wavelengths where smaller NWs give less signal in general, and larger wires do not transmit sufficient probe light for detection. Figure 6.6A shows the normalized transient curves for all three NWs. Data for NW6 was collected at a single localized point along the interior of the wire. However, in order to increase the signal to noise, data for NW4 and NW5 were taken as an average of several homogeneous interior positions along each wire. Just like the previous analysis for NW1 and NW3, the transients were fit to multi-exponential decays and the corresponding residuals (Figure 6.6B) represent the transient acoustic response. The Fourier transform spectra of the residuals is shown in Figure 6.6C. Again, neglecting frequencies below 10 GHz, the FT spectra are directly comparable to those for the interior points in NW1 and NW3, each with two dominant frequency peaks, one appearing near 20 GHz and a higher frequency peak above 40 GHz. Interestingly, the position period of these modes is correlated to nanowire diameter. Note that NW5 and NW1, which both have a measured diameter of 230 nm, exhibit almost identical FT spectra.

The two modes observed between 10 GHz and 70 GHz can be attributed to the fundamental breathing mode and overtone of the nanowire. These results are similar to those observed for semiconducting CdTe NWs.[56,57] The breathing modes ω_{br} for a NW modeled as a long isotropic cylinder can be found in the literature using the equation:[55-57]

$$\omega_{br} = \frac{\xi_n}{a} c_L \qquad \text{Eq. 6.3}$$

where ξ_n is the eigenvalue for the breathing mode, c_L is the longitudinal speed of sound and a is radius of the NW. The eigenvalue for the breathing mode and fundamental mode can be obtained by finding the roots of the Bessel function (J_o):

$$\xi_n J_0(\xi_n) = \frac{1-2\nu}{1-\nu} J_1(\xi_n) \qquad \text{Eq. 6.4}$$

where ν is Poisson's ratio (a property of the material) and $J_m(\xi)$ are Bessel functions of order m. The first root corresponds to the fundamental breathing mode while the second root corresponds to the overtone.

From Eq. 6.4 and 6.3, we can predict the periods (τ_{br}) for the fundamental breathing mode and overtone for VO_2 using the Poisson's ratio, ν, of 0.3[73] and 4000 m/s for c_L.[22] The predicted and experimental mode periods are shown together in Figure 6.7 as a function of nanowire diameter. The predicted periods are depicted as spheres with blue corresponding to the fundamental breathing mode and purple representing the overtone. NW1 (d = 230 nm) is represented by squares. NW3 (d = 260 nm) is represented by diamonds. NW4 (d = 220 nm) is represented by triangles. NW5 (d = 230 nm) is represented by stars and NW6 (d = 340 nm) is represented by circles. Like the theoretical values, blue symbols represent the fundamental breathing mode and purple symbols represent the overtone. The results are also summarized in Table 6.1.

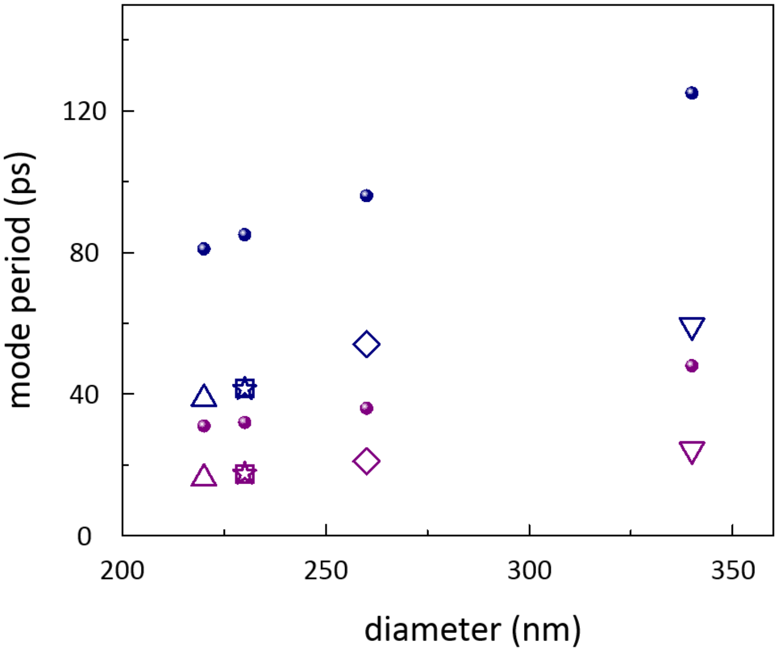

Figure 6.7: Diameter dependence. Fundamental (blue) and overtone (purple) mode period as a function of nanowire diameter for 5 NWs. NW1 (d = 230 nm) is represented by squares. NW3 (d = 260 nm) is represented by diamonds. NW4 (d = 220 nm) is represented by triangles. NW5 (d = 230 nm) is represented by stars and NW6 (d = 340 nm) is represented by circles. Solid spheres represent the predicted fundamental breathing mode (blue) and overtone (purple) using expressions from reference 57.

Table 6.1: Summary of experimental and theoretical values for the fundamental, $\tau_{br}^{(0)}$, and overtone, $\tau_{br}^{(1)}$, breathing mode periods of VO$_2$ NWs.

Wire	Symbol	Diameter (nm)	Experimental $\tau_{br}^{(0)}$ (ps)	Theoretical $\tau_{br}^{(0)}$ (ps)	Experimental $\tau_{br}^{(1)}$ (ps)	Theoretical $\tau_{br}^{(1)}$ (ps)
NW4	Triangle	220	38.7	81	16.2	31
NW1	Square	230	41.5	85	17.5	32
NW5	Star	230	41.4	85	17.5	32
NW3	Diamond	260	54.1	96	21.0	36
NW6	Circle	340	59.4	125	24.3	48

Though the overall trend of the theoretical model is preserved, the fundamental and overtone modes in our experiments have periods with values that are almost consistently 50 % lower than the predicted values. This discrepancy can be explained by several differences between the theoretical assumptions and the experiment itself. First, the model was developed for ultrafast laser-induced heating of elastically isotropic cylinders where the thermal pulse is modeled by the application of an initial uniform strain. Since the experiment employs a tightly focused laser pulse incident on a diffraction-limited spot along the axis of a wire, the initial strain is not uniform. Also, in an earlier discussion, we noted that the excitation of acoustic phonons in VO_2 NWs is likely due to a deformation potential mechanism, as opposed to laser-induced heating. This conclusion is supported by the observed anisotropic coherent acoustic phonon response. In such a case, our samples cannot be accurately described as elastically isotropic.

Next we consider the geometry of the NW samples. The theoretical model applies to perfectly cylindrical wires. While we cannot be certain of the NW cross-sections from the SEM images alone, similar growth conditions have produced wires with hexagonal and rectangular cross-sections.[50,51] One example from the literature demonstrated the growth of ultra-long, free-standing VO_2 MNWs.[51] In these samples, the wires were shown to have smooth surfaces and semi-round tips. In the SEM images in Figure 6.5A, NW1 and NW3 also appear to have rounded tips. It is therefore conceivable that the tips of the wires exhibit a more cylindrical symmetry. This could explain the appearance of only one peak in the FT spectra, the value of which is closer to that of the theoretical prediction for the fundamental breathing mode. Hexagonal or rectangular cross-sections with unknown aspect-ratios along the interior of the wires could explain the increased complexity of the observed mode patterns and increased deviation from the model. Lastly, it is worth mentioning that since the pump-probe experiments were performed at pulse energies just below the transition threshold, the observed mode patterns in the VO_2 nanowires could be further complicated by the onset of the IMT. This idea is supported by the behavior of the modes in the low frequency regime as the pump fluence approaches the IMT threshold.

6.5 Low Frequency Modes

6.5.1 Possible Mechanisms

Extensional Mode

We now turn our attention to the slow variation in signal over long timescales which is present in nearly all data collected at interior positions along the axis and is particularly dramatic for NW6. In the aforementioned theoretical model presented by Hartland and coworkers,[55,56] another type of coherent acoustic motion is predicted in nanowires which results from an extensional mode, where an increase in length is accompanied by a contraction in radius. The frequency of the extensional mode, which is much lower than that of the breathing mode, can be described by the expression:

$$\omega_{ext} = \frac{(2n+1)}{L}\pi\sqrt{\frac{E}{\rho_m}} \qquad \text{Eq. 6.5}$$

where L is the length of the wire, E is the Young's modulus, and ρ_m is the density. Though a detailed analysis of the low frequency oscillations in the previous discussion is impractical considering the limited number of recurrences in the time window of the delay stage, considering Eq. 6.5 and the extremely long length of the NWs in this study (on the order of 100 μm), predicted periods of oscillation would be on the order 10's of nanoseconds. We therefore conclude that this is not the mechanism driving the evolution of the transient signals in VO_2 wires at long times.

Shear Modes

The photoinduced stress itself is mostly depends on the optical, mechanical, and thermal properties of the material as well as laser characteristics such as pump wavelength and spot size. Additionally, in sub-micrometer films, the manner in which acoustic waves couple into the lattice is largely governed geometry. For example, in isotropic thin films under effectively homogeneous laser excitation (the ratio of the spot size incident on the film to the film thickness is much larger than unity), photoinduced stress leads to the propagation of longitudinal acoustic (LA) modes.[64,72,74] In this case, mechanical energy transferred from the pump pulse into the lattice introduces a plane stress wave in the depth direction that bounces back and forth at the interfaces of the thin film sample. The absorption and reflection properties of the probe pulse are altered by the strain in the lattice resulting in a change in the transmitted (or reflected) probe intensity. As the lattice returns to original position the signal recurs and the period of recurrence is linearly related to the thickness of the film.

Shear or transverse acoustic modes have also been observed in thin film samples. Though their generation and detection is not as straightforward and generally less efficient than that of longitudinal modes, several mechanisms have been demonstrated.[65-70,72,75] The most simplistic approach is through conversion of LA modes at reflection interfaces. At the interface of two isotropic materials, transverse modes can be generated by conversion of LA modes by reflection at oblique incidence.[65] Direct ultrafast optical excitation and detection of transverse acoustic phonon pulses has also been achieved in anisotropic materials with broken symmetry[65-67,70] and in isotropic materials using inhomogeneous laser excitation.[68,69] Though we wouldn’t expect to see longitudinal modes in nanowires due to geometry constraints, a similar excitation mechanism, coupled with focused laser excitation in an anisotropic material, could lead to the generation of shear acoustic pulses in our samples. In this case, the signal could arise from oscillating strain in the nanowire lattice where the mode frequency and period would be related to geometry and anisotropy of the wires as well as the spot size of the laser excitation.[36,41,42,68,76]

6.5.2 Experimental Results

In the following data, we have extended the length of the delay stage to more accurately examine the prominent modes below 5 GHz. In Figure 6.8 we present pump-probe transient data for a point on VO_2 NW7, indicated by the red circle in the zero ps pump-probe delay image in Figure 6.8C. Low frequency modes (with a period of approximately 700 ps) are clearly distinguished in the transient data (Figure 6.8A) as well as the residuals shown in the inset of Figure 6.8B. The behavior of the ~700 ps mode is investigated as a function of pump pulse fluence just below the IMT threshold. Regardless of pump fluence the temporal appearance of successive recurrences vary with pump-probe delay, increasing as delay increases. As the pump pulse fluence nears the transition threshold, the magnitude of the oscillations increase and the period shifts to slightly longer timescales. In the Fourier transform spectrum for the lowest pulse energy (12 pJ/pulse) the maximum of the low frequency peak corresponds to a period of 670 ps. At 30 pJ/pulse the corresponding period is 780 ps. This could be attributed to a phonon softening phenomenon as the transition threshold for the metallic phase is reached, similar to that of optical phonons.[77] This concept is more easily visualized in Figure 6.8D where the background signal is subtracted from the transient data in Figure 6.8A. Here the pump pulse energy is plotted on the y axis as a function of pump-probe delay and the corresponding transient response for each pulse energy is depicted on a color scale from 0 to 2.5. In this illustration the delayed onset of the recurrences as a function of pump-probe delay and pulse energy is more apparent.

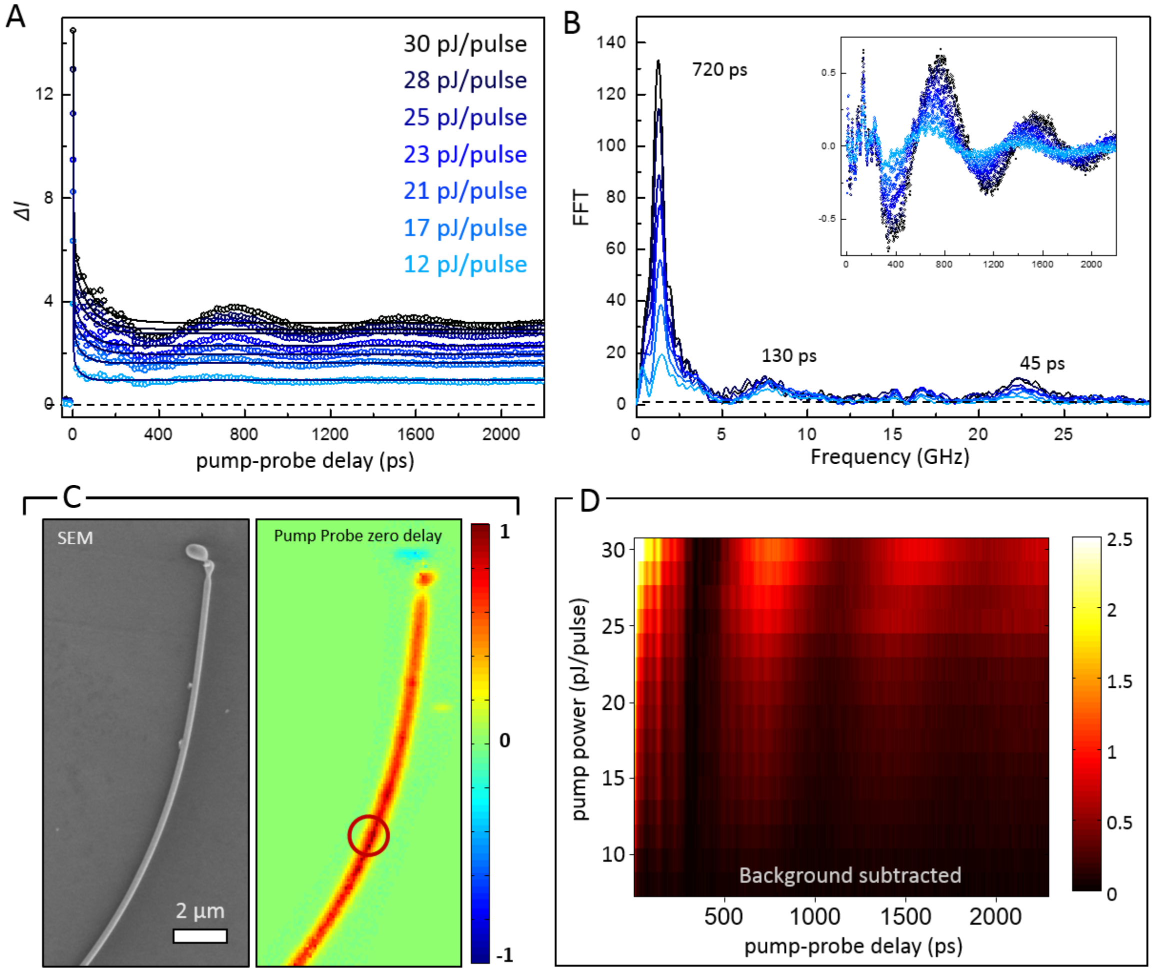

Figure 6.8: Power dependence (A) Transient decay traces at various pump fluences below the phase transition at a spatially-localized point on VO_2 NW7 **(B)** Fourier transform spectra for the residuals (inset) of multi-exponential fits of the transients in 6.7A **(C)** SEM and corresponding zero ps pump-probe delay image for NW where the red circle indicates the position where data was collected. Scale bar is 2 µm. **(D)** Background Subtracted transient data from Figure 6.8A where pump pulse energy is plotted as a function of pump-probe delay and the corresponding transient response is displayed on a color scale from 0 to 2.5.

6.6 Propagation of Acoustic Phonon Modes

The assumption that the low frequency modes are caused by a transverse or shear strain in the lattice is supported by images collected in the SSPP configuration. As mentioned previously, the slow oscillating signal is not apparent for points at the ends of the nanowires. Accordingly, at the ends of the wire, no clear transverse propagation of signal is observed (not shown). Therefore, to investigate the propagation of modes caused by shear stress, we only consider positions along interior of the nanowire axis.[65] Figure 6.9 shows a series of SSPP images collected at a single point on NW6 using a pump pulse energy of 12 pJ/pulse. The SSPP images were collected with the pump held fixed on the position indicated by the red circle on the SEM image. The probe beam was scanned across the wire at pump-probe decays indicated above each frame. The dotted lines on each SSPP image illustrate the approximate position of the nanowire. Each image is normalized such that maximum positive-going signal corresponds to a value of 1. Clear waves propagating outward are apparent beginning in the frame collected at 240 ps. By 960 ps a couple more waves have grown in and continue to propagate outward along the axis of the wire. A similar result for nanoacoustic wave generation with a nanoscale spot size has recently been reported for free-standing copper nanowires.[60] However, this is the first report for VO_2 nanowires, and first example of direct imaging of acoustic phonon propagation in individual NWs.

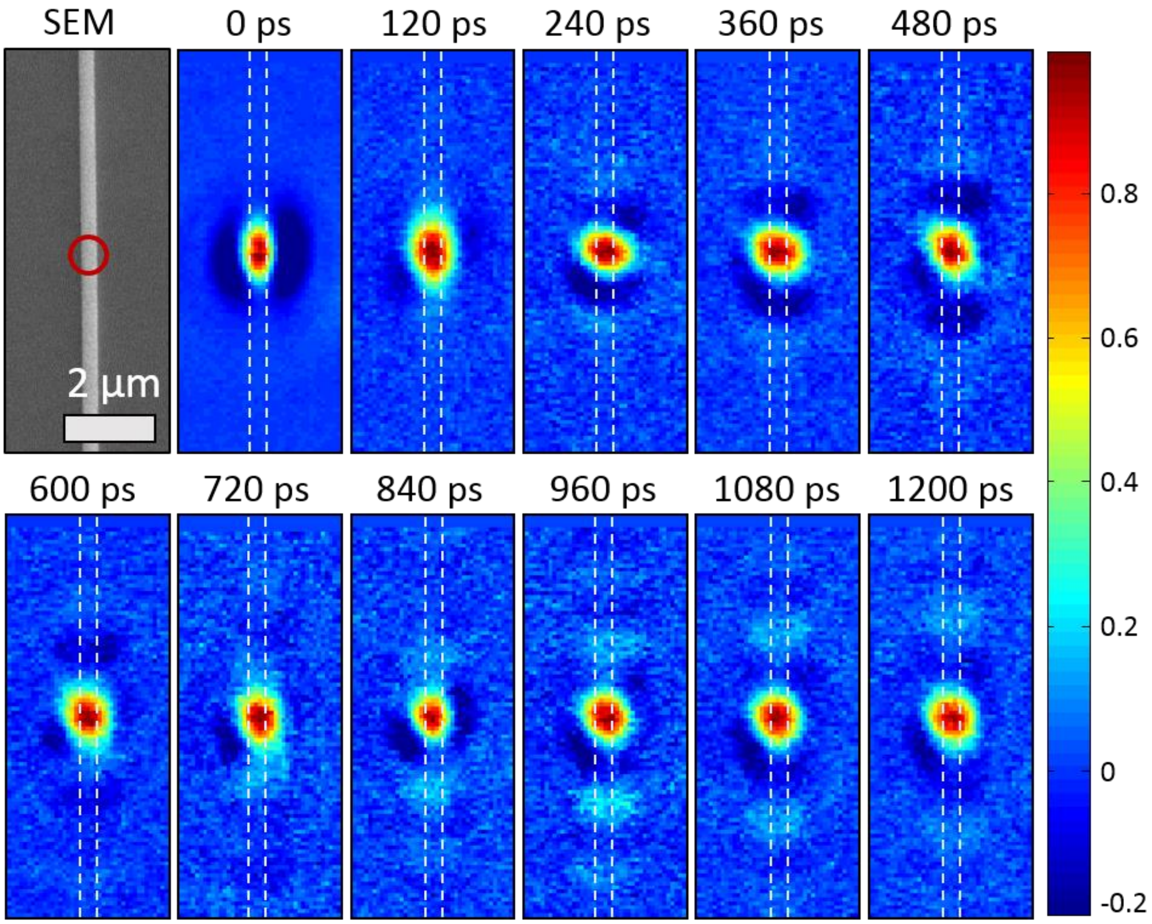

Figure 6.9: Spatially-separated pump-probe images of propagating shear modes. SEM image of a region of VO2 NW6. SSPP images were collected with the pump held fixed on the position indicated by the red circle on the SEM image. The probe beam was scanned across the wire at pump-probe decays indicated above each frame. The dotted lines on each SSPP image illustrate the approximate position of the nanowire. Each image is normalized such that maximum positive-going signal corresponds to a value of 1. All images are represented on the same spatial scale. The scale bar on the SEM image is 2 μm.

In order to quantitatively analyze the propagation of these acoustic waves, we spatially separate the pump and probe pulses at various spatial distances (Δ_{pp}) along the axis of the nanowire and scan the pump-probe delay. An SEM and pump-probe image of the investigated region of NW6 are shown in Figure 6.10A. The fixed pump position is indicated by a black circle. The various probe positions are indicated by the color-coded numbered circles. At large enough spatial separations, such that there is minimal Gaussian overlap of the pump and probe spots, a wave in the signal emerges corresponding to the arrival of a transverse acoustic pulse. Traces are shown in Figure 6.10B for probe positions 1-7, corresponding to Δ_{pp} = 1.7 µm, 1.9 µm, 2.3 µm, 2.7 µm, 3.1 µm, 3.8 µm, and 4.6 µm, respectively. The propagation velocity of the acoustic pulse is estimated using a plot of Δ_{pp} as a function of the arrival time of the first peak in the acoustic wave (dark red triangles). The plot shown in Figure 6.10C follows a linear trend where the velocity of wave propagation is estimated by the slope of the linear fit (black dashed line). Here, the slope corresponds to an acoustic wave velocity of 5370 m/s which is comparable to the known value for the speed of sound in VO_2 (4000 m/s).[22]

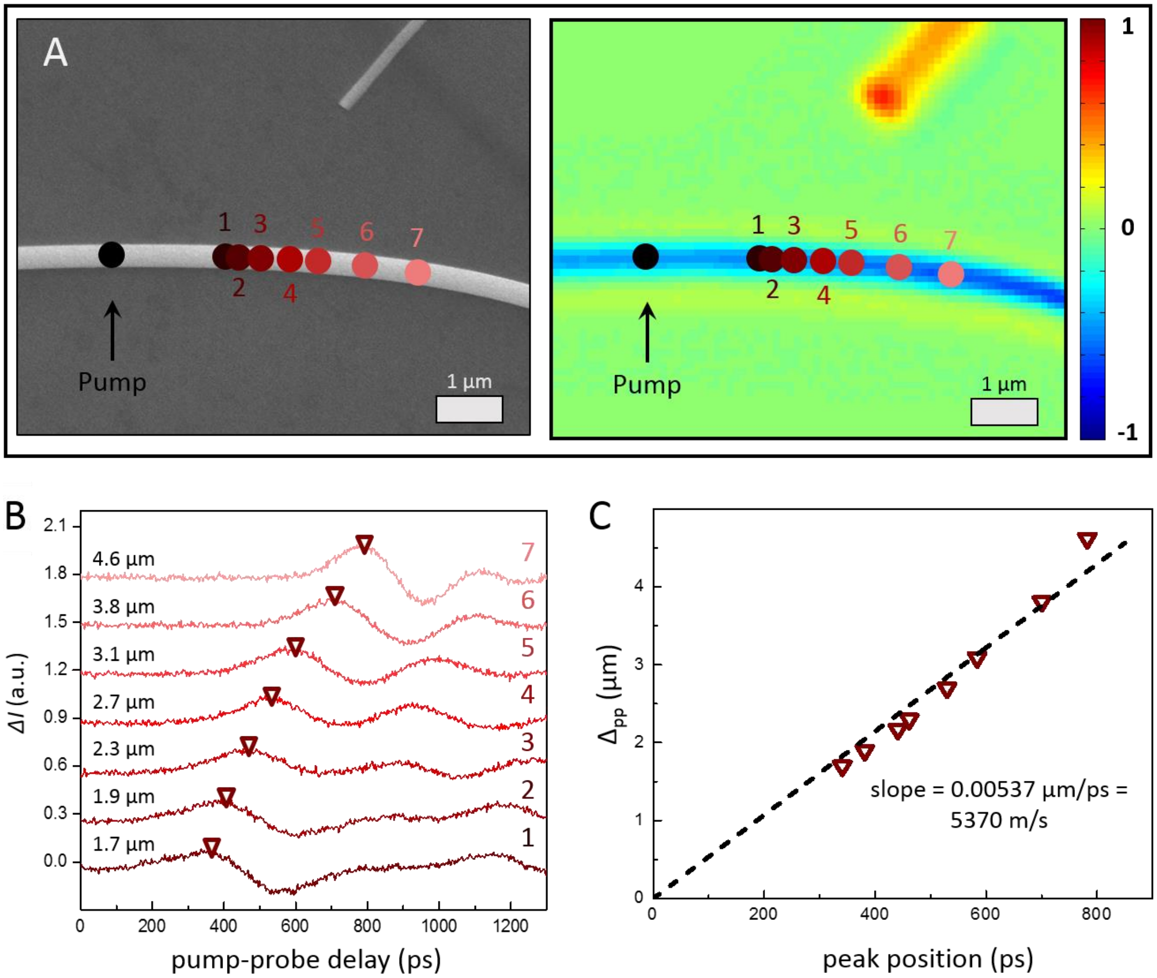

Figure 6.10: Propagation of modes (A) SEM of a VO_2 NW6 (left) and corresponding pump-probe image collected at zero ps delay (right). Scale bars are 1 µm. The pump-probe image is depicted using a normalized color scale. **(B)** Transient curves collected at various pump-probe spatial separations from 1.7 µm to 4.6 um, indicated above each trace. Pump and probe positions of traces 1 – 7 are indicated on the images in Figure 6.10A. **(C)** Plot of pump-probe spatial separations (Δ_{pp}) as a function of peak positon in time (ps) as estimated from 6.10B and indicated by dark red triangles on each trace. The dashed black line is the linear fit of peak position vs Δ_{pp}. The slope (5370 m/s) represents an estimation of how mode propagation along the length of the NW axis.

6.7 Conclusions

In summary, we have applied optical transient absorption pump-probe microscopy to study the insulator-to-metal transition and coherent acoustic phonon dynamics in VO_2 nanowires. Using two ultrafast laser pulses, both focused to diffraction-limited positions in VO_2 NWs, we have investigated the onset and evolution of the IMT. Using our SSPP imaging technique, we have imaged the spatial evolution of the thermal expansion of the phase transition at pump pulse energies above the transition threshold. At lower pump pulse energies just below the transition threshold, we have observed the anisotropic appearance of complex recurrence patterns in the transient signal. We have demonstrated that these complicated signals result from impulsive excitation of an elaborate combination of several coherent acoustic phonon modes that coexist in the NW lattice as a result of geometry and inhomogeneous excitation. The geometry dependence is supported through the position dependent mode patterns compared at the ends of the NWs vs positions along the interior of the NWs. Additionally, we have shown that the frequency of breathing modes depends on NW diameter. While the breathing modes show negligible spatial expansion along the axis of the wire, we have imaged and briefly analyzed the propagation of lower frequency modes that we attribute to inhomogeneous laser-induced shear strain along the nanowire axis. These results demonstrate an efficient and contactless method for the investigation of electronic, mechanical, and elastic properties of nanomaterials necessary for the rational design of new nanoscale devices. Additional quantitative analysis and finite element models would be beneficial for understanding the complex behavior of coherent acoustic modes near the IMT of VO_2, however, such rigorous approaches, which are reserved for future investigations, are beyond the scope of this initial report.

REFERENCES

1 Goodenough, J. B. Direct Cation- -Cation Interactions in Several Oxides. *Physical Review* **117**, 1442-1451, (1960).

2 Goodenough, J. B. The two components of the crystallographic transition in VO_2. *Journal of Solid State Chemistry* **3**, 490-500, (1971).

3 Wentzcovitch, R. M., Schulz, W. W. & Allen, P. B. VO_2: Peierls or Mott-Hubbard? A view from band theory. *Physical Review Letters* **72**, 3389-3392, (1994).

4 Eyert, V. The metal-insulator transitions of VO_2: A band theoretical approach. *Annalen der Physik* **11**, 650-704, (2002).

5 Zylbersztejn, A. & Mott, N. F. Metal-insulator transition in vanadium dioxide. *Physical Review B* **11**, 4383-4395, (1975).

6 Kim, H.-T., Lee, Y. W., Kim, B.-J., Chae, B.-G., Yun, S. J., Kang, K.-Y., Han, K.-J., Yee, K.-J. & Lim, Y.-S. Monoclinic and Correlated Metal Phase in VO_2 as Evidence of the Mott Transition: Coherent Phonon Analysis. *Physical Review Letters* **97**, 266401, (2006).

7 Pouget, J. P., Launois, H., Rice, T. M., Dernier, P., Gossard, A., Villeneuve, G. & Hagenmuller, P. Dimerization of a linear Heisenberg chain in the insulating phases of VO_2. *Physical Review B* **10**, 1801-1815, (1974).

8 Pouget, J. P., Launois, H., D'Haenens, J. P., Merenda, P. & Rice, T. M. Electron Localization Induced by Uniaxial Stress in Pure VO_2. *Physical Review Letters* **35**, 873-875, (1975).

9 Koethe, T. C., Hu, Z., Haverkort, M. W., Schüßler-Langeheine, C., Venturini, F., Brookes, N. B., Tjernberg, O., Reichelt, W., Hsieh, H. H., Lin, H. J., Chen, C. T. & Tjeng, L. H. Transfer of Spectral Weight and Symmetry across the Metal-Insulator Transition in VO_2. *Physical Review Letters* **97**, 116402, (2006).

10 Wegkamp, D., Herzog, M., Xian, L., Gatti, M., Cudazzo, P., McGahan, C. L., Marvel, R. E., Haglund, R. F., Rubio, A., Wolf, M. & Stähler, J. Instantaneous Band Gap Collapse in Photoexcited Monoclinic VO_2 due to Photocarrier Doping. *Physical Review Letters* **113**, 216401, (2014).

11 Maurer, D., Leue, A., Heichele, R. & Müller, V. Elastic behavior near the metal-insulator transition of VO_2. *Physical Review B* **60**, 13249-13252, (1999).

12 Arcangeletti, E., Baldassarre, L., Di Castro, D., Lupi, S., Malavasi, L., Marini, C., Perucchi, A. & Postorino, P. Evidence of a Pressure-Induced Metallization Process in Monoclinic VO_2. *Physical Review Letters* **98**, 196406, (2007).

13 Cavalleri, A., Dekorsy, T., Chong, H. H. W., Kieffer, J. C. & Schoenlein, R. W. Evidence for a structurally-driven insulator-to-metal transition in VO_2: A view from the ultrafast timescale. *Physical Review B* **70**, 161102, (2004).

14 Paquet, D. & Leroux-Hugon, P. Electron correlations and electron-lattice interactions in the metal-insulator, ferroelastic transition in VO_2: A thermodynamical study. *Physical Review B* **22**, 5284-5301, (1980).

15 Booth, J. M. & Casey, P. S. Anisotropic Structure Deformation in the VO_2 Metal-Insulator Transition. *Physical Review Letters* **103**, 086402, (2009).

16 Biermann, S., Poteryaev, A., Lichtenstein, A. I. & Georges, A. Dynamical Singlets and Correlation-Assisted Peierls Transition in VO_2. *Physical Review Letters* **94**, 026404, (2005).

17 Haverkort, M. W., Hu, Z., Tanaka, A., Reichelt, W., Streltsov, S. V., Korotin, M. A., Anisimov, V. I., Hsieh, H. H., Lin, H. J., Chen, C. T., Khomskii, D. I. & Tjeng, L. H. Orbital-Assisted Metal-Insulator Transition in VO_2. *Physical Review Letters* **95**, 196404, (2005).

18 Dachraoui, H., Müller, N., Obermeier, G., Oberer, C., Horn, S. & Heinzmann, U. Interplay between electronic correlations and coherent structural dynamics during the monoclinic insulator-to-rutile metal phase transition in VO_2. *Journal of Physics: Condensed Matter* **23**, 435402, (2011).

19 Yoshida, R., Yamamoto, T., Ishida, Y., Nagao, H., Otsuka, T., Saeki, K., Muraoka, Y., Eguchi, R., Ishizaka, K., Kiss, T., Watanabe, S., Kanai, T., Itatani, J. & Shin, S. Ultrafast photoinduced transition of an insulating VO_2 thin film into a nonrutile metallic state. *Physical Review B* **89**, 205114, (2014).

20 Morrison, V. R., Chatelain, R. P., Tiwari, K. L., Hendaoui, A., Bruhács, A., Chaker, M. & Siwick, B. J. A photoinduced metal-like phase of monoclinic VO_2 revealed by ultrafast electron diffraction. *Science* **346**, 445-448, (2014).

21 Tao, Z., Han, T.-R. T., Mahanti, S. D., Duxbury, P. M., Yuan, F., Ruan, C.-Y., Wang, K. & Wu, J. Decoupling of Structural and Electronic Phase Transitions in VO_2. *Physical Review Letters* **109**, 166406, (2012).

22 Baum, P., Yang, D.-S. & Zewail, A. H. 4D Visualization of Transitional Structures in Phase Transformations by Electron Diffraction. *Science* **318**, 788-792, (2007).

23 Liu, H., Kwon, O.-H., Tang, J. & Zewail, A. H. 4D Imaging and Diffraction Dynamics of Single-Particle Phase Transition in Heterogeneous Ensembles. *Nano Letters* **14**, 946-954, (2014).

24 Cavalleri, A., Tóth, C., Siders, C. W., Squier, J. A., Ráksi, F., Forget, P. & Kieffer, J. C. Femtosecond Structural Dynamics in VO_2 during an Ultrafast Solid-Solid Phase Transition. *Physical Review Letters* **87**, 237401, (2001).

25 Hada, M., Okimura, K. & Matsuo, J. Characterization of structural dynamics of VO_2 thin film on *c*-Al_2O_3 using in-air time-resolved x-ray diffraction. *Physical Review B* **82**, 153401, (2010).

26 Hsieh, W.-P., Trigo, M., Reis, D. A., Andrea Artioli, G., Malavasi, L. & Mao, W. L. Evidence for photo-induced monoclinic metallic VO_2 under high pressure. *Applied Physics Letters* **104**, 021917, (2014).

27 Cocker, T. L., Titova, L. V., Fourmaux, S., Holloway, G., Bandulet, H. C., Brassard, D., Kieffer, J. C., El Khakani, M. A. & Hegmann, F. A. Phase diagram of the ultrafast photoinduced insulator-metal transition in vanadium dioxide. *Physical Review B* **85**, 155120, (2012).

28 Kübler, C., Ehrke, H., Huber, R., Lopez, R., Halabica, A., Haglund, R. F. & Leitenstorfer, A. Coherent Structural Dynamics and Electronic Correlations during an Ultrafast Insulator-to-Metal Phase Transition in VO_2. *Physical Review Letters* **99**, 116401, (2007).

29 Pashkin, A., Kübler, C., Ehrke, H., Lopez, R., Halabica, A., Haglund, R. F., Huber, R. & Leitenstorfer, A. Ultrafast insulator-metal phase transition in VO_2 studied by multiterahertz spectroscopy. *Physical Review B* **83**, 195120, (2011).

30 Wall, S., Wegkamp, D., Foglia, L., Appavoo, K., Nag, J., Haglund, R. F., Stähler, J. & Wolf, M. Ultrafast changes in lattice symmetry probed by coherent phonons. *Nat Commun* **3**, 721, (2012).

31 Wall, S., Foglia, L., Wegkamp, D., Appavoo, K., Nag, J., Haglund, R. F., Stähler, J. & Wolf, M. Tracking the evolution of electronic and structural properties of VO_2 during the ultrafast photoinduced insulator-metal transition. *Physical Review B* **87**, 115126, (2013).

32 Hilton, D. J., Prasankumar, R. P., Fourmaux, S., Cavalleri, A., Brassard, D., El Khakani, M. A., Kieffer, J. C., Taylor, A. J. & Averitt, R. D. Enhanced Photosusceptibility near $\boldsymbol{T}_c$ for the Light-Induced Insulator-to-Metal Phase Transition in Vanadium Dioxide. *Physical Review Letters* **99**, 226401, (2007).

33 Xue, X., Jiang, M., Li, G., Lin, X., Ma, G. & Jin, P. Photoinduced insulator-metal phase transition and the metallic phase propagation in VO2 films investigated by time-resolved terahertz spectroscopy. *Journal of Applied Physics* **114**, 193506, (2013).

34 Lysenko, S., Fernández, F., Rúa, A. & Liu, H. Ultrafast light scattering imaging of multi-scale transition dynamics in vanadium dioxide. *Journal of Applied Physics* **114**, 153514, (2013).

35 Huffman, T. J., Xu, P., Qazilbash, M. M., Walter, E. J., Krakauer, H., Wei, J., Cobden, D. H., Bechtel, H. A., Martin, M. C., Carr, G. L. & Basov, D. N. Anisotropic infrared response of vanadium dioxide microcrystals. *Physical Review B* **87**, 115121, (2013).

36 Atkin, J. M., Berweger, S., Chavez, E. K., Raschke, M. B., Cao, J., Fan, W. & Wu, J. Strain and temperature dependence of the insulating phases of VO_2 near the metal-insulator transition. *Physical Review B* **85**, 020101, (2012).

37 Jones, A. C., Berweger, S., Wei, J., Cobden, D. & Raschke, M. B. Nano-optical Investigations of the Metal−Insulator Phase Behavior of Individual VO_2 Microcrystals. *Nano Letters* **10**, 1574-1581, (2010).

38 Sohn, J. I., Joo, H. J., Ahn, D., Lee, H. H., Porter, A. E., Kim, K., Kang, D. J. & Welland, M. E. Surface-Stress-Induced Mott Transition and Nature of Associated Spatial Phase Transition in Single Crystalline VO_2 Nanowires. *Nano Letters* **9**, 3392-3397, (2009).

39 Wei, J., Wang, Z., Chen, W. & Cobden, D. H. New aspects of the metal-insulator transition in single-domain vanadium dioxide nanobeams. *Nat Nano* **4**, 420-424, (2009).

40 Wu, J., Gu, Q., Guiton, B. S., de Leon, N. P., Ouyang, L. & Park, H. Strain-Induced Self Organization of Metal−Insulator Domains in Single-Crystalline VO2 Nanobeams. *Nano Letters* **6**, 2313-2317, (2006).

41 Cao, J., Ertekin, E., Srinivasan, V., Fan, W., Huang, S., Zheng, H., Yim, J. W. L., Khanal, D. R., Ogletree, D. F., Grossman, J. C. & Wu, J. Strain engineering and one-dimensional organization of metal-insulator domains in single-crystal vanadium dioxide beams. *Nat Nano* **4**, 732-737, (2009).

42 Cao, J., Gu, Y., Fan, W., Chen, L. Q., Ogletree, D. F., Chen, K., Tamura, N., Kunz, M., Barrett, C., Seidel, J. & Wu, J. Extended Mapping and Exploration of the Vanadium Dioxide Stress-Temperature Phase Diagram. *Nano Letters* **10**, 2667-2673, (2010).

43 Mehl, B. P., Kirschbrown, J. R., House, R. L. & Papanikolas, J. M. The End Is Different than The Middle: Spatially Dependent Dynamics in ZnO Rods Observed by Femtosecond Pump–Probe Microscopy. *The Journal of Physical Chemistry Letters* **2**, 1777-1781, (2011).

44 Mehl, B. P., Kirschbrown, J. R., Gabriel, M. M., House, R. L. & Papanikolas, J. M. Pump-Probe Microscopy: Spatially Resolved Carrier Dynamics in ZnO Rods and the Influence of Optical Cavity Resonator Modes. *Journal of Physical Chemistry B* **117**, 4390-4398, (2013).

45 Gabriel, M. M., Kirschbrown, J. R., Christesen, J. D., Pinion, C. W., Zigler, D. F., Grumstrup, E. M., Mehl, B. P., Cating, E. E. M., Cahoon, J. F. & Papanikolas, J. M. Direct Imaging of Free Carrier and Trap Carrier Motion in Silicon Nanowires by Spatially-Separated Femtosecond Pump-Probe Microscopy. *Nano Letters* **13**, 1336-1340, (2013).

46 Grumstrup, E. M., Gabriel, M. M., Pinion, C. W., Parker, J. K., Cahoon, J. F. & Papanikolas, J. M. Reversible Strain-Induced Electron–Hole Recombination in Silicon Nanowires Observed with Femtosecond Pump–Probe Microscopy. *Nano Letters* **14**, 6287-6292, (2014).

47 Gabriel, M. M., Grumstrup, E. M., Kirschbrown, J. R., Pinion, C. W., Christesen, J. D., Zigler, D. F., Cating, E. E. M., Cahoon, J. F. & Papanikolas, J. M. Imaging Charge Separation and Carrier Recombination in Nanowire p-i-n Junctions Using Ultrafast Microscopy. *Nano Letters* **14**, 3079-3087, (2014).

48 Grumstrup, E. M., Gabriel, M. M., Cating, E. M., Pinion, C. W., Christesen, J. D., Kirschbrown, J. R., Vallorz, E. L., Cahoon, J. F. & Papanikolas, J. M. Ultrafast Carrier Dynamics in Individual Silicon Nanowires: Characterization of Diameter-Dependent Carrier Lifetime and Surface Recombination with Pump–Probe Microscopy. *The Journal of Physical Chemistry C* **118**, 8634-8640, (2014).

49 Grumstrup, E. M., Gabriel, M. M., Cating, E. E. M., Van Goethem, E. M. & Papanikolas, J. M. Pump–probe microscopy: Visualization and spectroscopy of ultrafast dynamics at the nanoscale. *Chemical Physics* **458**, 30-40, (2015).

50 Guiton, B. S., Gu, Q., Prieto, A. L., Gudiksen, M. S. & Park, H. Single-Crystalline Vanadium Dioxide Nanowires with Rectangular Cross Sections. *Journal of the American Chemical Society* **127**, 498-499, (2005).

51 Cheng, C., Liu, K., Xiang, B., Suh, J. & Wu, J. Ultra-long, free-standing, single-crystalline vanadium dioxide micro/nanowires grown by simple thermal evaporation. *Applied Physics Letters* **100**, 103111, (2012).

52 Appavoo, K., Wang, B., Brady, N. F., Seo, M., Nag, J., Prasankumar, R. P., Hilton, D. J., Pantelides, S. T. & Haglund, R. F. Ultrafast Phase Transition via Catastrophic Phonon Collapse Driven by Plasmonic Hot-Electron Injection. *Nano Letters* **14**, 1127-1133, (2014).

53 Grumstrup, E. M., Cating, E. M., Gabriel, M. M., Pinion, C. W., Christesen, J. D., Kirschbrown, J. R., Vallorz, E. L., Cahoon, J. F. & Papanikolas, J. M. Ultrafast Carrier Dynamics of Silicon Nanowire Ensembles: The Impact of Geometrical Heterogeneity on Charge Carrier Lifetime. *The Journal of Physical Chemistry C* **118**, 8626-8633, (2014).

54 O'Callahan, B. T., Jones, A. C., Hyung Park, J., Cobden, D. H., Atkin, J. M. & Raschke, M. B. Inhomogeneity of the ultrafast insulator-to-metal transition dynamics of VO_2. *Nat Commun* **6**, (2015).

55 Hu, M., Wang, X., Hartland, G. V., Mulvaney, P., Juste, J. P. & Sader, J. E. Vibrational Response of Nanorods to Ultrafast Laser Induced Heating: Theoretical and Experimental Analysis. *Journal of the American Chemical Society* **125**, 14925-14933, (2003).

56 Major, T. A., Lo, S. S., Yu, K. & Hartland, G. V. Time-Resolved Studies of the Acoustic Vibrational Modes of Metal and Semiconductor Nano-objects. *The Journal of Physical Chemistry Letters* **5**, 866-874, (2014).

57 Lo, S. S., Major, T. A., Petchsang, N., Huang, L., Kuno, M. K. & Hartland, G. V. Charge Carrier Trapping and Acoustic Phonon Modes in Single CdTe Nanowires. *ACS Nano* **6**, 5274-5282, (2012).

58 Mansart, B., Boschetto, D., Sauvage, S., Rousse, A. & Marsi, M. Mott transition in Cr-doped V_2O_3 studied by ultrafast reflectivity: Electron correlation effects on the transient response. *EPL (Europhysics Letters)* **92**, 37007, (2010).

59 Ristow, O., Merklein, M., Grossmann, M., Hettich, M., Schubert, M., Bruchhausen, A., Grebing, J., Erbe, A., Mounier, D., Gusev, V., Scheer, E., Dekorsy, T. & Barretto, E. C. S. Ultrafast spectroscopy of super high frequency mechanical modes of doubly clamped beams. *Applied Physics Letters* **103**, 233114, (2013).

60 Jean, C., Belliard, L., Cornelius, T. W., Thomas, O., Toimil-Molares, M. E., Cassinelli, M., Becerra, L. & Perrin, B. Direct Observation of Gigahertz Coherent Guided Acoustic Phonons in Free-Standing Single Copper Nanowires. *The Journal of Physical Chemistry Letters* **5**, 4100-4104, (2014).

61 Cavalleri, A., Siders, C. W., Brown, F. L. H., Leitner, D. M., Tóth, C., Squier, J. A., Barty, C. P. J., Wilson, K. R., Sokolowski-Tinten, K., Horn von Hoegen, M., von der Linde, D. & Kammler, M. Anharmonic Lattice Dynamics in Germanium Measured with Ultrafast X-Ray Diffraction. *Physical Review Letters* **85**, 586-589, (2000).

62 Lindenberg, A. M., Kang, I., Johnson, S. L., Missalla, T., Heimann, P. A., Chang, Z., Larsson, J., Bucksbaum, P. H., Kapteyn, H. C., Padmore, H. A., Lee, R. W., Wark, J. S. & Falcone, R. W. Time-Resolved X-Ray Diffraction from Coherent Phonons during a Laser-Induced Phase Transition. *Physical Review Letters* **84**, 111-114, (2000).

63 Liu, M. K., Pardo, B., Zhang, J., Qazilbash, M. M., Yun, S. J., Fei, Z., Shin, J.-H., Kim, H.-T., Basov, D. N. & Averitt, R. D. Photoinduced Phase Transitions by Time-Resolved Far-Infrared Spectroscopy in V_2O_3. *Physical Review Letters* **107**, 066403, (2011).

64 Thomsen, C., Strait, J., Vardeny, Z., Maris, H. J., Tauc, J. & Hauser, J. J. Coherent Phonon Generation and Detection by Picosecond Light Pulses. *Physical Review Letters* **53**, 989-992, (1984).

65 Pezeril, T., Chigarev, N., Ruello, P., Gougeon, S., Mounier, D., Breteau, J. M., Picart, P. & Gusev, V. Laser acoustics with picosecond collimated shear strain beams in single crystals and polycrystalline materials. *Physical Review B* **73**, 132301, (2006).

66 Pezeril, T., Ruello, P., Gougeon, S., Chigarev, N., Mounier, D., Breteau, J. M., Picart, P. & Gusev, V. Generation and detection of plane coherent shear picosecond acoustic pulses by lasers: Experiment and theory. *Physical Review B* **75**, 174307, (2007).

67 Lejman, M., Vaudel, G., Infante, I. C., Gemeiner, P., Gusev, V. E., Dkhil, B. & Ruello, P. Giant ultrafast photo-induced shear strain in ferroelectric $BiFeO_3$. *Nat Commun* **5**, (2014).

68 Rossignol, C., Rampnoux, J. M., Perton, M., Audoin, B. & Dilhaire, S. Generation and Detection of Shear Acoustic Waves in Metal Submicrometric Films with Ultrashort Laser Pulses. *Physical Review Letters* **94**, 166106, (2005).

69 Harb, M., Peng, W., Sciaini, G., Hebeisen, C. T., Ernstorfer, R., Eriksson, M. A., Lagally, M. G., Kruglik, S. G. & Miller, R. J. D. Excitation of longitudinal and transverse coherent acoustic phonons in nanometer free-standing films of (001) Si. *Physical Review B* **79**, 094301, (2009).

70 Matsuda, O., Wright, O. B., Hurley, D. H., Gusev, V. E. & Shimizu, K. Coherent Shear Phonon Generation and Detection with Ultrashort Optical Pulses. *Physical Review Letters* **93**, 095501, (2004).

71 Ruello, P., Zhang, S., Laffez, P., Perrin, B. & Gusev, V. Laser-induced coherent acoustical phonons mechanisms in the metal-insulator transition compound $NdNiO_3$: Thermal and nonthermal processes. *Physical Review B* **79**, 094303, (2009).

72 Ruello, P. & Gusev, V. E. Physical mechanisms of coherent acoustic phonons generation by ultrafast laser action. *Ultrasonics* **56**, 21-35, (2015).

73 Nagashima, K., Yanagida, T., Tanaka, H. & Kawai, T. Stress relaxation effect on transport properties of strained vanadium dioxide epitaxial thin films. *Physical Review B* **74**, 172106, (2006).

74 Thomsen, C., Grahn, H. T., Maris, H. J. & Tauc, J. Surface generation and detection of phonons by picosecond light pulses. *Physical Review B* **34**, 4129-4138, (1986).

75 Hurley, D. H., Wright, O. B., Matsuda, O., Gusev, V. E. & Kolosov, O. V. Laser picosecond acoustics in isotropic and anisotropic materials. *Ultrasonics* **38**, 470-474, (2000).

76 Hu, B., Ding, Y., Chen, W., Kulkarni, D., Shen, Y., Tsukruk, V. V. & Wang, Z. L. External-Strain Induced Insulating Phase Transition in VO2 Nanobeam and Its Application as Flexible Strain Sensor. *Advanced Materials* **22**, 5134-5139, (2010).

77 Budai, J. D., Hong, J., Manley, M. E., Specht, E. D., Li, C. W., Tischler, J. Z., Abernathy, D. L., Said, A. H., Leu, B. M., Boatner, L. A., McQueeney, R. J. & Delaire, O. Metallization of vanadium dioxide driven by large phonon entropy. *Nature* **515**, 535-539, (2014).

CHAPTER 7: CONCLUSIONS

7.1 Summary

We have developed a diffraction-limited pump-probe microscope capable of probing materials on the nanoscale and comparing the properties of one particle to another, thus overcoming the limit of heterogeneity among samples by disentangling the many contributions from individual members within an ensemble.[1-7] We have also used this technique to study the distribution of physical properties along different positions within a single nanostructure, demonstrating that ultrafast optical properties can vary along a single particle as a result of inhomogeneity in geometry, defect concentration, and secondary structure. For example, we have shown that the electron-hole recombination processes vary from one point to the next within a single rod shaped ZnO crystal due to the spatial distribution of optical resonator modes supported within the varying cross-section diameter along the structure.[3,8] Additionally, in studies of silicon nanowires, we have shown that changes in secondary structure resulting from deformation potential can also affect electronic phenomena.[7,9] The combined spatial and temporal resolution of the pump-probe microscope and its contactless measurement capability make it well-suited to capture the complexities of charge carrier behavior with high throughput even in complex and sophisticated nanomaterials.

In a new imaging mode, we have extended the application of our pump-probe microscope to the direct visualization of transport properties in nanomaterials by photoexciting a single structure in one location and probing it in another. Spatially-separated pump-probe experiments on silicon nanowires have enabled direct observation of the evolution of excited charge carriers generated in a localized diffraction-limited spot along the nanowire axis.[2,4,10] In these experiments we have imaged ambipolar diffusion in intrinsic nanowires as well as drift of photoexcited charges in the presence of a built-in electric field in a nanowire junction. We have also demonstrated the relevance and versatility of the microscope and spatially-separated pump-probe configuration by examining the insulator-to-metal transition and coherent acoustic phonon dynamics in vanadium dioxide nanowires. We have imaged the spatial evolution of thermal diffusion along the axis of the VO_2 nanowires and, for the first time, directly imaged the propagation of coherent acoustic phonon modes along a nanostructure.

All of these results collectively establish the necessity for experimental techniques with combined spatial and temporal resolution to examine complex signals that are often hidden in the ensemble. This kind of detailed information regarding optical, electronic, and mechanical properties of individual nanostructures will only become more crucial as materials with greater complexity are targeted for sophisticated nanoscale electronic applications.

7.2 Challenges and Future Directions

Though several advances have been realized with conventional pump-probe microscopy, there is still room for improvement with additional quantitative analysis and theoretical modeling to more accurately understand the complex behavior of electron dynamics and acoustic mode behavior in nanomaterials. Additionally, the diffraction limit prevents resolution of structural features smaller than about 200 nm. While the work outlined in the previous chapters suggests a wealth of information is available to diffraction-limited techniques, the ability to probe smaller scales using higher resolution microscopies is still compelling. To this end, some early work from other groups has been implemented to improve the resolution of far field pump-probe experiments by utilizing methods developed for fluorescence imaging.[11,12] Additionally, a variety of near-field microscopy techniques have been implemented which benefit from sub-micron localization of the electric field using scanning fiber based or tip-enhanced approaches.[13-22] However, these techniques tend to suffer from signal to noise constraints and as a result offer only a limited improvement over far-field techniques. These technical limitations will likely be overcome with advanced techniques such as the combination of pump-probe microscopy with higher resolution imaging methods such as SEM or AFM. In any case, the ability of pump-probe microscopy to bridge the gap between the nanoscale and the macroscale promises to be a powerful tool for characterizing fundamental optical, electronic, and even mechanical properties in a variety of complex systems. The use of time-resolved microscopies will undoubtedly have a profound impact on the advancement of future nanotechnologies, including nanoscale electronics, photonics, optoelectronics, photovoltaics, and mechanical and chemical sensors.

REFERENCES

1 House, R. L., Kirschbrown, J. R., Mehl, B. P., Gabriel, M. M., Puccio, J. A., Parker, J. K. & Papanikolas, J. M. Characterizing Electron-Hole Plasma Dynamics at Different Points in Individual ZnO Rods. *Journal of Physical Chemistry C* **115**, 21436-21442, (2011).

2 Gabriel, M. M., Kirschbrown, J. R., Christesen, J. D., Pinion, C. W., Zigler, D. F., Grumstrup, E. M., Mehl, B. P., Cating, E. E. M., Cahoon, J. F. & Papanikolas, J. M. Direct Imaging of Free Carrier and Trap Carrier Motion in Silicon Nanowires by Spatially-Separated Femtosecond Pump-Probe Microscopy. *Nano Letters* **13**, 1336-1340, (2013).

3 Mehl, B. P., Kirschbrown, J. R., Gabriel, M. M., House, R. L. & Papanikolas, J. M. Pump–Probe Microscopy: Spatially Resolved Carrier Dynamics in ZnO Rods and the Influence of Optical Cavity Resonator Modes. *The Journal of Physical Chemistry B* **117**, 4390-4398, (2013).

4 Gabriel, M. M., Grumstrup, E. M., Kirschbrown, J. R., Pinion, C. W., Christesen, J. D., Zigler, D. F., Cating, E. E. M., Cahoon, J. F. & Papanikolas, J. M. Imaging Charge Separation and Carrier Recombination in Nanowire p-i-n Junctions Using Ultrafast Microscopy. *Nano Letters* **14**, 3079-3087, (2014).

5 Grumstrup, E. M., Gabriel, M. M., Cating, E. M., Pinion, C. W., Christesen, J. D., Kirschbrown, J. R., Vallorz, E. L., Cahoon, J. F. & Papanikolas, J. M. Ultrafast Carrier Dynamics in Individual Silicon Nanowires: Characterization of Diameter-Dependent Carrier Lifetime and Surface Recombination with Pump–Probe Microscopy. *The Journal of Physical Chemistry C* **118**, 8634-8640, (2014).

6 Grumstrup, E. M., Cating, E. M., Gabriel, M. M., Pinion, C. W., Christesen, J. D., Kirschbrown, J. R., Vallorz, E. L., Cahoon, J. F. & Papanikolas, J. M. Ultrafast Carrier Dynamics of Silicon Nanowire Ensembles: The Impact of Geometrical Heterogeneity on Charge Carrier Lifetime. *The Journal of Physical Chemistry C* **118**, 8626-8633, (2014).

7 Grumstrup, E. M., Gabriel, M. M., Cating, E. E. M., Van Goethem, E. M. & Papanikolas, J. M. Pump–probe microscopy: Visualization and spectroscopy of ultrafast dynamics at the nanoscale. *Chemical Physics* **458**, 30-40, (2015).

8 Mehl, B. P., Kirschbrown, J. R., House, R. L. & Papanikolas, J. M. The End Is Different than The Middle: Spatially Dependent Dynamics in ZnO Rods Observed by Femtosecond Pump-Probe Microscopy. *Journal of Physical Chemistry Letters* **2**, 1777-1781, (2011).

9 Grumstrup, E. M., Gabriel, M. M., Pinion, C. W., Parker, J. K., Cahoon, J. F. & Papanikolas, J. M. Reversible Strain-Induced Electron–Hole Recombination in Silicon Nanowires Observed with Femtosecond Pump–Probe Microscopy. *Nano Letters* **14**, 6287-6292, (2014).

10 Gabriel, M., Grumstrup, E., Kirschbrown, J., Pinion, C., Christesen, J., Zigler, D., Cating, E., Cahoon, J. & Papanikolas, J. in *19th International Conference on Ultrafast Phenomena.* 09.Wed.E.05 (Optical Society of America).

11 Wang, P., Slipchenko, M. N., Mitchell, J., Yang, C., Potma, E. O., Xu, X. & Cheng, J.-X. Far-field imaging of non-fluorescent species with subdiffraction resolution. *Nat Photon* **7**, 449-453, (2013).

12 Gong, L. & Wang, H. Breaking the diffraction limit by saturation in stimulated-Raman-scattering microscopy: A theoretical study. *Physical Review A* **90**, 013818, (2014).

13 Smith, S., Holme, N. C. R., Orr, B., Kopelman, R. & Norris, T. Ultrafast measurement in GaAs thin films using NSOM. *Ultramicroscopy* **71**, 213-223, (1998).

14 Nechay, B. A., Siegner, U., Achermann, M., Bielefeldt, H. & Keller, U. Femtosecond pump-probe near-field optical microscopy. *Review of Scientific Instruments* **70**, 2758-2764, (1999).

15 Nechay, B. A., Siegner, U., Morier-Genoud, F., Schertel, A. & Keller, U. Femtosecond near-field optical spectroscopy of implantation patterned semiconductors. *Applied Physics Letters* **74**, 61-63, (1999).

16 Shen, Y., Lin, T.-C., Dai, J., Markowicz, P. & Prasad, P. N. Near-Field Optical Imaging of Transient Absorption Dynamics in Organic Nanocrystals. *The Journal of Physical Chemistry B* **107**, 13551-13553, (2003).

17 Terada, Y., Yoshida, S., Takeuchi, O. & Shigekawa, H. Real-space imaging of transient carrier dynamics by nanoscale pump–probe microscopy. *Nature Photonics* **4**, 869-874, (2010).

18 Berweger, S., Atkin, J. M., Xu, X. G., Olmon, R. L. & Raschke, M. B. Femtosecond Nanofocusing with Full Optical Waveform Control. *Nano Letters* **11**, 4309-4313, (2011).

19 Berweger, S., Atkin, J. M., Olmon, R. L. & Raschke, M. B. Light on the Tip of a Needle: Plasmonic Nanofocusing for Spectroscopy on the Nanoscale. *The Journal of Physical Chemistry Letters* **3**, 945-952, (2012).

20 Atkin, J. M. & Raschke, M. B. Techniques: Optical spectroscopy goes intramolecular. *Nature* **498**, 44-45, (2013).

21 Karki, K., Namboodiri, M., Zeb Khan, T. & Materny, A. Pump-probe scanning near field optical microscopy: Sub-wavelength resolution chemical imaging and ultrafast local dynamics. *Applied Physics Letters* **100**, 153103, (2012).

22 Atkin, J. M., Berweger, S., Jones, A. C. & Raschke, M. B. Nano-optical imaging and spectroscopy of order, phases, and domains in complex solids. *Advances in Physics* **61**, 745-842, (2012).